Ultrasonic imaging of contact defects under low frequency loading

Marina Terzi

To cite this version:

Marina Terzi. Ultrasonic imaging of contact defects under low frequency loading. Acoustics [physics.class-ph]. Université Polytechnique Hauts-de-France; Institut National des Sciences Appliquées Hauts-de-France, 2022. English. NNT : 2022UPHF0013 . tel-03777450

HAL Id: tel-03777450

https://uphf.hal.science/tel-03777450v1

Submitted on 14 Sep 2022

Thèse de doctorat

Pour obtenir le grade de Docteur de

l'UNIVERSITÉ POLYTECHNIQUE HAUTS-DE-FRANCE

et l'INSA HAUTS-DE-FRANCE

Discipline, spécialité selon la liste des spécialités pour lesquelles l'École Doctorale est accréditée :
Acoustique

Présentée et soutenue par Marina Terzi.

Le 14/03/2022, à Valenciennes

École doctorale :
École Doctorale Polytechnique Hauts-de-France (ED PHF)

Unité de recherche :
Institut d'Electronique de Microélectronique et de Nanotechnologie – Site de Valenciennes (IEMN – UMR CNRS 8520)

Imagerie ultrasonore de défaut de contact sous sollicitations basse fréquence: application pour le contrôle santé de plaques élastiques

JURY

Présidente du jury

- Dragomirescu, Daniela. Professeur. INSA, Toulouse.

Rapporteurs

- Payan, Cédric. Maître de conférences, HDR. LMA, Marseille.
- Meziane, Anissa. Professeur. I2M, Bordeaux.

Examinateurs
- de Rosny, Julien. DR CNRS. Langevin institute, Paris.
- Chapuis, Bastien. Ingénieur de recherche, Docteur. CEA LIST, Saclay.

Directeur de thèse : Moulin, Emmanuel. Professeur. INSA HdF, Valenciennes.

Co-directeur de thèse : Aleshin, Vladislav. CR CNRS. IEMN, Villeneuve d'Ascq.

Co-encadrant : Chehami, Lynda. Maître de conférences. UPHF, Valenciennes.

PhD Thesis

Submitted for the degree of Doctor of Philosophy from

UNIVERSITÉ POLYTECHNIQUE HAUTS-DE-FRANCE

And INSA HAUTS-DE-FRANCE

Subject: **Acoustics**

Presented and defended by Marina TERZI.

On 14/03/2022, Valenciennes

Doctoral school:

Doctoral School Polytechnique Hauts-de-France

Research unit:

Institute of Electronics Microelectronics and Nanotechnology – Site of Valenciennes (IEMN – UMR 8520)

Ultrasonic imaging of contact defects under low frequency loading: application for structural health monitoring of elastic plates

JURY

President of jury

- Dragomirescu, Daniela. Professor. INSA, Toulouse.

Reviewers

- Payan, Cédric. Associate professor, HDR. LMA, Marseille.
- Meziane, Anissa. Professor. I2M, Bordeaux.

Examiners

- de Rosny, Julien. DR CNRS. Langevin institute, Paris.
- Chapuis, Bastien. Research engineer, PhD. CEA LIST, Saclay.

Thesis director : Moulin, Emmanuel. Professor. INSA HdF, Valenciennes.

Thesis co-director : Aleshin, Vladislav. CR CNRS. IEMN, Villeneuve d'Ascq.

Co-supervisor: Chehami, Lynda. Associate professor. UPHF, Valenciennes.

The only difference between screwing around and science is writing it down.

Alex Jason

Acknowledgments

The last three years have shown me both the extreme devastation and the euphoria that research can bring to a scientist. I am grateful to everyone who turned this PhD journey into reality, particularly, to my scientific advisors Prof. Emmanuel Moulin and Dr. Vladislav Aleshin, who admitted me for this position and guided me in the world of research through thick and thin. I have been extremely lucky to have as a supervisor Dr. Lynda Chehami, who has thrown herself into this project with such commitment and set an excellent example of a young woman's hard work and competence in research. I thank these people for their great assistance at every stage of my thesis.

I am extremely grateful to my reviewers Dr. Cedric Payan, Prof. Anissa Meziane for their reports and recommendations, as well as to examiners Prof. Daniela Dragomirescu, Dr. Julien de Rosny, Dr. Bastien Chapuis for accepting my thesis and asking questions that led to a deep and rich discussion.

My honest thanks go as well to the engineer Nikolay Smagin for designing a model contact acoustic nonlinearity and helping with the laser vibrometry experiment.

It was a real privilege to be advised by colleagues from Langevin Institute : Dr. Maxime Farin and Dr. Julien de Rosny, who not only helped to design an experimental setup for simultaneous noise emission and wrote a code to operate it but also provided with a sound card and a computer. Also Maxime taught me different signal processing techniques and for that I am very grateful. I would also like to thank Dr. Claire Prada for the insightful advises on my research.

On the modeling tool for wave propagation in solids with defects, my special thanks to Dr. Kevin Truyaert and Dr. Steven Delrue from KU Leuven University.

I thank my colleagues and peers for always being there for me and creating an amazing atmosphere in the laboratory.

At the end I would like to thank my school physics teacher Sergey Kolpakov and my Master's thesis advisor Prof. Oleg Sapozhnikov for instilling in me an interest in physics. Without them I would not reach this point.

These acknowledgments would be incomplete without thanking my family, friends and my beloved Chakib who was supporting me throughout this time, preventing from giving up, encouraging to continue no matter what.

Above all, thanks to French National Agency (ANR) for financing my thesis as a part of the project « Passive Ambient Noise-based Structural monitoring through exploitation of Contact Acoustic Nonlinearity » (PANSCAN).

Table of contents

Page

List of figures

Page

Introduction

Problem statement

For over seventy years, non-destructive testing (NDT) of materials has been an area of continued growth. Structural health monitoring (SHM) is an important particular case of NDT allowing to permanently inspect a structure in service for flaws. Examples of SHM applications include aircraft structures, bridges, offshore wind energy plants, pipes and rails. Detecting flaws and analyzing their severity in time is critical for transportation safety, safe use of infrastructure and industrial objects.

Ultrasound is relatively inexpensive and harmless technology comparing to other SHM methods. Classical methods of ultrasonic NDT involve actuators and sensors attached to the testing structure. In pitch-catch inspection mode, actuator emits ultrasound so that it it propagates through the structure and is received by the sensor on the other side. The passed signal delay can be used to determine the presence of damage. In pulse-echo inspection mode, the same element plays the role of actuator and sensor. Instead of passed signal here the reflected signal delay reveals damage.

Some limitations are specific to SHM. Indeed, contrary to the conventional NDT, it is not possible to physically move the scanning sensors around the sample, since they are integrated into the structure. It is therefore necessary to use robust signal processing techniques to extract useful information on the defect using a limited number of sensors. It is also important to reduce the power consumption of the ultrasonic sources, to make them lighter, simplify the electronics, and limit the electromagnetic interactions between the cables.

Some NDT techniques require additional measurement on a baseline pristine sample. It should be a copy of the test sample except for damage presence. It is challenging to produce such a sample for some cumbersome or unique structures (e.g. colliders or nuclear reactors). Another issue with baseline is that it stops being valid and has to be replaced whenever environmental or operational conditions change.

To address the two latter issues, in this work we propose to use the ambient noise to scan the inspected sample. Indeed, when the noise is diffuse, i.e. without any privileged location or direction, the cross-correlation of the signals recorded between two points of the environment gives the impulse response (i.e. the Green's function) as if one of the two receivers had been substituted by an actuator. This approach has been used in seismology since 1968, first introduced by Claerbout [1]. Some years later, in the ultrasonic domain, Lobkis and Weaver [2] showed that the latter is also valid in reverberant solids. Since then significant number of research works have been concerned with passive acoustic SHM, i.e. inspection based on the use of ambient noise.

The most interesting findings highlighted in the project ANR PASNI (Passive Acoustic Sensing Network and Imaging), in which my supervisors E. Moulin and L. Chehami were involved, contributed to development of passive ambient noise imaging. L. Chehami et al. developed a reliable passive damage localization algorithm. My PhD thesis is a continuation of her work.

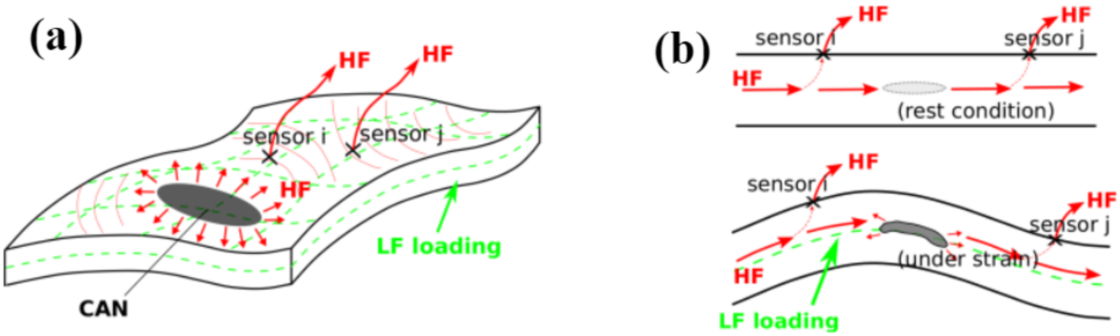

FIGURE 1 – Illustration of CAN behaviour under LF loading : (a) nonlinear HF emission (e.g. harmonics generation) ; (b) local variation of material properties and wave scattering.

For robust damage monitoring, it is important to detect nonlinear defects such as cracks, delaminations, etc. In this thesis, contact acoustic nonlinearity (CAN) plays the role of damage, and we study its interaction with acoustic waves and vibrations.

When the structure to which CAN belongs is excited with high frequency (HF) acoustic waves and low frequency (LF) vibrations, CAN either becomes a secondary wave source (see fig. 1 a) emitting harmonics or modulates local material properties (fig. 1 b) and scatters the wave in various directions. In this work, damage detection means is based on the modulations induced by CAN under variable low frequency loading states. More precisely, the CAN is subjected to low-frequency (pump) vibrations that modifies the local properties of material which in turn alters the high frequency (probe) signal revealing the signature of the CAN.

The thesis work presented in this manuscript finds its originality in the set of studies conducted at the IEMN-DOAE and IEMN-LCI. This thesis is financed by the French National Research Agency (ANR) in the framework of the ANR PANS-CAN (Passive Ambient Noise-based Structural monitoring through the exploitation of Contact Acoustic Nonlinearity) project, carried out by a four UMR CNRS laboratories : IEMN-DOAE (Valenciennes), IEMN-LCI (Villeneuve d'Ascq), Institut Langevin (Paris) and LaMCoS (Lyon).

Research objectives

Summarizing the desired requirements we formulate the following objectives of the present study :

Experimental : develop an acoustical localization technique for SHM that

- is sufficiently sensitive for robust detection of contact nonlinearities
- does not require baseline sample
- is efficient for passive inspection with ambient noise

Theoretical : Create a numerical model or, eventually, numerical tool for modeling wave propagation in a thin plate containing contact acoustic nonlinearity

- taking inner friction into account
- predicting measurable indicator of contact acoustic nonlinearities
- helping to test and optimize the detection algorithm

Practical :

- Contribute to the creation of embedded structural health monitoring system into aircrafts

Thesis outline

This manuscript consists of five chapters. In the first chapter, a review on existing ultrasonic structural health monitoring methods is given with an emphasis on reference-free and passive methods. Lamb waves interaction with defects in an elastic plate is discussed. Scattering characteristics of damage are introduced and the method to measure them is described. Green's function reconstruction from correlation of diffuse waves is discussed.

Chapter 2 describes in detail pump-probe experimental procedures of two kinds : synchronized and non-synchronized emission between low frequency and probe signals. Reference-free repetitive probing damage localization algorithm taking into account the dispersion of A0 Lamb mode is proposed. Results of contact acoustic nonlinearity (CAN) localization on a thin plate are presented with incoherent imaging. To improve localization image contrast, the beamforming algorithm is modified through multiplying by ah-doc coefficients resulting in synchronous detection.

Chapter 3 focuses on relationship between the defect scattering cross-section and localization image contrast. This relationship is derived both theoretically and by measurements. Detection scattering cross-section threshold is estimated. Essential parameters influencing the contrast are found.

Chapter 4 is concerned with preliminary experimental results on the passive localization method. In pump-probe experiments, high frequency white noise plays the role of probe wave. The optimal parameters are established both for diffuse field emission (thus, satisfactory Green's function reconstruction) and for defect scattering cross-section to exceed the detection threshold. Localization results are discussed.

In chapter 5, physical modeling for ultrasonic waves propagation in a thin plate in the presence of localized contact acoustic nonlinearity is performed. The contact is activated by the Lamb wave propagation in a thin plate that generates a specific response in terms of contact loads that, in turn, perturbs the propagation medium and induces secondary waves in there. Two types of CAN are compared with each other : the one that was used in the experiment and more realistic crack-like CAN. Numerical modeling tool that takes into account the above-mentioned phenomena and imitates wave-CAN interactions in simplified 2D plate-like geometry is given.

Chapter 1

General review for SHM techniques and associated signal processing tools

Contents

Introduction

Structural Health Monitoring (SHM) refers to a permanent inspection of a system or a structure in service and includes damage detection, structural integrity assessment, as well as damage evolution prognostics and life-time estimations. Permanent monitoring should be capable of detecting fatigue damage that appears in materials under repetitive loading, and possibly locate it.

Structural Health Monitoring is a part of nondestructive testing (NDT). Examples of widely used methods for not entirely acoustic NDT include : eddy currents in thin plates [3, 4], ionizing radiation tomography [5], thermal wave imaging [6], thermal acoustic imaging and ultrasonic infrared thermography[7, 8]. In industry they often practice magnetic patricle testing and liquid penetrant testing [9, 10]. In this chapter, we will be particularly interested in ultrasonic methods based on guided waves widely used in NDT and SHM.

1.1 Propagation and scattering of Lamb waves in thin elastic plates

Ultrasonic guided waves are a powerful tool in SHM due to their simple implementation, low attenuation, and their ability to provide detailed information about a structure [11].

Lamb waves are guided elastic waves whose particle motion occurs in a thin plate in a plane described by the normal to the surface and the direction of propagation (see fig. 1.1).

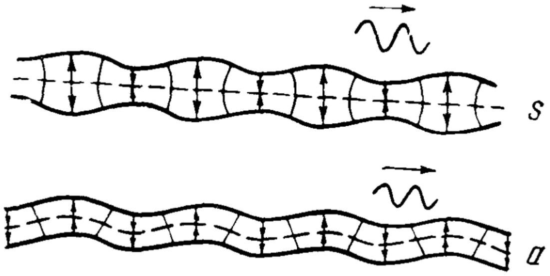

FIGURE 1.1 – Displacement of symmetric (top) and antisymmetric (bottom) Lamb wave modes. The discontinuous line represents the middle of the plate.

They occur in materials with a uniform thickness on the order of a few wavelengths or less. Due to their relatively short wavelengths, they have shown promise in detecting highly localized defects [11].

The issues with Lamb waves based structural health monitoring are in their multimode dispersive nature (see fig. 1.2) and complex wave reflection from structural boundaries. To tackle these issues, usually the inspected plates are chosen relatively large, so it is possible to consider them infinite and the analysis will be based on the first wave arrivals only. Another technique consists of the use of optimal sensors and actuators allocation in correlative sensors array [12]. Damage is located based on analysis of correlations between signals from different sensors.

The effects of dispersion traditionally have been minimized by using narrow bandwidth input signals to concentrate input energy at a point (referred to as the operating point) on the dispersion curves in which the dispersion is low [13]. More recently, digital post-processing techniques have been shown to be effective in compensating for the effect of dispersion, even when the operating point is in a dispersive region [14]. Modal selectivity is generally achieved by using narrow bandwidth input signals in conjunction with transducer design [13].

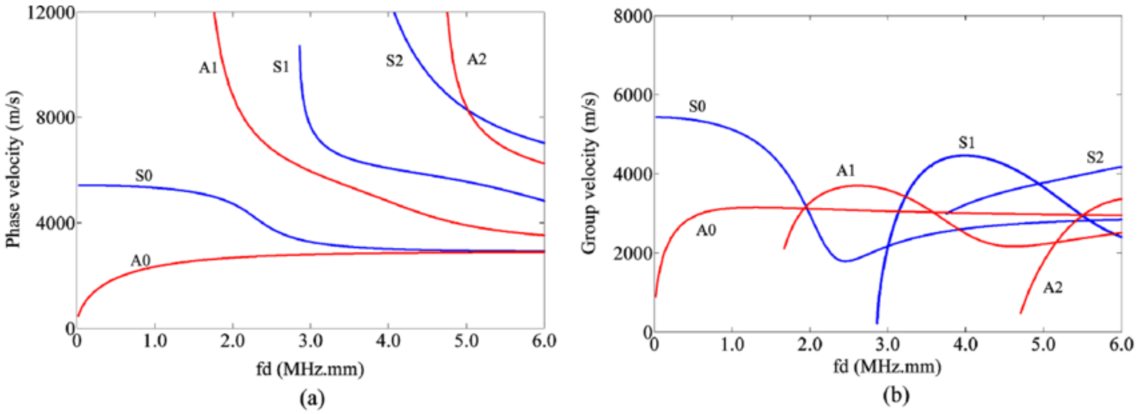

FIGURE 1.2 – (taken from Liu et al. [15]) Dispersion curves of Lamb waves in an aluminum plate : (a) phase velocity and (b) group velocity.

If a plate is sufficiently thin and excitation frequency is sufficiently low, number of Lamb modes in a plate is limited, which prevents modal interaction and simplifies localization process.

In some plates it is possible to excite only one fundamental mode (S0 or A0, see fig. 1.1). Selective generation of Lamb modes is necessary for detecting vertical (S0) and horizontal (A0) damage position [16]. Clezio et al. (2002) [17] used S0 Lamb wave mode by adopting a frequency below the S1 cut-off, to quantify vertical cracks in an aluminum plate. Single A0 mode excitation in a thin plate using Hertzian contact is described in [18] where a transducer generates normal displacement on the surface.

The theoretical number of the antisymmetric Lamb modes that can travel in a plate of a certain thickness is given by Eq. (1.1) [19].

$$N_a = 1 + \left[\frac{2d}{\lambda_l}\right] + \left[\frac{2d}{\lambda_t} + \frac{1}{2}\right], \tag{1.1}$$

where λ_l and λ_t refer to longitudinal and transverse wavelengths, respectively, d is a half-thickness of the plate, « [ ] » denote integer part of a number. Having in mind that $\lambda_t < \lambda_l$ we arrive to the condition : if $[\frac{2d}{\lambda_t}] = 0$, then $N_a = 1$, namely, only A0 mode is present.

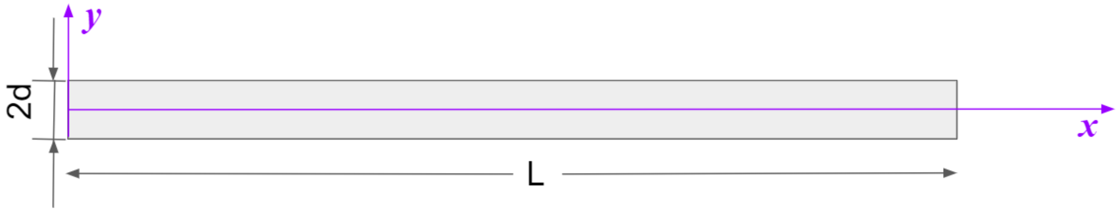

FIGURE 1.3 – Scheme of a thin plate.

The following dispersion relationship in Eq. (1.2) defines wavenumber k for A0 Lamb mode in isotropic plates [19].

$$\begin{aligned}&(2k^2 - k_t^2)^2 \cdot \sinh(\sqrt{k^2 - k_l^2}d) \cdot \cosh\left(\sqrt{k^2 - k_t^2}d\right) = \\ &= 4k^2 \cdot \sqrt{k^2 - k_l^2}\sqrt{k^2 - k_t^2} \cdot \cosh\left(\sqrt{k^2 - k_l^2}d\right) \sinh\left(\sqrt{k^2 - k_t^2}d\right),\end{aligned} \tag{1.2}$$

where $k_l = \frac{\omega}{c_l}$ and $k_t = \frac{\omega}{c_t}$ are wavenumbers for longitudinal and transverse waves with longitudinal $c_l = \sqrt{\frac{E(1-\nu)}{\rho(1+\nu)(1-2\nu)}}$ and transverse $c_t = \sqrt{\frac{E}{2(1+\nu)\rho}}$ phase velocities, d is a half-thickness of the plate, ω stands for angular frequency, E and ν are Young's modulus and Poisson's ratio of plate material, respectively, and ρ is mass density of a plate material. If k_{A0} is a solution to Eq. (1.2), then displacement components for A0 mode can be expressed as :

$$\begin{cases} u_x^{Lamb} = Bk_{A0}(\frac{\sinh qy}{\cosh qd} - \frac{qs}{k_{A0}^2+s^2} \cdot \frac{\sinh sy}{\cosh sd}) \cos(k_{A0}x - \omega t - \pi/2) \\ u_y^{Lamb} = -Bq(\frac{\cosh qy}{\cosh qd} - \frac{2k_{A0}^2}{k_{A0}^2+s^2} \cdot \frac{\cosh sy}{\cosh sd}) \cos(k_{A0}x - \omega t), \end{cases} \tag{1.3}$$

where $q = \sqrt{k_{A0}^2 - k_l^2}$, $s = \sqrt{k_{A0}^2 - k_t^2}$, B is an amplitude-related factor with the dimensionality of the length square. Coordinate system (x,y) is introduced in fig. 1.3.

By taking time derivative of Eq. (1.3), velocity components for A0 mode can be obtained :

$$\begin{cases} v_x^{Lamb} = -\omega B \cdot k \cdot (\frac{\sinh qy}{\cosh qd} - \frac{2 \cdot q \cdot s}{k^2+s^2} \cdot \frac{\sinh sy}{\cosh sd}) \cdot \cos{(kx - \omega t)} \\ v_y^{Lamb} = -\omega B \cdot q(\frac{\cosh qy}{\cosh qd} - \frac{2 \cdot k^2}{k^2+s^2} \cdot \frac{\cosh sy}{\cosh sd}) \cdot \sin{(kx - \omega t)}\,. \end{cases} \tag{1.4}$$

Stress tensor components can be deduced from Eq. (1.3) by using Hook's law $\sigma_{ik} = \lambda \varepsilon_{ll} \delta_{ik} + 2\mu \varepsilon_{ik}$ resulting in :

$$\begin{cases} \sigma_{xx}^{Lamb} = (\lambda + 2\mu) B k^2 (\frac{\sinh qy}{\cosh qd} - \frac{2qs}{k^2+s^2} \frac{\sinh sy}{\cosh sd}) \cos{(kx - \omega t)} \\ -\lambda B q (\frac{q \sinh qy}{\cosh qd} - \frac{2k^2 s}{k^2+s^2} \frac{\sinh sy}{\cosh sd}) \cos{(kx - \omega t)} \\ \sigma_{xy}^{Lamb} = 2\mu B k q (\frac{\cosh qy}{\cosh qd} - \frac{\cosh sy}{\cosh sd}) \cdot \sin(kx - \omega t) \\ \sigma_{yy}^{Lamb} = -Bq(\lambda + 2\mu)(\frac{q \sinh qy}{\cosh qd} - \frac{2k^2 s}{(k^2+s^2)} \cdot \frac{\sinh sy}{\cosh sd}) \cos(kx - \omega t) \\ +\lambda B k^2 (\frac{\sinh qy}{\cosh qd} - \frac{2qs}{(k^2+s^2)} \cdot \frac{\sinh sy}{\cosh sd}) \cos(kx - \omega t)\,, \end{cases} \tag{1.5}$$

where λ and μ are Lamé parameters.

Another way to obtain $k_{A0}(\omega)$ is by using Kirchoff-Love theory [20] based on the following assumptions :

- Plate is isotropic, plane and homogeneous ;
- Transverse displacement of the plate mean plane does not exceed its thickness ;
- The normal to plate surface remains normal to plate mean plane during deformation ;
- Rotational inertia of the plate can be neglected (valid for low frequency-thickness products).

If all these conditions are met, then the following equation for normal displacement u_y holds :

$$D\Delta^2 u_y(\vec{r}, t) + 2\rho d \frac{\partial^2 u_y(\vec{r}, t)}{\partial t^2} = -F(\vec{r_s}, t)\,, \tag{1.6}$$

where $F(\vec{r_s}, t)$ is a transverse component of a force acting on the plate, and D is a bending stiffness coefficient defined as :

$$D = \frac{2Ed^3}{3(1 - \nu^2)}\,. \tag{1.7}$$

Solution of Eq. (1.6) in the form of propagating wave $u_{y_0}\ e^{-i(\vec{k}\vec{r} - \omega t)}$ leads to the following analytical expression of A0 wave number for low frequency-thickness products :

$$k(\omega) = \Big(\frac{2\rho d}{D}\Big)^{1/4} \sqrt{\omega}\,. \tag{1.8}$$

In the next section, interaction of Lamb waves with defects in a thin plate will be discussed.

1.2 Damage detection using guided waves

1.2.1 Active baseline-free methods

Many SHM techniques require additional reference measurements on a baseline intact sample for comparison with the actual monitored structure. However, even a significant difference with the reference in measured properties does not necessarily indicate the presence of damage. Indeed, materials' characteristics can slowly evolve due to aging, environmental effects, change in temperature, loading, boundary conditions, moisture, surface conditions or other external factors, etc. In addition, measurements in the original state of a structure are frequently not available or not possible. That is why development of reference-free damage detection methods has lately become a trend in research works.

Environmental and operational conditions effects on Lamb wave based structural health monitoring systems are reviewed in [21]. Temperature variations affect amplitude and arriving time of Lamb waves. It is experimentally shown that by increasing temperature, the wave group velocity decreases which affects the experimental measurement of time of flight.

Low frequency vibration causes deviation in recorded time domain signals [22] in comparison with static structure, since vibration generates flexural waves in addition to the Lamb waves actuated by the PZT elements. Time of flight changes only within the margin of error, so time of flight based methods are still valid. Strain tensor becomes asymmetric and Lamb waves speeds change because of the acoustoelastic effect [23].

Loads applied to initially isotropic plate make it slightly anisotropic, hence, the magnitude of the time shift due to varying applied loads, depends on the propagation angle [21].

a) Optimal baseline selection and instantaneous baseline

First ancestors of an algorithm with no baseline is an optimal baseline selection [24, 25] and baseline signal stretch or both of them together [26]. These approaches imply multiple baseline samples subjected under different environmental conditions, i.e. temperatures. The baseline that is the most coherent with an experimental signal is selected and adjusted. Then an error parameter between the signal and the adjusted baseline waveform is calculated and compared to a threshold to determine the structural status. However, optimal baseline selection is storage consuming and there is a risk to confuse a flaw with a temperature deviation.

Stubbs and Kim in 1996 [27] elaborated a method of damage localization in a steel beam based on changes in mode shape of the structure after being damaged. A combination of a finite element model together with postdamage modal parameters from an experiment allow one to estimate possible baseline parameters. This method is feasible only for structures with simple geometry.

To get rid of environmental changes dependency, instantaneous baseline could be applied. In this approach [28], Lamb wave propagation along several paths is interrogated in pitch-catch configuration with a distributed transducers array. Common features in the undamaged paths are considered as instantaneous baseline and used for damage prediction. The flaws of instantaneous baseline are the following : precision strongly depends on number of transducers, localization is only possible on the paths' intersection.

b) Neural networks and artificial intelligence

A promising technology for nondestructive testing is based on artificial neural networks due to their excellent pattern recognition capability. First, neural networks were used in damage localization by Wu et al in 1992 [29]. They trained a neural network to recognize the behavior of the undamaged structure as well as the behavior of the structure with various possible damage states. The trained network was able to detect and localize any existing damage based on structural response measurements. Neural networks can be trained to be immune to changes in various environmental and operational conditions, thus, they only indicate damage when changes in the data do not correlate with the learned effects avoiding false positive predictions. For instance, neural networks provide possibility to use only one initial baseline instead of multiple and build others with the help of dictionary learning algorithm [30]. Or at least the errors in the intact baseline can be accounted [31] by estimation of structure modal properties in various perturbation states. Recently, Mariani et al detected damage in plates using CNN for guided waves at temperatures well outside the range in the baseline set of signals [32].

Neural networks help reducing required number of baseline samples, accounting for errors in intact sample and expanding the detection method scope beyond the existing set of baseline samples, however, up to now neural networks are not able to get rid of baseline samples completely. So although this method is not completely baseline-free but it reduces the methodical error related to the baseline and allows to test samples in conditions different to the baseline set, therefore moves towards baseline-free situation.

c) Coda wave interferometry (CWI)

The idea of CWI is to delay each wave packet by an amount of time proportional to the relative velocity change. Maximum of cross-correlations between source signal and the delayed one in short time-windows corresponds linearly to relative velocity change. As diffused waves travel along much longer paths than direct or simply reflected ones, they are much more sensitive to weak perturbation in the medium. This high sensitivity makes CWI stand out compared to time-of-flight techniques [33]. Using CWI allows to eliminate undesired environmental effects by carrying out tests over a time scale shorter than the characteristic temperature (or humidity) change time. Instead of reference it is possible to compare codas before and after perturbation. However, if change in testing structure between the states before and after perturbation exceeds certain limit, then waveforms might be shifted by more than a half of the wavelength between windows which makes classical CWI inapplicable. In this case stepwise CWI must be applied [34]. In addition, stepwise CWI provides estimation of maximum load amplitude to remain nondestructive. Zhang et al. [35] showed that CWI relying on reference sample is ~ 5 times more accurate. They used one part of the concrete sample to test and the other part as a reference which is sort of instantaneous baseline.

Evidences of interaction between independent waves of different frequencies is a classical proof of nonlinearity existence. Pump-probe experiment is one of the ways to arrange frequency mixing. It implies excitation of a structure by signals of two different central frequencies such as $f_{probe} \gg f_{pump}$. For example, pump-probe experiment applied together with Coda Wave Interferometry in [36] results in a coda wave velocity variation due to interaction with low-frequency pump waves. When the probe signal is shorter than the pump counterpart, it is efficient to perform temporal averaging combined with asynchronous excitation of probe and pump signals, because this procedure averages the nonlinear mixing effect of the pump on the probe wave, hence, enhances it.

d) Probability-based diagnostics

A classical probabilistic damage diagnostic algorithm is based on a correlation coefficient between signals recorded in the same structure at different damage states – no damage (baseline), one damage, two damage – and digital damage fingerprints extracted from the signals captured by a set of sensors. The probability of damage presence at a point is estimated as a sum of probabilities for different actuator-sensor paths. It is related to distances from a point to both actuator and sensor, as well as specific amplitude features related to the presence of damage [37].

Probability-based diagnostic imaging is interesting, because it is not relying on a shape of structure, so it is useful in the absence of structure's physical model, applicable for complex structures such as composites. In [38] probability of the damage presence in the monitoring area estimated using correlation coefficients of Lamb wave signals from an active sensor network. Damage index is defined by comparing the real-time data with the baseline data as reference. Recently reference-free probabilistic approaches also appeared. In [39] the damage index is defined based on the mode conversion of multi-mode guided waves with real-time signals without baseline signals. Interrogating different sensing paths sensor-actuator one can obtain probability of damage presence. Localization precision depends on number of sensors and paths (should be long enough to contain both S0 and A0 modes) and is limited by intersection of paths. However, probabilistic approaches are applicable only for damages related to variation in thickness of the plate (cracks, corrosion).

In reconstruction algorithm for probabilistic inspection of defects (RAPID), probability esteem of damage presence at a certain position depends on a correlation between signals recorded on test and reference samples and distance from emitter to receiver via interrogated point averaged over multiple emitter-receiver pairs. Probability mapping provides damage localization image. In 2007 in [40] it was used for detection of corrosion in an airplane wing and recently geometricaly modified version of RAPID was applied for composite plates [41].

Combination of coda wave interferometry and multiply scattered waves spectroscopy [42] allow one to localize perturbation in propagation velocity (source or scatterer) under diffusion approximation by cross-correlating of the unperturbed and perturbed wave fields. Similar to a standard CWI, analysis of later-arriving waveforms is performed. Later this probabilistic approach was developed and called LOCADIFF (Locating a weak change using diffuse waves) [43]. Maximum likelihood approach combined with a diffusive propagation model provide scatterer's location as well as its effective scattering cross-section.

e) Time reversal

Another method capable of detecting small nonlinearities is called Time Reversal (TR) invariance [44]. The idea of TR is to re-emit of a time reversed version of the reflected and transmitted waves and reconstruct the original pulse shape. Due to the spatial reciprocity and time-reversal invariance of linear wave equations reconstructed signal is deviated from the input – time reversibility breaks down – only in case of nonlinearity (or high attenuation) along the wave path. Typical markers of damage are additional frequencies generated during forward propagation such as higher harmonics, sub-harmonics and zero-frequency component.

As for Lamb waves, application of TR for them is complicated because of their dispersive nature. Dispersion causes non-uniform amplitude distribution of different frequency components in the signal passed through the medium, since some of the components arrive to receiver earlier than the others. Therefore, reconstruction of broadband signals, whose components propagate with essentially different velocities, is challenging. In order to enhance TR and tackle dispersion issue allowing to detect damage in a plate without baseline sample, wavelet-based signal processing technique can be applied [45] or probabilistic approaches such as consecutive outlier analysis [46].

Nevertheless, time reversibility of Lamb waves is widely used for baseline free damage detection techniques, in particular, applying time reversal mirror and self-focusing effect [47],[48],[49], [50]. There are possible concerns with an incorrect interpretation of the physics of time reversal and also incorrect approach to assessing time reversibility in several published papers. Hence, it is recommended to refer to reference [51] for a critical discussion of these issues.

It was concluded [52], that TR is relatively immune to environmental and operational variations but, on the other hand, there are significant limitations such as necessity to employ narrowband signals to minimize dispersion and a large number of transducers required for precise localization. In [53] combination of methods is applied : pump-probe experiment is performed, CWI is used to analyze frequency mix interacting with nonlinearity for global inspection of a structure, and TR aids for damage localization by focusing a pump wave.

In [54] the loss of reciprocity is estimated with a reciprocity index, which compares the discrepancy input signal and re-emitted one depending on elastic responses from A to B and from B to A. High values of this index identify damaged paths between transducers. Together with probabilistic imaging algorithm this technique allowed to detect a delamination in a plate.

f) Lamb wave based SHM

Sohn and co-researchers [55, 45, 52, 56] have put forward a time reversed Lamb wave based damage detection technique through theoretical and experimental study.

Mode conversion technique benefits from multimodal dispersive nature of Lamb waves. In [57] collocating PZT transducers are attached to the opposite surfaces of a thin plate, then guided waves are excited across different transducer pairs. Crack formation creates Lamb wave mode conversion due to a sudden change in the thickness of the plate. Knowledge of transducers' polarization characteristics allows to isolate mode conversion and, hence, identify damage.

Qu et al [58] presents a baseline-free imaging technique based on Lamb waves along with using decomposition of time reversal operator. In [59] Lamb wave based refined time reversal method without baseline has been tested. First, probe frequency of best reconstruction is selected and, second, an extended wave packet ranging between two sidebands accompanying the main mode of the reconstructed signal is used for computing a damage index.

The idea of guided wave tomography was initially inspired by the computational tomographic technique used in X-ray imaging. Combining the computational tomographic algorithms with guided wave features, researchers have been able to generate tomograms that reveal structural integrity of the objects under inspection [60]. Signal Different Coefficients are guided wave features that account for mode conversion, changes in signal amplitude and in wave velocity. They are derived from the mean-removed cross-correlation value between guided wave signals from two data sets.

1.2.2 Passive methods

Passive SHM is monitoring based on analysis of ambient noise (diffuse acoustic field). Monitoring of this kind is energy saving, since ultrasound generator is not required.

The possibility of retrieving the impulse response (the Green's function) of a complex medium by correlating records between two passive sensors has been suggested several times in the literature [61]. Weaver and Lobkis [2] have first shown that method from seismology can be applied in ultrasonic inspection of solid reverberating structures. After this work, principle of correlation of acoustic fields became widely used in underwater acoustics, medical imaging, seismology, etc. In structural health monitoring the pioneer work was done by Farrar and James [62] for monitoring of civil engineering structures by estimating resonant frequencies of a bridge using traffic excitation as an ambient vibration source. Later Larose et al. [63] showed application of the correlation-based approach for measurement of dispersion curves. In 2008 Sabra et al. [64] first proved that it is possible to detect a flaw in a plate. In [65] Snieder derived the Green's function from the correlation of coda waves under assumption that scattered waves propagate on average isotropically near the receivers.

The complexity of this application lies on the nondiffusivity of the ambient field, which leads to an imperfect convergence of correlations towards the Green's functions. As a consequence, localizing, detecting, and imaging defect is a real challenge.

One of the well known passive detection method is matching pursuit [66]. In signal processing, a matched filter is obtained by correlating a known delayed signal, or template, with an unknown signal to detect the presence of the template in the unknown signal. This is equivalent to convolving the unknown signal with a conjugated time-reversed version of the template. A matching pursuit isolates the signal structures that are coherent with respect to a given dictionary. Matching pursuit decomposes any signal into a linear expansion of waveforms that are selected from a redundant dictionary of functions [67]. These waveforms are chosen in order to match the signal structures in the best possible way.

Principle of retrieving information from ambient noise

Information about flaws in thin plates perturbated with diffused ambient noise can be retrieved from Green's function. Green's function between two points of a structure can be reconstructed from correlation of noise signals recorded at these two points. Estimated Green's functions can be then used for damage localization via classical techniques from active NDT methods. Similar to [68],[[69]] the passive damage localization algorithm proposed in this thesis is based on Green's function retrieval from noise correlation matrix. However, in this work the method is baseline-free, thus, instead of comparing Green's functions for a plate with its pristine baseline counterpart, Green's functions are compared between different contact states during pump-probe experiment (see chapter 2).

For a good quality of Green's function reconstruction, several conditions must be met : noise sources with fixed locations should be uncorrelated and emit wideband signals in ultrasound range.

According to [2] under the assumption of diffuse noise, cross-correlation between two receivers A and B is proportional to impulse response between them. It is similar to situation when A is an active emitter and B is a receiver : the recorded signal can be reconstructed as a convolution between emitted signal and impulse response (Green's function) depending on the state of the medium and presence of damage. In passive experiment A and B are both physically receivers but to highlight the similarity with the active situation, one of them e.g. receiver A is referred as virtual emitter.

$$C_{AB}(t) = [G_{AB}(t) - G_{AB}(-t)] \otimes f(t) + n(t)\,. \tag{1.9}$$

Here $\otimes$ stands for a convolution, $C_{AB}(t)$ is a cross-correlation between recordings at point A and at point B, $G_{AB}(t)$ and $G_{AB}(-t)$ are causal and anticausal parts of Green's function between A and B respectively, $n(t)$ is called a reconstruction error or spurious term, $f(t)$ is a virtual excitation waveform.

If $h(r_i, r_n, t)$ is an impulse response emitted by the i^{th} noise source and received by the n^{th} receiver, then cross-correlation is defined as follows :

$$C_{mn}(t) = \sum_{i=1}^{N_s} h(r_i, r_m, t) \otimes h(r_i, r_n, -t)\,, \tag{1.10}$$

where N_s is the number of sources.

L. Chehami et al. [68, 70] applied this approach for passive damage detection in thin plates. My thesis is a continuation of these works for reference-free case with nonlinear defects. Green's function retrieval will be used in signal processing of passive experiments in chapter 4.

1.3 Damage localization

1.3.1 Damage localization using ultrasonic arrays

Ultrasonic arrays offer two key advantages over standard monolithic transducers [71]. Firstly, a particular array is able to undertake a range of different inspection angles and focal depths from a single location and so is more flexible than a single element transducer. However, they are most commonly used to produce fields similar to those from traditional single element transducers, i.e. plane, focused and steered beams. Secondly, most types of array (with the exception of annular arrays) can be used to produce images at each test location. This allows rapid visualization of the internal structure of a component. Thirdly, using array of transducers provides more information per time unit, than from single transducer, thus, it is less costly in terms of time.

Apart from the acoustic emission technique, where the damage itself acts as the primary acoustic source, classically considered methods rely on active principles. By implanting small piezoelectric transducers (PZT) into the structures, guided waves can be emitted and received, and it is theoretically possible to monitor a whole given area. Damage localization algorithms using such sparse transducer arrays implanted in structures are widely used.

1.3.2 Beamforming techniques

Classical beamforming

Beamforming is a process of producing a desired wavefront by means of an ultrasonic array. Beamforming can be used to focus ultrasound on a defect in experiment by adjusting excitation time on different array elements or to visualize a defect in post-processing.

The simplest and most widely used technique for beamforming is the delay-and-sum beamformer. By applying delays on the received data from each receiver element prior to summation, the output from the beamformer can be steered in a certain direction. Signals coming from the steered direction will add up constructively, while interfering signals from other directions will generally be reduced.

Total focusing method is a delay and sum beamforming algorithm, in which the array is synthetically focused on each image point in the imaging region. For this reason, it can result in the highest possible imaging resolution of any linear algorithm and has been termed the gold standard in array imaging [72],[73].

Classical delay-and-sum algorithms are very computer-efficient but, since they neglect wave dispersion, they lack accuracy and are not suitable for Lamb waves based SHM.

Speaking of beamforming techniques for phased arrays accounting for Lamb waves dispersion, the earliest work was reported by Deutsch et al. in 1997 [74]. They proposed a method based on time reversal mirror to focus an ultrasonic linear array on a defect. They applied an iterative re-transmission of reversed signal from receivers to emitters with time excitation adjustments based on time-of-flight estimation from cross-correlation of signals recorded on adjacent elements. Focusing occurs when time-of-flight for each element is the same.

Wilcox et al. in 2000 [75] proposed an array-based beam steering technique operating with Lamb modes in the post-processing stage. They showed that circular arrays of round ceramic disks can be applied for omni-directional inspection of plate structures, therefore, this technique contributes to rapid data acquisition from large areas.

Dispersion compensation is challenging, however, some approaches, conversely, take advantage of dispersive structures for the beamforming purposes. For instance, ultra-wideband beamforming [76] with enhanced resolution can be achieved without phase shifters, delay lines, or moving parts by connecting linear antenna array to a passive device made of highly dispersive material, where multipath propagation implies channels with a very low level of correlation. Signals are received by antenna array, then pass through the passive device, after that they are summed up and at the end they are being decoded using time reversal in frequency domain including both magnitude and phase compensation. This technique allows one to obtain a radiation pattern enhancement with simple increase of the antenna array's inter-element spacing.

Compared to the array approaches reviewed above, acoustic tomography uses distributed sensors that surround the inspected area. This technique requires multiple projections to create an image of a region. To obtain these projections, in classical tomography, emitter and receiver are mechanically moved in parallel, which requires a setup capable of accurate positioning of the transmitter and receiver in parallel and complicates field inspections. McKeon et al. [77] evaluated the crosshole technique. Transmitted signal from each position is received at all receiver positions. This leads to a more efficient use of the setup, and is not restricted to a certain geometry which allows to obtain images with fixed array setups.

Michaels et al. [78] proposed the use of the minimum variance distortionless response reference-free algorithm on data from a tomographic setup. A multistatic dataset was acquired by sequentially exiting a number of transducers. A circular ring of transducers surrounded a single defect, which was probed from different angles. This causes the backscattered signals from different excitations to vary substantially. To improve the results a scattering model of the defect was used to compensate for these variations.

Back-propagation algorithm

In [79] Wilcox added dispersion compensation to time reversal mirror for omnidirectional guided wave arrays. Converting raw signals into wavenumber k domain enables recompression of dispersed signals and subsequent phase shifting by $e^{ik(\omega)r}$ to precisely follow the dispersion relationship for the guided wave mode of interest. Angular deconvolution of signals is performed dividing by reference simulated array response. Gaussian filter is applied to reduce side-lobes. This method is limited by geometry of US array : transmitter and receiver element density both must be uniform in the angular domain.

Two types of noise may exist in guided wave tests. Noise that is independent of the desired guided wave signals is considered as incoherent noise. Other noise belongs to the class of coherent noise. Coherent noise includes unwanted guided wave modes, higher order harmonic signals caused by non-linearity, guided wave mode conversions, etc.

Fei et al. in 2010 [80] showed that by applying time delays to the phased array elements guided wave beams can be formed. In the receiving end of the phased array back-propagation technique is used to synthesize the received signals. The combination of real time beam forming and back-propagation provides higher signal-to-noise ratio and longer inspection distance. Back-propagation also allows to suppress the side-lobe effects as well as the influence of guided wave dispersion and coherent noise.

The coherent noise introduced by unwanted guided wave modes can be significantly reduced by selecting guided wave sensors that produce single mode excitation and detection. Another major source of coherent noise for phased array applications is the reflections from objects close to the phased array. This is caused by the wave divergence. The use of real-time phased array has a great advantage to lower the influence of the coherent noise from close reflectors. The physically formed wave beams have strong directivity, which is helpful in reducing the reflections from close reflectors that are away from beam steering direction. The well-formed wave beam also greatly improves the signal-to-noise ratio of the possible reflection signals from defects in the beam steering direction.

Back-propagation algorithm described by Chehami et al. in [68] is a beamforming method applied during post-processing to steer beam formed by ultrasonic phase array omnidirectionally. Multiplication of signals in frequency domain by phase factor taking dispersion into account allows to identify damage location. For low wavenumber-thickness products kd, a single Lamb mode in thin plates can be dominant. In this work, modified version of this algorithm will be applied (see chapter 2 for details).

1.4 Defect scattering characteristics

Every damage can be considered as a scatterer, i.e. some type of obstacle that causes scattering of incident waves.

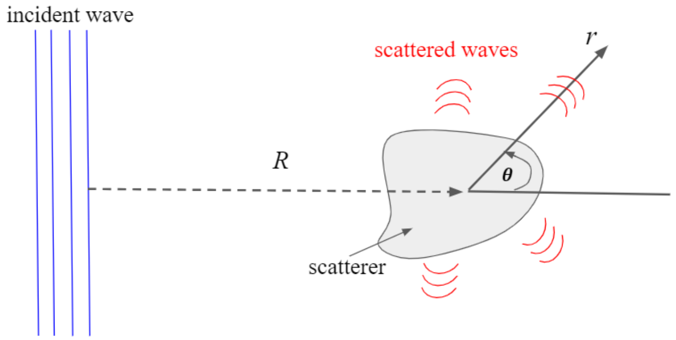

FIGURE 1.4 – Wave scattering by a rigid heterogeneity.

To evaluate scatterer's ability to be detected, the following quantitative characteristics are introduced.

Let us denote θ a scattered angle (between incident and scattered waves), ω is angular frequency, $f(\theta, \omega)$ is a scattered far-field amplitude, and $\sigma(\omega)$ is a scattering cross-section. $f(\theta, \omega)$ is defined in the form of the following 2D scattered field asymptotic behavior [81] :

$$u_{sc}(r,\theta) = \frac{e^{ikr}}{\sqrt{r}}(f(\theta,\omega) + \mathcal{O}(1/r)),\ r \to \infty\,.$$

Then a scattering cross-section, defined as a ratio of the scattered flux to the incident flux, at a frequency ω can be expressed as (see e.g. [82]) :

$$\sigma(\omega) = \int_0^{2\pi} |f(\theta,\omega)|^2 \mathrm{d}\theta\,. \tag{1.11}$$

Scattered amplitude and scattering cross-section are also related by an optical theorem [83] :

$$\sigma(\omega) = -2\sqrt{\frac{\pi}{k}}\,\mathrm{Re}\, f(0,\omega)\,.$$

The optical theorem expresses energy conservation in classical acoustics and electromagnetism [84, 85]. It was first used in the context of flexural wave scattering by Vemula and Norris [86]. The far-field flexural waves are governed by Helmholtz equations makes the form of the optical theorem identical to that of two-dimensional acoustics for both Kirchoff and Mindlin plate theories.

Scattering cross-section is a quantity proportional to the rate at which a particular radiation-target interaction occurs. As applied to our experiment, scattering cross-section represents the rate of interaction between sound wave and a scatterer (defect). If a value of scattering cross-section is sufficiently high, the defect is detectable.

It is possible to relate the scattering properties of a local heterogeneity (or defect) to average features of reverberated signals in a finite plate. To do so and measure defect's scattering cross-section, experimental approach based on statistical properties of scattered flexural wave envelope is applied [87]. A brief summary of this procedure is described below.

First, active static measurements are conducted with defect s^{w} and without defect $s^{w/o}$: a series of sine bursts is excited. Then these signals are filtered in a narrow band. Narrow band filtering allows to consider that scattering cross-section is a constant in this frequency range. After that envelope of an averaged signal is extracted $env(s^{w/o})$. It decays exponentially as $Ae^{-2t/\tau}$ where A is related to the energy emitted into the medium (for more details see [88]).

Estimation of parameters A (amplitude) and τ (reverberation time) is done by fitting of squared signal envelope averaged over receivers with an exponential function using nonlinear least squares fit :

$$\frac{1}{N_r}\sum_{n=1}^{N_r} env^2(s_n^{w/o}) = Ae^{-2t/\tau}\,, \tag{1.12}$$

where subscript n stands for the n^{th} receiver, N_r is the number of receivers. An example of this fitting is shown in fig. 1.5.

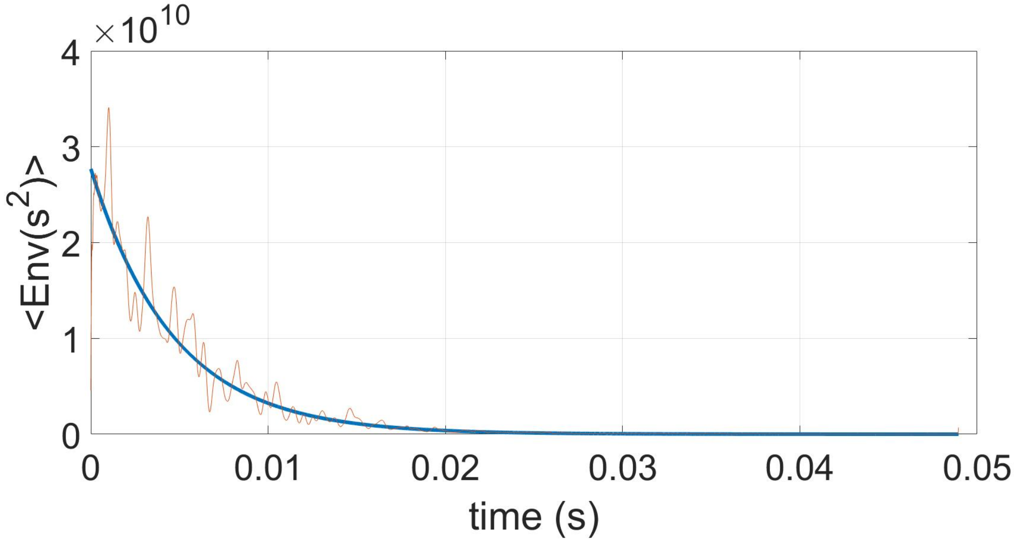

FIGURE 1.5 – Estimation of amplitude A and a plate reverberation time τ by using nonlinear least squares fitting for squared signal envelope averaged over receivers.

A similar procedure is repeated for a differential signal $\Delta s = s^w - s^{w/o}$. Averaged square of differential signal envelopes over number of receivers is fitted with a product of a decaying exponent and linear time function using nonlinear least squares fit to estimate a parameter K :

$$\frac{1}{N_r}\sum_{n=1}^{N_r} env^2(\Delta s_n) = K(v_g t - r_a)e^{-2t/\tau}\,. \tag{1.13}$$

Here v_g is the group velocity for A0 mode, r_a is two times the average distance between defect and any point on the plate : $r_a = \frac{2}{S}\int\int_S \sqrt{(x-x_d)^2 + (y-y_d)^2)}$. S stands for the plate's area, x_d and y_d are defect's coordinates on the plate. Example of this fitting is illustrated in fig. 1.6.

Finally, scattering cross-section can be found as :

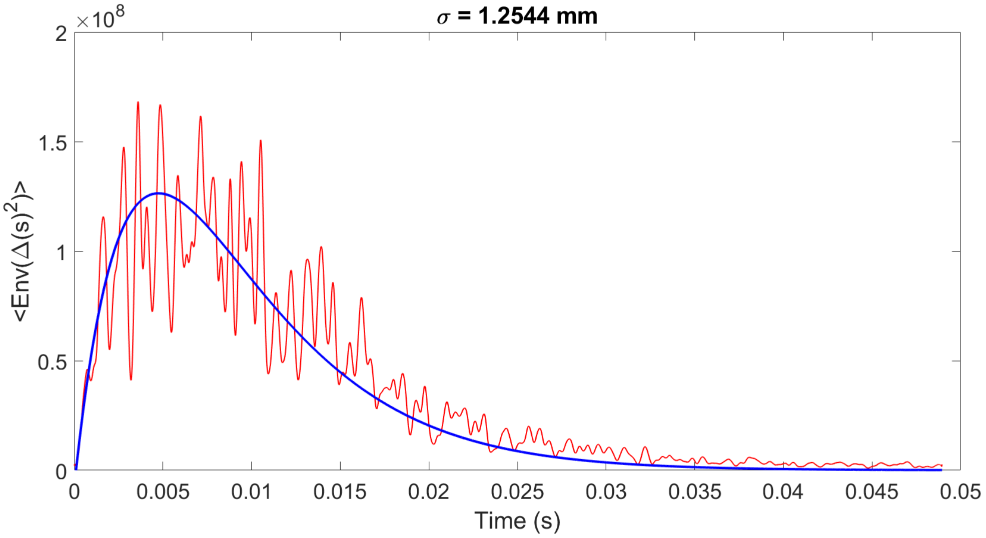

FIGURE 1.6 – Estimation of a parameter K by using nonlinear least squares fitting for squared differential signal envelope averaged over receivers.

$$\sigma = \frac{KS}{A} \tag{1.14}$$

Figs. 1.5,1.6 illustrate an agreement between experimentally obtained square of envelope of a signal and differential signal and the theoretical expression from a statistical model.

In the chapter 3 the described measurements are applied experimentally and it is shown that localization image quality, in particular its contrast, is influenced by the defect scattering cross-section.

Conclusions

We have seen in this chapter some reminders on the propagation of guided waves in thin plates. Dispersive nature and multi-modality of Lamb waves challenges in the context of SHM are discussed. We have shown the advantages of back-propagation algorithm comparing to other beamforming technique, since it takes dispersion into account and uses single mode. The state-of-the-art methods of damage detection are briefly reviewed with an accent on benefits from baseline-free approaches. Multiple reflections from plate boundaries can generate diffuse field. It is shown that correlation of diffuse field is a good candidate for the estimation of the Green's functions of the medium allowing to identify damage.

We propose in the rest of this thesis to adapt back-propagation beamforming for the baseline-free localization and imaging of a contact defect subjected to low frequency vibration in reverberating plates. We will first apply it in active mode in chapter 2. Then we will measure scattering characteristics of damage from flexural waves envelope (as was discussed in section 1.4 of this chapter) to quantify the range of defects that are possible to detect with the proposed method in chapter 3. After that we will adapt damage detection and localization for passive experiments by retrieving Green's function from noise correlations in chapter 4.

Chapter 2

Active baseline-free experiments for CAN localization

Contents

Introduction

This chapter describes a baseline-free imaging method capable of localizing contact acoustic nonlinearity (CAN) in thin plates. This method is based on a pump-probed interaction, in which information of damage is provided by differences in high frequency (HF) probe signals measured under varying contact conditions induced by low frequency (LF) pumping. The contact defect is localized by using a back-propagation technique presented in [68, 70, 89], where baseline-subtraction allowed to strongly enhance the scattering signature of the defect.

In the reported experiments, a steel sphere pressed against an aluminum plate is used to mimic a CAN. Similarly to a crack or delamination, the sphere excited by the LF pumping slightly modifies the propagation conditions for the HF probe. These weak changes are considerably enhanced by cumulating effects over multiple different contact states. Mechanical characteristics of the contact such as its deflection and strain caused by pump and probe waves separately are estimated.

2.1 Experimental setup and pump-probe principle

2.1.1 Pump-probe experiment

In this experiment, the setup consists of a thin aluminum rectangular plate (1 m × 0.5 m × 3 mm) horizontally suspended with elastic strings on a metallic supporting structure, and instrumented with piezoelectric transducers (model « KEPO FT-20T-4.0A1-465 ») glued on its surface. Instead of real defect we use a 1 cm diameter steel sphere pressed against the top plate surface (see fig. 2.1).

Two types of vibrations are generated in the plate (fig. 2.2) : a high-frequency (HF) probe wave corresponding to a one-period sine toneburst at f_{probe}=10 kHz, sequentially emitted at regular time-intervals ΔT ; and a low-frequency (LF) harmonic pump vibration $s_{pump}(t)$ with a frequency f_{pump} in the range of a few Hz ($f_{pump} \ll f_{probe}$). The choice of the probe frequency in the range of dozens of kHz is justified by two reasons. Firstly, signal processing developed in this thesis requires one and the only propagating flexural mode in the plate. Secondly, few tens of kHz is the frequency range of noise emitted by sponge rubbing in the previous works in our research team L. Chehami et al. [70] the ancestor of a passive adaptation for a defect detection method presented in chapter 4. As for the pump wave, the choice of a few Hz is related to the reverberation characteristics of the plate.

The probe signal is emitted using one of the piezoelectric patch transducers glued to the plate surface. Pump vibration is excited using an electromechanical shaker (TIRAvib 50018, fed through its power amplifier TIRA BAA60) connected to the

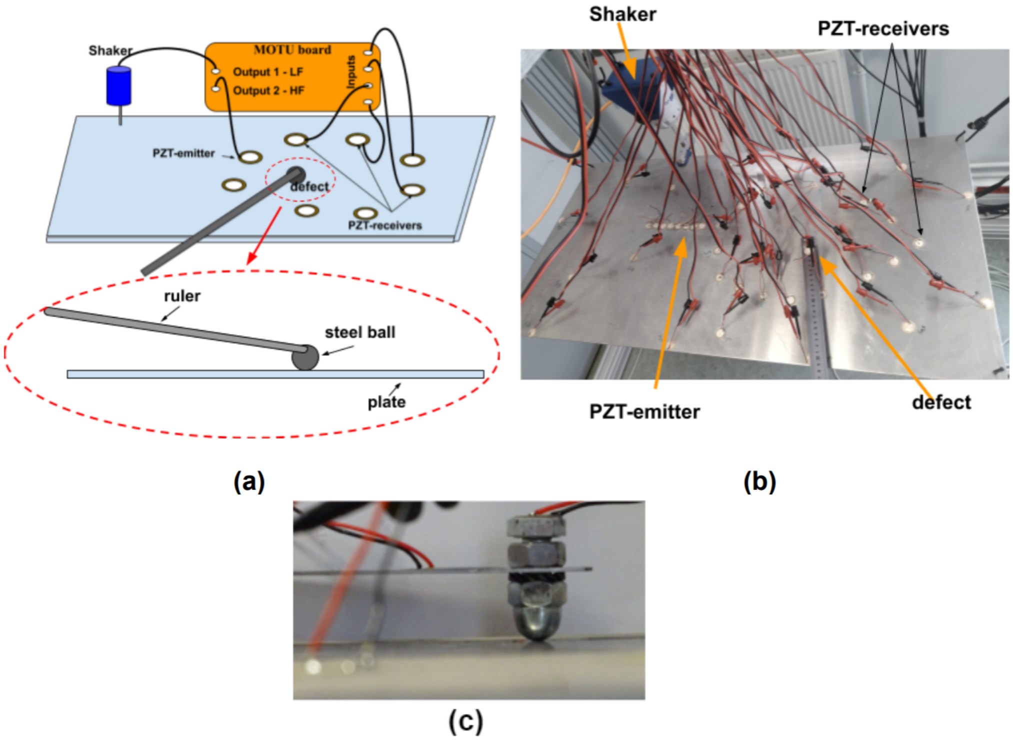

FIGURE 2.1 – Pump-probe experimental setup. (a) - Scheme, (b) - photo, (c) - zoom on the defect.

plate with a steel rod equipped at its extremity with a polystyrene foam-coated clamp gripped to the plate edge. In that way, the shaker forces alternative normal motion at the clamp point of the plate.

In addition to the emitting piezoelectric transducer, $N_r = 14$ receiving transducers of the same kind (model « KEPO FT-20T-4.0A1-465 ») are fixed at known positions. Signals from these transducers are recorded by means of a multichannel digital sampling board (24 I/O MOTU, 96 kS/s, 24 bits digitizer) for 40 s. Low-pass and high-pass filtering then easily allow to retrieve respectively the LF pump vibration and the HF probe signals from these recorded signals. Individual HF signals are then obtained by cutting high-pass filtered signals from each sensor into slices of duration ΔT. We thus denote $s_{m,n}(t)$ the HF signal in the m^{th} slice from the n^{th} receiver R_n.

The idea behind this experimental setup is that LF vibrations will slightly mo-

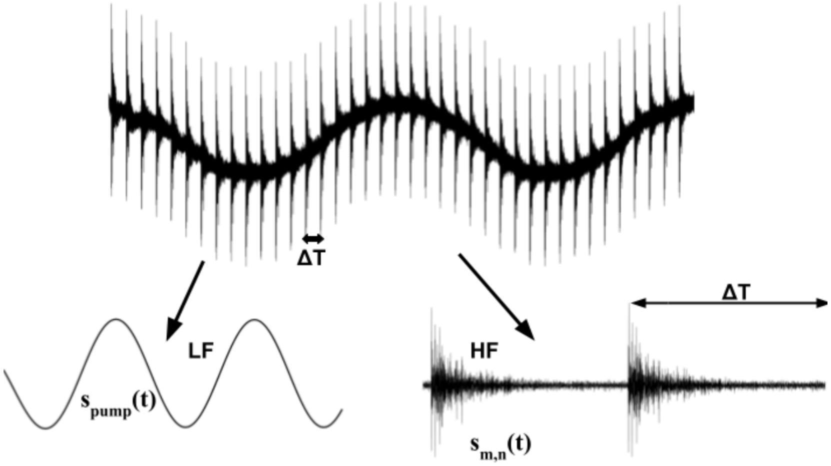

FIGURE 2.2 – Recorded signals as a mix of the LF pump and HF probe waves.

dulate the contact condition (contact load, relative positions) between the plate and the sphere. Each recorded HF signal, containing components with wave paths having crossed the contact area, will then carry information on the contact state at the instant of measurement. Indeed, since ΔT is much smaller than the LF period, as pointed out above, the contact state can be assumed stationary during one HF signal slice. The other restriction is that the duration of one HF slice ΔT should be greater that the plate reverberation time τ to avoid overlapping the adjacent slices. To meet all these requirements the pump frequency must be in the range of few Hz.

Since the effect of contact modulation in the HF signals is expected to be slight, we seek to cumulate information acquired at different contact states (i.e. different HF signal slices).

2.1.2 Synchronized and non-synchronized experiments

There have been done two sorts of experiments depending on the way a pump LF signal was emitted : synchronized and non-synchronized. In synchronized experiments, pump and probe waves are emitted both by a sound board simultaneously. In non-synchronized experiments pump and probe waves are emitted independently from different devices. The pump and probe emission start times are independent of each other.

Both sorts of experiments prove to show satisfactory results for defect localization. Further both of them will be described in more detail.

a) Synchronized experiments

In synchronized experiments (see fig. 2.1 a), a pump and a probe are excited simultaneously with the use of a MOTU sound board (96 kS/s, 24 I/O) being managed from a computer. This setup allows experimenter to have control over LF waveform and a moment LF emission starts. Synchronization provides LF phase information at every given time instant, which makes synchronous detection possible to apply (see section 2.3.1 for details). It is important to note that maximum voltage available from the sound board is around 1.7 V. Later we will see that this fact imposes a strong limitation for damage detection in synchronized experiments.

b) Non-synchronized experiments

In non-synchronized experiments, a pump is excited separately from a probe by an independent electrical generator connected to the shaker through a power amplifier. In this case, pump is excited continuously and then probing is started at random moment. Thus, a sine phase of pump at that moment is unknown, i.e. pump and probe are not synchronized with each other. On the one hand, it implies no control over a moment when LF emission starts, thus, synchronous detection is not an option. On the other hand, it is easy to control LF amplitude and it can be made relatively high to magnify fine modulation effect we are trying to observe here.

We used here the same experimental testbench as described before in section 2.1.1. Here individual HF signals are obtained using National Instruments acquisition board (500 kS/s, 8 channels). They pass through high-pass filter and are amplified at reception. $f_{probe} = 20$ kHz and number of PZT patches receiving signals is $N_r = 7$. 40 consecutive acquisitions of HF signals were performed.

2.2 Estimation of displacement and strain induced by pump and probe waves excitation

Before presenting the obtained imaging results (in section 2.3), it is interesting to estimate the orders of magnitude of mechanical parameters involved in our experimental setup. In particular, comparison of displacements and strains induced respectively by the pump vibrations and the HF probe wave is essential to get more quantitative insight on the pump-probe processes. Besides, detection threshold estimation in terms of pump excitation will also help us quantify capabilities of the developed technique. This is what is proposed in this section.

2.2.1 Measurements of displacement and strain induced by pump excitation using image correlation

Before presenting the obtained imaging results (in section 2.3), it is interesting to estimate the orders of magnitude of mechanical parameters involved in our experimental setup. In particular, comparison of displacements and strains induced respectively by the pump vibrations and the HF probe wave is essential to get more quantitative insight on the pump-probe processes. Besides, detection threshold estimation in terms of pump excitation will also help us quantify capabilities of the developed technique. This is the subject of the current section.

a) Evaluation of displacement caused by pump : image correlation

Displacement induced by the pump wave is estimated using image correlation technique. First, ten-second videos of the pump-probe experiment are recorded with « zoom » on the defect at different pump amplitudes (in the range of 0.5-6 V). In these experiments, pump is a continuous sine wave at 1 Hz. Second, each video is converted into frames. After that, frames are converted into gray scale images. In the image a small fragment with high contrast – preferably, with the Dirac δ distributed intensity – in y-direction, but homogeneous in x-direction was selected, since we are looking for vertical displacement. A fragment of the photo with the washer connecting the two nuts (see fig. 2.3 b) meets these requirements. The defect is considered a rigid body, so the vertical displacements of the washer and the sphere are equal. Then gray scale intensity of the selected image fragment is averaged in x-direction. Finally, this averaged gray scale intensity is cross-correlated with its counterparts in different frames of the selected image fragment corresponding to various time instants. Maximum of correlation corresponds to a coordinate of the moving object (defect). Thus, shift in distance of the correlation peak position plotted against time can reveal an amplitude of the defect displacement (see fig. 2.4).

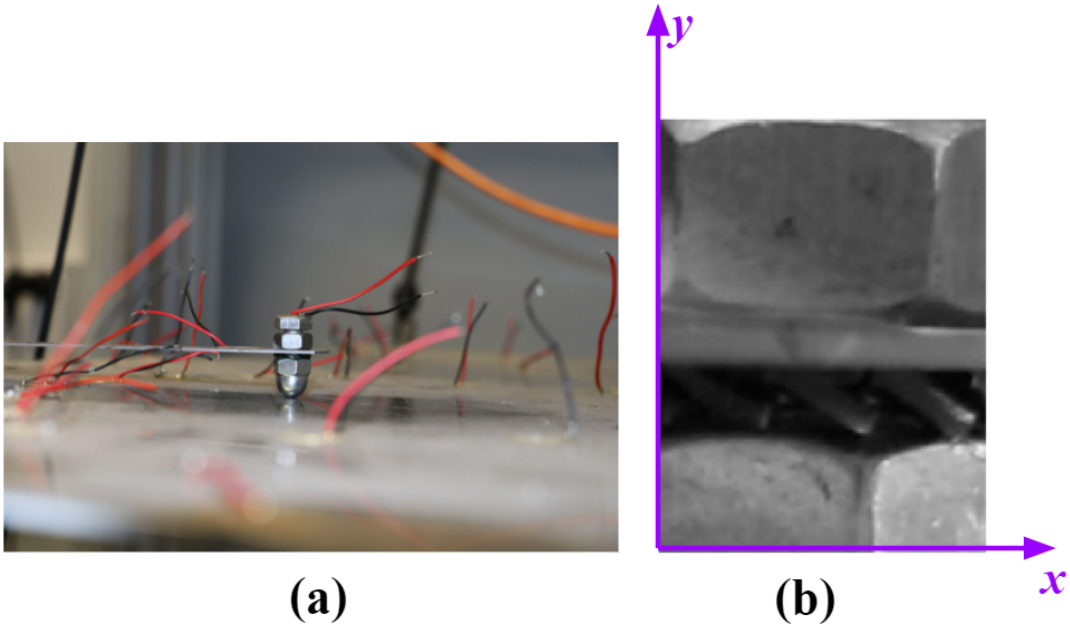

FIGURE 2.3 – (a) - Frame of a video of the pump-probe experiment : zoom on the defect, (b) - gray scale fragment of this frame selected for image correlation procedure to estimate the sphere's y-displacement induced by pump excitation.

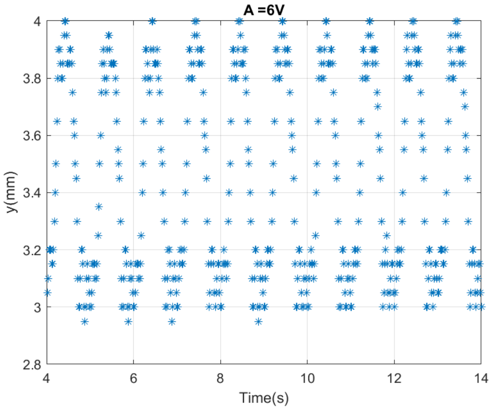

FIGURE 2.4 – Shift in coordinate corresponding to maximum correlation vs time at pump amplitude 6 V.

After averaging over ten pump periods, amplitude of y-displacement $\Delta\delta$ is calculated and plotted against pump amplitude in fig. 2.5. The dependency is linear.

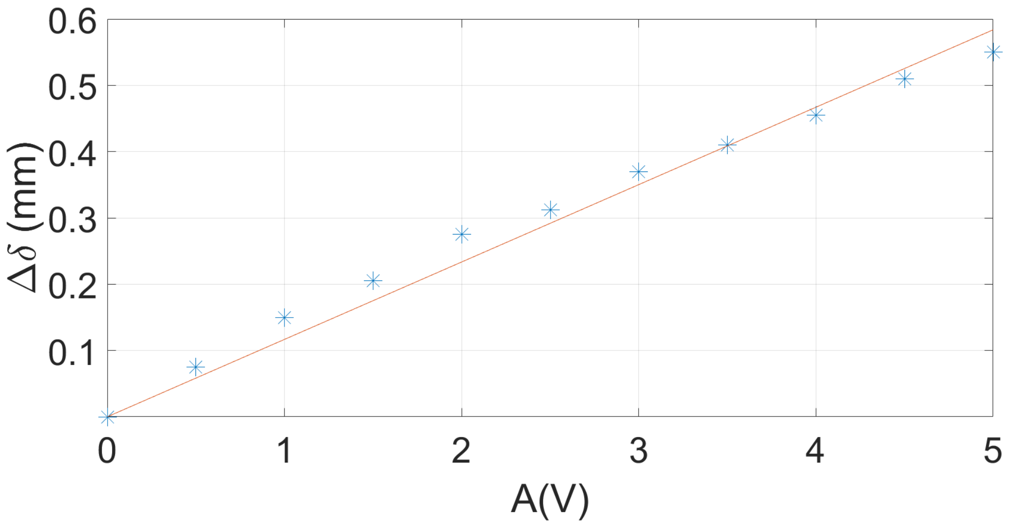

FIGURE 2.5 – Defect's y-displacement due to pump excitation vs pump amplitude.

b) Estimation of strain caused by pump wave at the defect-plate contact area

After the estimation of the pump wave displacement (resulting in ruler's deflection), it is possible to estimate the corresponding contact force and strain. It is generally known [90] that for a flexed rod, which our ruler can be roughly approximated by, relationship between its deflection δ and exerted force is the following :

$$\delta = \frac{Nl^3}{3IE_1}, \tag{2.1}$$

where N is the normal force, l is the ruler's length, E_1 is Young's modulus of steel, I is its inertia moment, which is for rectangular section equal to :

$$I = \frac{bh^3}{12}, \tag{2.2}$$

where b and h stand for the ruler's width and thickness, respectively. Substituting this expression into Eq. (2.1) yields :

$$N = \frac{E_1 b h^3}{4 l^3} \delta \,. \tag{2.3}$$

Let us denote N_0 and δ_0 the force and deflection for the system at rest (when there is no plate, ruler is bending free), whereas ΔN and $\Delta\delta$ stand for force and deflection caused by pump oscillations and interaction with a plate. Thus, at every moment the following statements will hold :

$$\begin{cases} N = N_0 + \Delta N \\ \delta = \delta_0 + \Delta\delta \,. \end{cases}$$

The edge of the ruler is connected to the sphere, so N is also a force applied at the Hertz contact [91] given by :

$$N = \frac{4}{3} E^* \sqrt{R} a^{3/2} \tag{2.4}$$

where R is the sphere's radius, a is an interpenetration distance between the sphere and the plate, E^* is effective Young's modulus defined as

$$\frac{1}{E*} = \frac{1-\nu_1^2}{E_1} + \frac{1-\nu_2^2}{E_2} \tag{2.5}$$

with ν_1 and ν_2, Poisson's ratios of the ruler material (steel) and plate material (aluminum) respectively, E_2, Young's modulus of aluminum.

For more details about force-displacement relationship for a sphere pressed against a plate see chapter 5.

Then pressure radial distribution in the circle of contact area is [92] :

$$p(r) = p_0 \sqrt{1 - \frac{r^2}{c^2}} \,, \tag{2.6}$$

where c is a radius of the Hertz contact area expressed as

$$c = \sqrt{Ra} \,, \tag{2.7}$$

p_0 is maximum contact pressure given by :

$$p_0 = \frac{3N}{2\pi c^2} = \frac{1}{\pi} \left(\frac{6 N E_2^{*2}}{R^2}\right)^{1/3} . \tag{2.8}$$

According to Hooke's law stress tensor is proportional to strain tensor :

$$\sigma_{zz} \approx E_2 \varepsilon_{zz} \,,$$

where z is a vertical axis.

Considering that at the contact area $\sigma_{zz} = p(r)$, maximum strain obtained at the center of the contact is :

$$\varepsilon = \frac{p_0}{E_2} \,.$$

Assuming that $E_1 \gg E_2$, $\nu_2^2 \ll 1$, $E^* \approx E_2$ and substituting p_0 from Eq. (2.8) results in :

$$\varepsilon \approx \frac{1}{\pi} (\frac{6N}{R^2 E_2})^{1/3} \,.$$

By replacing N with an expression from Eq. (2.3), we get :

$$\varepsilon \approx K d^{1/3}$$

with

$$K = \frac{h}{\pi l} \Big(\frac{3bE_1}{2R^2 E_2} \Big)^{1/3} \,. \tag{2.9}$$

Dividing deformation into strain at rest ε_0 and strain caused by pump-plate interaction $\Delta\varepsilon$ similarly as we did for force and deflection before, one can introduce :

$$\varepsilon = \varepsilon_0 + \Delta\varepsilon$$

with

$$\varepsilon_0 \approx K d_0^{1/3} \,.$$

And assuming $\Delta\delta \ll \delta_0$ leads to :

$$\Delta\varepsilon \approx \frac{K \delta_0^{-2/3}}{3} \Delta\delta$$

Substituting Eq. (2.9) into the last equation finally yields :

$$\Delta\varepsilon \approx \frac{h}{\pi l} \Big(\frac{3bE_1}{2R^2 E_2} \Big)^{1/3} \frac{\delta_0^{-2/3}}{3} \Delta\delta \tag{2.10}$$

Considering h=1 mm, l = 0.5 m, b = 2.7 cm, $E_1 = 2 \cdot 10^{11}$ Pa, R = 0.5 cm, $E_2 = 6.9 \cdot 10^{10}$ Pa, δ_0 = 43 mm, we get approximate values for acoustical strain at different pump amplitudes (see fig. 2.6). In this series of experiments, the defect detection was successful for pump amplitudes higher than A_{th}^{pump} that was between 1 and 1.5 V. In fig. 2.6 acoustical strain corresponding to this detection threshold $\Delta\varepsilon_{th}$ is observed to be around 10^{-5}. This is a limitation of our detection method sensitivity : we can detect damage only if it produces strain $\Delta\varepsilon \geq \Delta\varepsilon_{th} = 10^{-5}$.

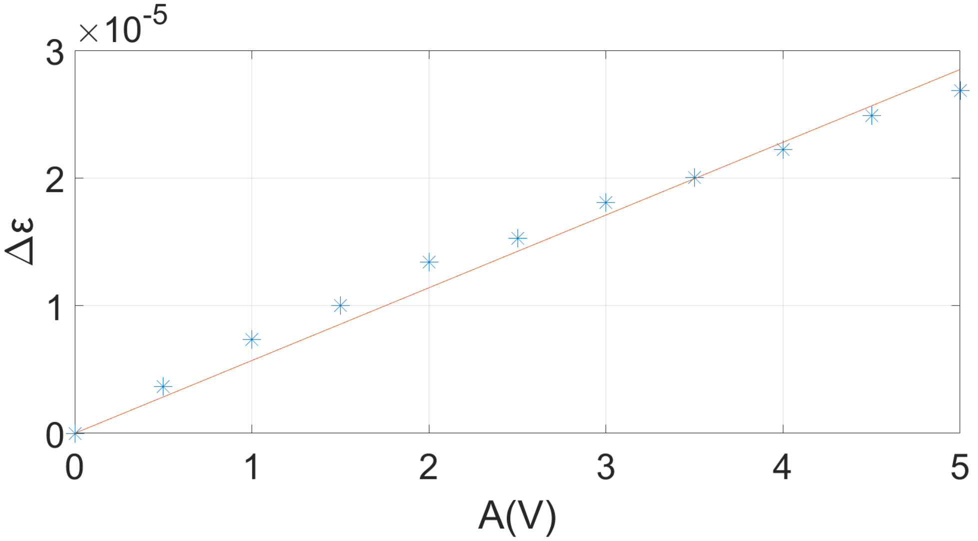

FIGURE 2.6 – Acoustical strain in the center of sphere-plate contact as a function of pump amplitude.

Linear behavior of displacement (fig. 2.5) and strain (fig. 2.6) as functions of pump amplitude means that the materials in contact (steel and aluminum) stay in linear elastic region of the stress-strain curve during the entire experiment. The nonlinear character of the experiment is associated with the interaction of the pump vibrations with the solid contacts in the defect. Indeed, the modulation of the defect properties induced by the pump vibration is nonlinear (since Hertzian contact and friction imply nonlinear force-displacement relationship) and amplitude-dependent, and can be seen as a local manifestation of acousto-elastic or nonlinear elasticity effects (see for instance [93], [94], [95]). Therefore, the HF probe signals will hold some signatures of these local vibration-induced property changes (effect known in some works as pump-probe modulations or nonlinear frequency mixing, see [36]).

Also it is insightful to note that probe modulation is directly related to the defect scattering cross-section defined in section 1.4. Variation of the scattering cross-section that will be studied in chapter 3, section 3.3, and interpenetration distance (and, consequently, force and displacement) are related by the unknown nonlinear relationship.

2.2.2 Measurements of displacement and strain induced by high frequency excitation using laser vibrometer

a) Estimation of displacement induced by high frequency signal : laser Doppler vibrometry

Laser doppler vibrometer (LDV) [96] experiment was performed with laser Polytec OFV 55 with a decoder VD-09 at the regime « measurements of velocity » with 5mm/s/V precision, sampling frequency 1MS/s with averaging over 1024 acquisitions. Experimental setup consists of a fiber laser vibrometer, LDV controller and oscilloscope (see fig. 2.7).

Synchronization was applied : emission signal generated with MOTU sound board was received directly by one of the oscilloscope channels and at the same time transmitted by the PZT transducer into the plate. Defect was located 25 cm away from the emitter. Laser was positioned under the plate at different locations : under emitter, under the defect and several locations in between. 50 ms bursts at 10 kHz were emitted with MOTU board (as in pump-probe experiments) during 140 s.

We obtained the following result : when amplitude of the probe is 5V$_{pp}$ at the plate (as we apply in experiments), it causes defect normal displacement around 1 nm.

b) Estimation of strain caused by a probe wave at source position

In case of an axisymmetric problem (isotropic plate and source located in the coordinates origin), strain in polar coordinates (r, θ) is given by [97] :

$$\begin{cases} \varepsilon_{rr} = \frac{\partial u_r}{\partial r} \\ \varepsilon_{\theta\theta} = \frac{u_r}{r} \end{cases} \tag{2.11}$$

Assuming that there is only A0 flexural mode in the plate within Kirchoff-Love model (see chapter 1, section 1.1), displacement can be written as :

$$\begin{cases} u_r = -z\frac{\partial w}{\partial r} \\ u_\theta = 0 \\ u_z = w \end{cases} \tag{2.12}$$

(a) Laser vibrometer experimental setup.

(b) Laser vibrometer controller.

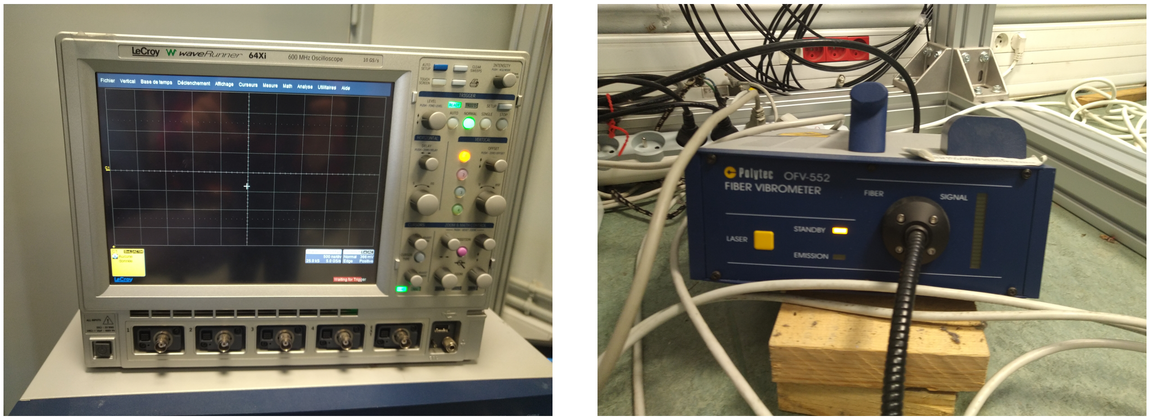

(c) Oscilloscope.

(d) Fiber vibrometer.

FIGURE 2.7 – Experimental setup for Laser Doppler vibrometry in order to measure velocity at the contact spot while emitting high frequency signal.

where w is a plate deflection.

Substituting the second system Eq. (2.12) into the first one Eq. (2.11), we get :

$$\begin{cases} \varepsilon_{rr} = -z\frac{\partial^2 w}{\partial r^2} \\ \varepsilon_{\theta\theta} = -\frac{z}{r}\frac{\partial w}{\partial r} \end{cases}$$

For a 2D propagation, a solution for the wave equation can be presented in the form of $w(r,\omega) = \frac{K(\omega)}{\sqrt{r}}e^{j(\omega t - kr)}$, where $K(\omega)$ depends on the source characteristics and type of emitted signal. It is difficult to determine this factor, but it will not affect the final result of this derivation. Applying of this expression of w into the previous system of equation leads to :

$$\begin{cases} \varepsilon_{rr} = z(\frac{1}{4r^2} + \frac{jk}{r} + k^2)w \\ \varepsilon_{\theta\theta} = z(-\frac{1}{2r^2} + \frac{jk}{r})w \end{cases}$$

Maximum of strain is obtained for $z = d$, i.e. on the surface of the plate. Thus, in the far-field approximation, maximum deformation can be estimated as :

$$\begin{cases} \varepsilon_{rr} \sim dk^2 w \\ \varepsilon_{\theta\theta} \sim 0 \end{cases}$$

For A0 flexion mode, wavenumber k within Kirchoff-Love model is given by Eq. (1.8), with bending stiffness D defined in Eq. (1.7).

For the laser vibrometry experiment described in a previous subsection the plate is made of aluminum : $E = 69$ GPa, $\nu = 0.35$, $\rho = 2700 kg/m^3$ with a thickness of $h = 3$ mm. Central frequency of excitation is $f = 10$ kHz. An estimated displacement is $w \sim 1$ nm. So the strain is equal to :

$$\varepsilon_{rr} \sim d \cdot 2\pi f \sqrt{2d\rho \frac{12(1-\nu^2)}{8Ed^3}} w = \pi f w \sqrt{\frac{12\rho(1-\nu^2)}{E}}$$

Substituting the problem parameters in the above equation, we can estimate deformation as

$$\varepsilon_{rr} \sim 2 \cdot 10^{-8}$$

This is 3 orders lower than pump-related strain ($\varepsilon_{pump} \sim 10^{-5}$), which means that conditions of pump-probe experiment are met.

2.3 Signal processing for damage localization and experimental results

In this section, details of signals processing for defect detection are described and obtained localization images are discussed.

2.3.1 Synchronous detection mode between pump and probe signals

We define differential signals $\Delta s_{m,n}$ by subtracting the extracted HF signals $s_{m,n}$ (signal in the m^{th} slice from the n^{th} receiver) and their averages over all M slices (see fig. 2.2) :

$$\Delta s_{m,n}(t) = s_{m,n}(t) - \frac{1}{M}\sum_{i=1}^{M} s_{i,n}(t) \tag{2.13}$$

Averaging is expected to cancel the defect contribution and only retain components of the signals associated to the plate itself and the sensor array configuration. Therefore the differential signals $\Delta s_{m,n}$ should essentially contain contributions of the defect [98]. Indeed, nonlinear defect is being revealed from contact modulations caused by the powerful pump that is three orders of magnitude stronger than the probe (see section 2.2), which allows to linearly separate a term related to the defect, whereas the averaged state cancels the modulations. We expect the defect to manifest as a very weak modulation comparing to reverberations, but this effect can be enhanced by averaging over different contact states.

Note that pump frequency $f_{pump} = 1$ Hz is far below the mechanical resonance frequency of the plate, so the defect can not correspond to a node or anti-node of a plate mode and defect signature is not hidden by high resonance amplitude. To prove this point, we performed the modal analysis of the plate. A shaker excited a plate with a chirp in a range of 1-200 Hz, we recorded this signal with an accelerometer at different locations on the plate. Then we averaged the square of absolute value of a signal spectrum over all the accelerometer locations and obtained the power spectral density of the plate that is presented in fig. 2.8. Most of the plate modes energy is distributed between 40 and 150 Hz that is much higher than $f_{pump} = 1$ Hz.

The defect localization procedure consists in constructing an image by processing these differential signals pixel by pixel, using a back-propagation based procedure

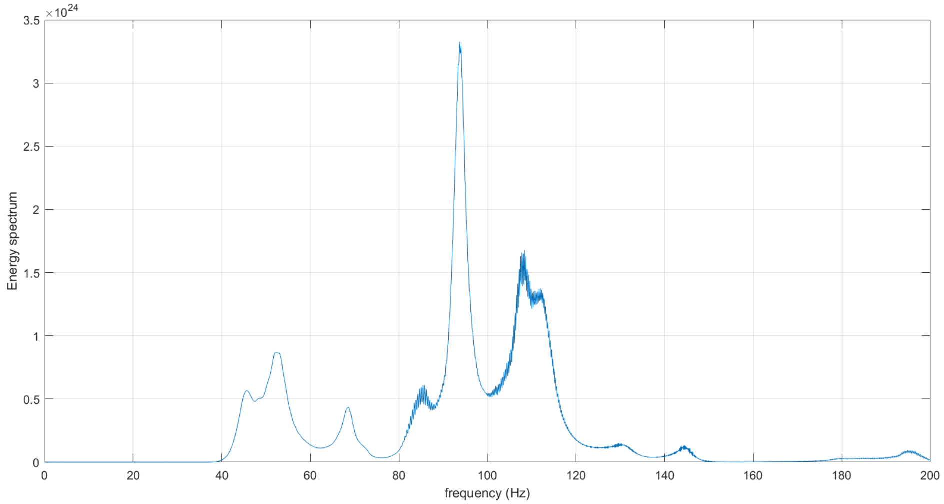

FIGURE 2.8 – Energy spectrum of the plate.

already exploited with success in previous works [68]. For clarity, we briefly describe below the main steps of this processing.

First, for a given pixel of coordinates (x, y) and a given signal slice m, differential signals are back-propagated over distances $r_n(x, y)$ between the emitter and the n^{th} receiver via the pixel. This is simply done through multiplication in the frequency domain by the complex conjugate of a propagation function $e^{-j\,\vec{k}\,\vec{r}}$:

$$F_{m,n}(x, y, \omega) = \Delta s_{m,n}(\omega)\, e^{j\,k(\omega)\,r_n(x,y)}, \tag{2.14}$$

where the wavenumber k fulfills the dispersion relation of A0 Lamb mode (flexural wave), which is largely dominant in the considered conditions (low frequency-thickness product and surface excitation). Then we construct so-called back-propagation function by summation over all receivers

$$bpf_m(x, y, \omega) = \sum_{n=1}^{N_r} F_{m,n}(x, y, \omega), \tag{2.15}$$

where N_r states for a number of receivers.

For pixels coinciding with the defect position, the back-propagation process will perfectly compensate for propagation phases and, back in the time-domain, the back-propagation function $bpf_m(x, y, t)$ will result in a constructive sum at zero time. On the contrary, for pixels at arbitrary positions, summed terms will have no particular phase relation.

In this work, two types of imaging are applied depending on how the information from the back propagation functions from the different slices is stacked : incoherent and coherent imaging.

a) Incoherent sum

According to the properties of the back-propagation function, the pixel intensity defined as

$$I_m(x,y) = \int_{-T_0/2}^{T_0/2} \left[bpf_m(x,y,t)\right]^2 \, \mathrm{d}t, \tag{2.16}$$

is expected to exhibit a local maximum at the defect location. Here T_0 is the duration of the emitted wavepacket (typically inverse of the bandwidth), and integration over the interval $[-T_0/2, T_0/2]$ allows to eliminate influence of reverberations outside this interval.

Finally, to enhance detection quality and reduce noise effects, averaging over all M slices is performed, resulting in

$$I_{inc}(x,y) = \frac{1}{M}\sum_{m=1}^{M} I_m(x,y), \tag{2.17}$$

where the subscript *inc* stands for « incoherent », since the final image is made up of incoherent summation (sum of energy terms) over all HF signal slices.

In accordance to the formulated principle, $I_{inc}(x,y)$ reaches a maximum when (x,y) coincides with the defect position. A graphical representation of $I_{inc}(x,y)$ thus constitutes a localization image of the defect.

Later in the results section c) we will see that incoherent imaging provides satisfactory defect detection but contains some speckle-like background artifacts. Those artifacts can be diminished by using an improved version of the imaging with coherent sum described in the next section.

b) Coherent sum : synchronous detection

In a refined version of the procedure, the back-propagation functions obtained for each HF slice can be coherently summed. To that end, we define

$$BPF(x, y, \omega) = \frac{1}{M} \sum_{m=1}^{M} a_m \, bpf_m(x, y, \omega) \tag{2.18}$$

where a_m is a set of ponderation coefficients aiming at ensuring that the summation will be constructive.

Indeed, since the contact at the defect location is continuously and alternatively modulated through the LF shaker, real part of excitation $s_{pump}(t)$, averaging with unitary ponderation ($a_m = 1$) should cancel the defect contribution. Instead, we will apply here the well-known principle of synchronous detection, by defining ponderation as

$$a_m = s_{pump}(T_m) \tag{2.19}$$

where $T_m = m\Delta T$ is the instant of the m^{th} HF emission (slice m). As explained in section 2.1.1, the pump vibration s_{pump} is easily extracted by low-pass filtering the received signals.

Then, similarly to Eq. (2.16), an image can be constructed from coherently summed back-propagation functions as in eq. (2.20)

$$I_{\text{coh}}(x, y) = \int_{-T_0/2}^{T_0/2} |BPF(x, y, t)|^2 dt \tag{2.20}$$

c) Localization results for synchronized experiments

The results of the experiments in comparison between coherent and incoherent imaging are shown in the fig. 2.9. Time interval between HF signal emissions is set as $\Delta T = 50$ ms and the LF pump is $f_{pump} = 1$ Hz, signals contain M=700 slices. The defect position is marked with a black circle, the crosses correspond to receivers R_n. Two defect positions are tested : one inside the receiver array and one outside it.

Both defect positions are correctly detected through localized higher-intensity spots on the images. Note that the fact that the spot corresponding to the defect outside the receiver array is larger than the one inside is coherent with the well-known diffraction laws relative to the array aperture.

In incoherent images (figs. 2.9a, 2.9c) speckle-like background noise is observed. It is mostly related to incoherent averaging of intensities in Eqs. (2.16) and (2.17), which does not suppress all of experimental noise and reverberation contributions.

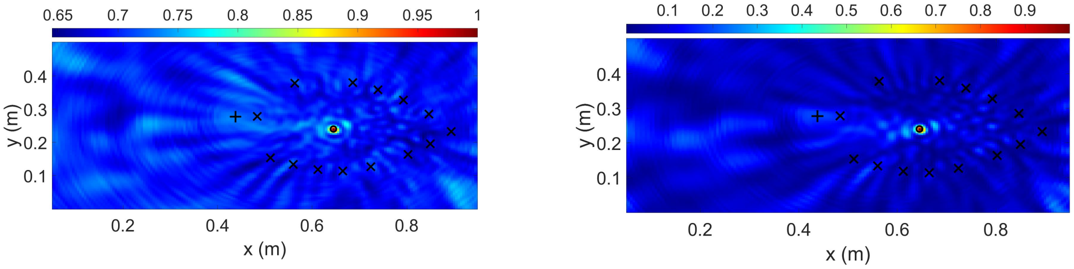

(a) Incoherent image : defect (0.645, 0.24).

(b) Coherent image : defect (0.645, 0.24).

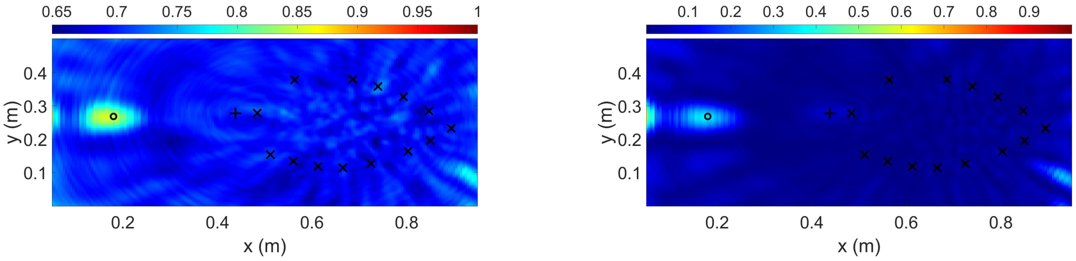

(c) Incoherent image : defect (0.18, 0.268).

(d) Coherent image : defect (0.18, 0.268).

FIGURE 2.9 – Localization results for synchronized experiments with incoherent imaging (left column) and coherent imaging with synchronous detection (right column).

To remedy that, coherent images (Eq. (2.20)) obtained from the same experimental recordings have been computed as well. They are shown in figs. 2.9b, 2.9d. The benefit of synchronous detection application, resulting in coherent and constructive summation of the back-propagation function, on the image quality is obvious.

To make a quantitative comparison between incoherent and coherent imaging, image contrast is introduced. A classical definition of image contrast is the so-called Weber contrast, defined as

$$\mathcal{C} = \frac{I_{def} - I_{av}}{I_{av}} \tag{2.21}$$

where I_{def} is the intensity value at the defect position and I_{av} is the average intensity value of the image excluding the defect area.

Computed contrasts for incoherent and coherent images for the first defect location are $\mathcal{C}_{inc} = 4.7$ (fig. 2.9a) and $\mathcal{C}_{coh} = 14.8$ (fig. 2.9b), respectively. For the second defect location they are $\mathcal{C}_{inc} = 2.4$ (fig. 2.9c) and $\mathcal{C}_{coh} = 12.2$ (fig. 2.9d). This corresponds to a factor 3 to 5 of contrast improvement when applying the pump-probe technique in a synchronous coherent way.

2.3.2 Non-synchronous detection mode using back-propagation technique

Here the signal processing and the results of the non-synchronized pump-probe experiments are presented. The experimental setup for them is described in section 2.1.2. First, we will see the results of incoherent imaging.

a) Incoherent sum : results

In order to collect information from different contact states, signal slices $s_{m,n}$ of duration ΔT are subtracted from each other, so for each pair of slices $(m_1, m_2) \equiv p$ there is a differential signal :

$$\Delta s_{p,n} = s_{m_1,n} - s_{m_2,n}$$

And then P randomly selected pairs of loading states produce P differences $\Delta s_{p,n}$ that are taken into account for a back-propagation localization algorithm. So to apply the incoherent imaging algorithm described for synchronized experiments in section 2.3.1, it is required to replace $\Delta s_{m,n}$ with $\Delta s_{p,n}$ and M with P respectively that yields :

$$I_p(x,y) = \int_{-T_0/2}^{T_0/2} \left[bpf_p(x,y,t)\right]^2 \,\mathrm{d}t, \tag{2.22}$$

and

$$I_{inc}(x,y) = \frac{1}{P}\sum_{p=1}^{P} I_p(x,y)\,. \tag{2.23}$$

The results of the described algorithm obtained for $P = 20$ differences are demonstrated below. Defect is denoted with a black circle, white square refers to shaker, PZTs are depicted as white asterisks, the letter E is for emitter.

The first series of experiments (fig. 2.10) is to examine different PZT patches playing the role of emitter. The algorithm works more or less regardless the emitter position, but better when emitter is far from the boundaries. The best images were obtained with transducers R_1 at (0.512,0.153) m and R_8 at (0.484, 0.28) m as emitters. So in the further series of experiments only these two are used.

The second series of experiments is concerned with a study of the pump frequency dependency of the image quality. It turns out, that for all the frequencies in the range of [0.5-4] Hz with a certain pump amplitude, location of the defect can be found correctly (see fig. 2.11). Whilst for frequencies higher than frequency threshold $f_{max} \sim 4$ Hz localization is hardly possible (as in the two last images of fig. 2.11).

Two types of the defect's motion are observed : « horizontal » and « vertical ». « Horizontal » motion is a motion in which a sphere moves along elliptical trajectory on the plate surface. « Vertical » motion is the motion regime in which sphere is stationary in relation to the plate, its coordinate is constant and only the contact force is modulated. In fig. 2.11 two transitions between « vertical » and « horizontal » modes are observed : below f_1=1 Hz and above f_2=1.5 Hz motion is « vertical » while between f_1 and f_2 it is « horizontal ». Later in this work « horizontal » motion is avoided in order to make the artificial CAN behavior closer to a crack whose coordinate does not change with vibrations.

If the pump amplitude is too high, squealing appears, signals contain extra spikes, algorithm does not work. Since we are interested here in the effect of the CAN modulation under low frequency vibrations (not acoustic emission), this situation is avoided.

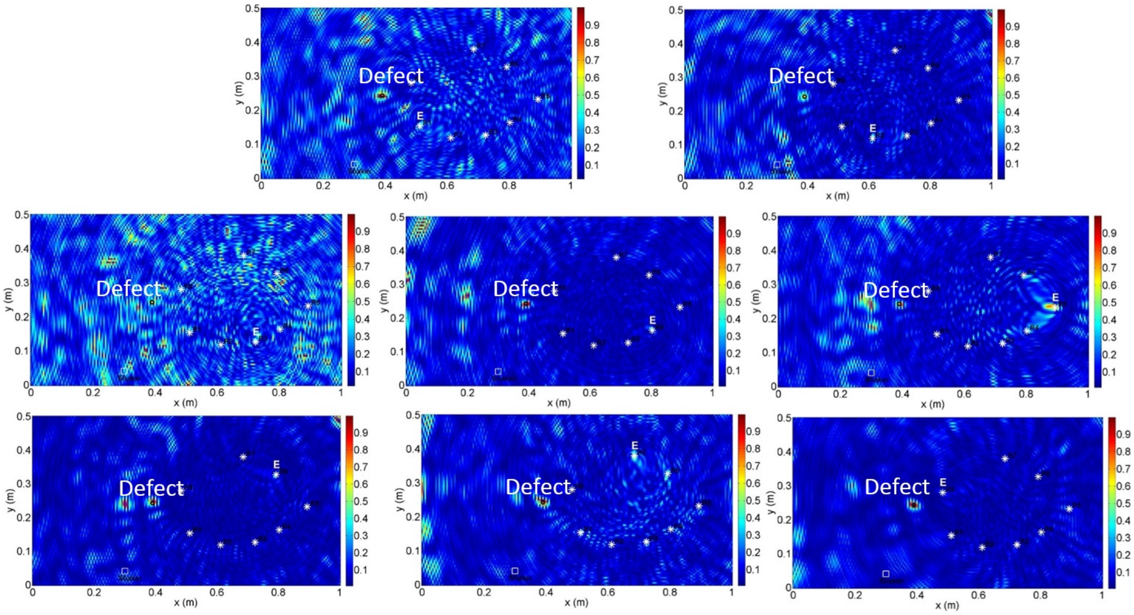

FIGURE 2.10 – Imaging localization results : different PZTs play role of emitter.

If the pump amplitude is too high, squealing appears, which adds non-stationary noise to the recorded signals and interferes with the work of the proposed detection method. Acoustic emission based methods e.g. in [100] are robust for squealing. Since we are interested here in the effect of the CAN modulation under low frequency vibrations (not acoustic emission), this situation is beyond the scope of this thesis.

The third series of experiments (see left column on the fig. 2.12) was focused on different defect locations. There are three locations : inside transducers zone at (0.615, 0.297) m, outside transducers zone at (0.39, 0.244) m and close to the boundaries at (0.39, 0.10) m. Algorithm works for different defect positions, even when it is close to the boundaries.

b) Coherent sum : random sign compensation

In many images obtained with incoherent sum, the contrast is not optimal : there is speckle-like background noise due to high side lobes. To improve localization images quality while keeping in mind idea about cumulation of information from repetitive probings, random sign compensation technique is proposed here.

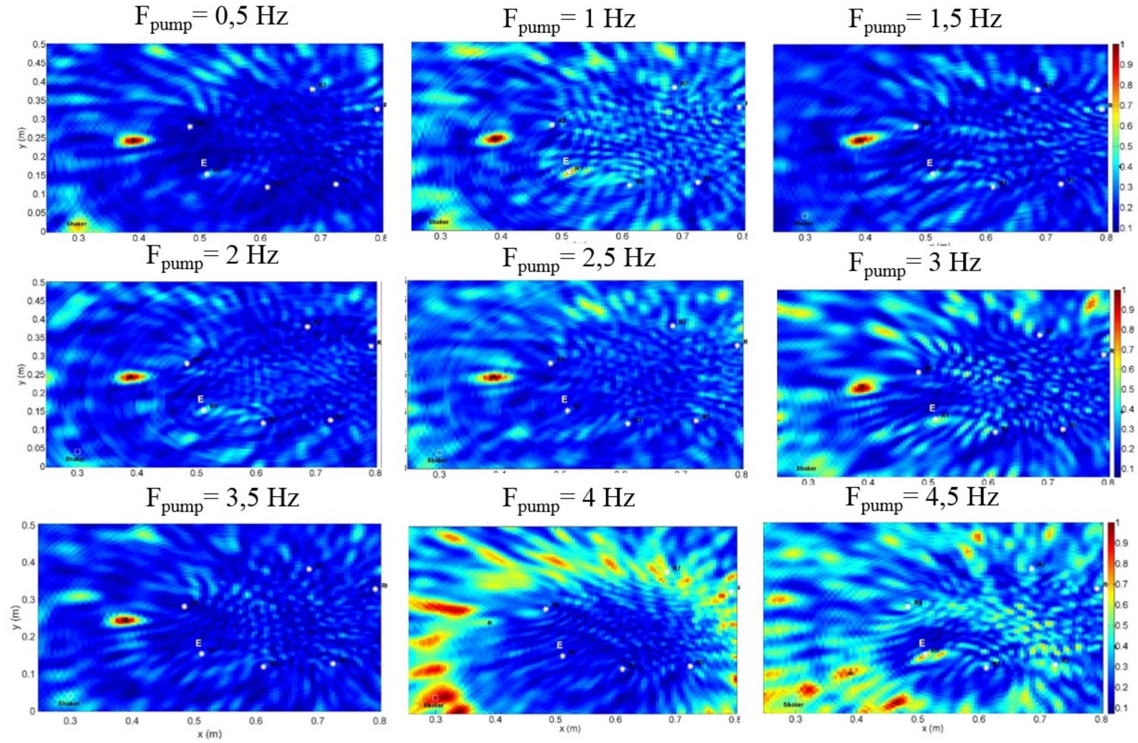

FIGURE 2.11 – Imaging localization results at different pump frequencies. Defect is located at (0.39, 0.244) m.

The sum in Eq. (2.17) is incoherent, which means that the phase information of back-propagation function (i.e. of scattered field) is discarded.

If signs of the defect strength a_p under different loading states were known (p refers to the pair of loading states), it would be easy to calculate this sum. However, signs of the scattering amplitude are arbitrary and unknown in the experiment. Unlike in synchronized experiments, synchronous detection is not an option here, since pump and probe are excited independently. Within so-called random sign compensation technique, ponderation coefficients are defined as : $a_p = +1$ or -1, depending on conditions discussed below. The pixel intensity is then defined in time domain coherently by Eq. (2.20).

The optimal case would obviously be achieved if the actual sign sequence would be known. Then, replacing a_p by α_p in Eq. (2.18) and applying Eq. (2.20) on the obtained BPF would yield the pixel intensity corresponding to the optimal image :

$$I_{\text{opt}}(x, y) = I_{\text{coh}}(x, y)\big|_{(a_p=\alpha_p)} \tag{2.24}$$

In practical situations, this optimal image is not accessible, since α_p is unknown.

After obtaining an image, one should test quite a large number of different sign sequences. We will seek to find the set of $[a_p]$ that maximizes the apparent image contrast $\mathcal{C}$ defined in Eq. (2.21), which is in this case equivalent to :

$$\mathcal{C}([a_p]) = \frac{\max\limits_{(x,y)} \left[I_{\text{coh}}(x, y)\big|_{a_p} \right]}{\frac{1}{N_{\text{pixel}}} \sum\limits_{(x,y)} I_{\text{coh}}(x, y)\big|_{a_p}} - 1 \tag{2.25}$$

here N_{pixels} stands for the number of considered candidate defect positions.

Since the actual sign sequence is unknown, exact solution of this optimization problem is not applicable. Instead, a Monte-Carlo estimation [101] – substituting a deterministic process with a stochastic one – can be easily implemented. The idea of Monte Carlo technique here is to repeat imaging with different randomly generated sign vectors statistically significant number of times to find a vector corresponding to maximum contrast based on the Law of Large Numbers. The details about statistical inference of contrast estimation with onte Carlo simulation are given further in section 3.1.3. Briefly, a set of W candidate sign vectors $[a_p]_w$ $(1 \leq w \leq W)$ will be randomly selected. The retained vector $[\beta_p]$ among this set is then the one satisfying best the optimization problem. Formally, this can be written as

$$[\beta_p] = \underset{\substack{[a_p]_w \\ (1 \leq w \leq W)}}{\arg\max}\, \mathcal{C}([a_p]_w) \tag{2.26}$$

The image obtained using this selected vector is then defined as :

$$I_{\text{sel}}(x, y) = I_{\text{coh}}(x, y)|_{(a_p = \beta_p)} \tag{2.27}$$

c) Localization results for non-synchronized experiments

This post-processing is then applied for some cases of different defect positions where image contrast is relatively low. In fig. 2.12 the obtained results for incoherent imaging and coherent imaging with random sign compensation are shown for $W = 1000$ different sign sequences and $P = 20$ differences.

Sign compensation leads to a clear contrast improvement. This will be theoretically discussed in the next chapter.

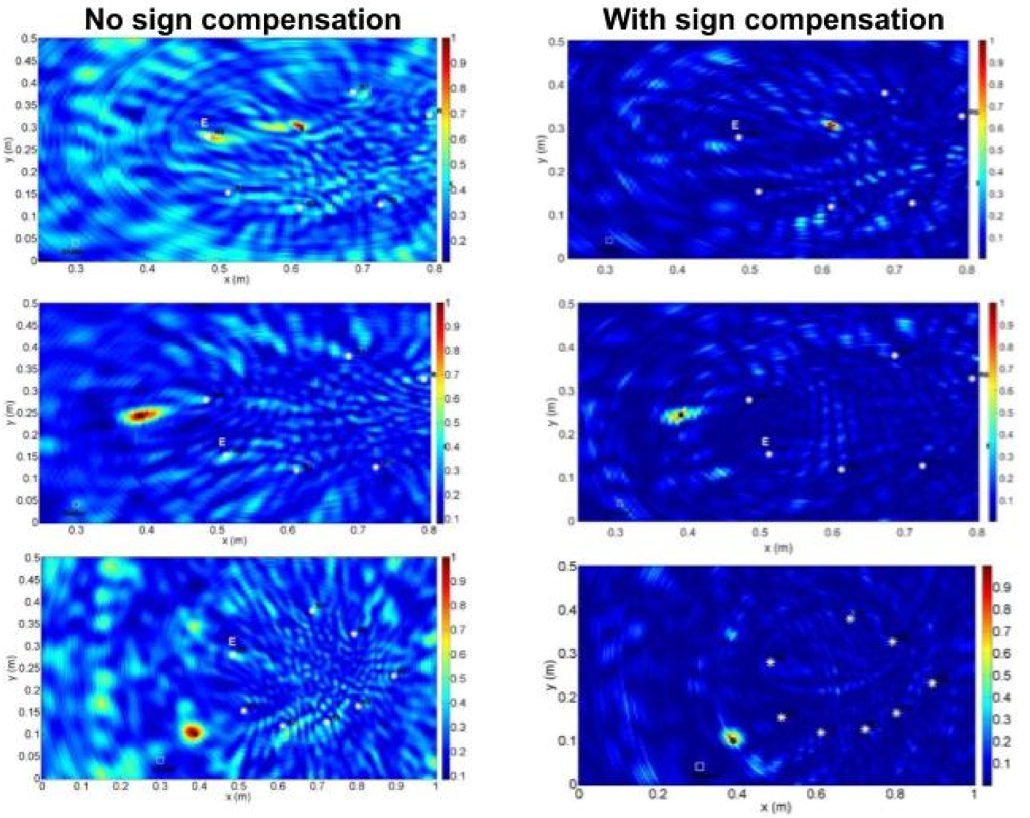
No sign compensation

With sign compensation

Figure 2.12 – Imaging localization results at different defect locations at pump frequency 1.5 Hz : incoherent imaging (left column) and coherent imaging with random sign compensation (right column). White letter *E* stands for the emitter position : (0.484, 0.278) in top and bottom images, (0.512, 0.153) in the middle ones. White square is for the shaker position (0.3, 0.02).

Conclusions

An active reference-free damage localization algorithm in thin plates based on a combination of repetitive probing with back-propagation of signals has been developed. The algorithm is capable of detecting modulated Hertzian-like contact defects. Two kinds of experiment have been done : when a pump wave is synchronized with a probe wave (synchronized experiments) and when it is not (non-synchronized experiments).

To improve localization image contrast, we performed coherent imaging using two techniques : classical synchronous detection and random sign compensation. The latter offers an elegant and practical way to optimize imaging without synchronization.

Displacement induced by pump wave at 1 Hz is estimated in a range of tenths of mm, whereas displacement induced by probe at 10 kHz is smaller by six orders : around 1 nm. The difference in strains is three orders of magnitude : 10^{-5} and 10^{-8} for pump- and probe-induced strain, respectively. Our experiment belongs to a linear part of stress-strain curve, nonlinearity is essentially in pump-probe interaction. A quantitative study on influence of other parameters such as defect scattering characteristics on the image contrast is derived in the next chapter.

Chapter 3

Quantitative analysis of image contrast and parametric study

Contents

Introduction

The purpose of this chapter is to find limitations of the developed detection technique described previously and quantify the involved parameters and their influence on image contrast. Therefore, theoretical derivation and experimental study of what the image contrast depends on are described. Quantification of CAN scattering cross-section is also performed.

3.1 Theoretical estimations of contrast

Let us consider a plate equipped with an ultrasound emitter E and N_r receivers R_i. We also assume the presence in the plate of a local heterogeneity. This defect interacts with ultrasound probe waves with a given strength directly related to its state at the instant of recording. Formally, the signal recorded at the i^{th} receiver when the defect is in the m^{th} state can be expressed as :

$$s_{m,i}(t) = s_{0,i}(t) + f_m(\theta_i)\,\Delta s_{0,i}(t) + n_{m,i}(t) \tag{3.1}$$

where $s_{0,i}$ is the defect-free signal, f_m is the defect scattering amplitude (far-field pattern) defined for a plane wave, θ_i the direction angle of the i^{th} receiver, $n_{m,i}$ an experimental additive noise and $\Delta s_{0,i}$ the wave signal scattered by the defect, whose Fourier transform is given by

$$\Delta s_{0,i}(\omega) = \delta_i\, u_0(\omega)\; e^{-jk(\omega)\,(d_1+d_{2_i})} \tag{3.2}$$

with $\delta_i = 1/\sqrt{d_1 d_{2_i}}$ the geometrical spreading factor, d_1 and d_{2_i} the distances from the emitter to the defect and from the defect to receiver R_i, respectively, and u_0 the emission signal :

$$u_0(t) = \begin{cases} \frac{A}{2}(1-\cos\omega_0 t)\sin\omega_0 t\,, & 0 \le t \le \frac{2\pi}{\omega_0} \\ 0\,, & t > \frac{2\pi}{\omega_0} \end{cases}$$

with amplitude A centered at angular frequency ω_0.

For simplification purposes, we will assume in the following that the defect behavior is isotropic, implying that f_m is independent from θ_n.

Considering a set of two recordings $(m_1, m_2) \equiv p$ in two different defect states, the associated differential signal is then defined as

$$\Delta s_{m,i}(t) = s_{m_2,i}(t) - s_{m_1,i}(t) = Z_p \, \Delta s_{0,i}(t) + \Delta n_{p,i} \tag{3.3}$$

with $Z_p = f_{m_2} - f_{m_1}$ and $\Delta n_{p,i} = n_{m_1,i} - n_{m_2,i}$.

We consider here that $n(t)$ is a zero-mean additive Gaussian noise with variance σ_n^2 affecting the recorded signals. Presence of this noise will result in a non-zero, speckle-like, background on the images, even in the absence of a defect. The defect detection contrast will then be evaluated based on the definition from Eq. (2.21).

First we will derive contrast expression in the simplest case of all, which is static differential detection (i.e. subtraction of signals with and without defect, as developed in [68]). Then we will adapt the derivation to the cases considered in chapter 2 of this manuscript : dynamic incoherent (I_{inc} in Eq. (2.17)) and coherent (I_{coh} in Eq. (2.20), I_{opt} in Eq. (2.24), I_{sel} in Eq. (2.27)) imaging.

3.1.1 Static differential detection

a) Residual speckle without defect

In the defect-free case, $f_{m_1} = f_{m_2} = 0$ and therefore from Eq. (3.3) the recorded differential signals would be :

$$\Delta s_{p,i}(t) = \Delta n_{p,i}(t) \ , \ \forall p \tag{3.4}$$

with $\Delta n_{p,i}$ the differential noise, i.e. difference between two independent realizations of noise $n(t)$, thus, its variance can be expressed as :

$$\sigma_{\Delta n}^2 = 2\sigma_n^2 \tag{3.5}$$

From Eq. (2.16) the averaged pixel intensity for a single pair of loading states :

$$\langle I_p \rangle = T_0 \left\langle \mathrm{bpf}_p^2 \right\rangle = T_0 \, \sigma_{\mathrm{bpf}_p}^2 \tag{3.6}$$

Considering that back-propagated noises from each receiver are uncorrelated, Eq. (2.15) yields :

$$\sigma_{\mathrm{bpf}_p}^2 = N_r \sigma_{F_{p,i}}^2 \tag{3.7}$$

Using Parseval's theorem, under the assumption of a stationary ergodic random process, the variance of $F_{p,i}$ can be expressed as average power :

$$\sigma^2_{F_{p,i}} = \int_{-\infty}^{+\infty} S_{F_{p,i},F_{p,i}}(\omega)\, d\omega \tag{3.8}$$

where $S_{\mathrm{bpf}_{i,p},\mathrm{bpf}_{i,p}}$ is the power spectral density of $\mathrm{bpf}_{i,p}$.

Eq. (2.14) can be considered as a relation between the input and the output of a linear invariant system of the form $Y(\omega) = G(\omega)X(\omega)$. Then using the consequence of the Wiener-Khinchin theorem for power spectral densities of stationary processes $S_{Y,Y}(\omega) = |G(\omega)|^2\, S_{X,X}(\omega)$ with $G(\omega) = e^{jkd_i}$, we can immediately deduce :

$$S_{F_{p,i},F_{p,i}}(\omega) = S_{\Delta s_{p,i},\Delta s_{p,i}}(\omega) \tag{3.9}$$

and

$$\sigma^2_{F_{p,i}} = \int_{-\infty}^{+\infty} S_{\Delta s_{p,i},\Delta s_{p,i}}(\omega)\, d\omega = \sigma^2_{\Delta s_{p,i}} \tag{3.10}$$

Finally, substituting Eq. (3.5) in Eq. (3.10) and using it in Eq. (3.7), yields :

$$\sigma^2_{\mathrm{bpf}_p} = 2N_r\sigma_n^2 \tag{3.11}$$

and then using Eq. (3.6), we get

$$\langle I_p \rangle = 2N_r\, T_0\, \sigma_n^2 \tag{3.12}$$

b) Defect-related spot

The pixel intensity at the defect location is estimated from the back-propagation functions defined by Eq. (2.14) when $\Delta s_{p,i}$ corresponds to Eq. (3.3) along with Eq. (3.2) and $d_i = d_1 + d_{2_i}$ (pixel at the defect). This yields

$$F_{p,i}(t) = Z_p\, \delta_i\, u_0(t) + \Delta n'_{p,i}(t) \tag{3.13}$$

where $\Delta n'_{p,i}$ is the back-propagated version of $\Delta n_{p,i}$.

Then Eq. (2.15) yields

$$\mathrm{bpf}_p(t) = Z_p N_r\, \overline{\delta}\, u_0(t) + N_p(t) \tag{3.14}$$

where $\overline{\delta}$ is a geometrical spreading factor averaged over receivers :

$$\overline{\delta} = \frac{1}{N_r}\sum_{i=1}^{N_r}\delta_i \tag{3.15}$$

and

$$N_p(t) = \sum_{i=1}^{N_r}\Delta n'_{p,i}(t) \tag{3.16}$$

Introducing Eq. (3.14) into Eq. (2.16) yields

$$I_p = Z_p^2 N_r^2\,\overline{\delta}^2\,E_0 + \int_{-T_0/2}^{T_0/2} N_p^2(t)\mathrm{d}t + X \tag{3.17}$$

with $X = 2Z_pN_r\overline{\delta}\int_{-T_0/2}^{T_0/2} u_0(t)N_p(t)\mathrm{d}t$ the cross-term and where E_0 is energy radiated by emitter during T_0 :

$$E_0 = \int_{-T_0/2}^{T_0/2} u_0^2(t)\,dt \tag{3.18}$$

Since $\langle X\rangle = 0$, taking the expected value over time of Eq. (3.17) yields

$$\langle I_p\rangle = Z_p^2 N_r^2\,\overline{\delta}^2\,E_0 + 2N_rT_0\sigma_n^2 \tag{3.19}$$

In the case of static differential imaging (subtraction of signals with and without the defect), Z_p^2 is directly related to the scattering cross-section σ_0 of the defect defined in Eq. (1.11). $f(\theta,\omega)$ is assumed to be constant in a narrow frequency band centered at ω_0. Then a scattering cross-section at a frequency ω_0 can be expressed as

$$\sigma(\omega_0) = \int_0^{2\pi}|f(\theta,\omega_0)|^2 d\theta \equiv \sigma_0 \tag{3.20}$$

If states m_1 and m_2 correspond to the cases without and with defect, respectively, then $f_{m_1}(\theta) = 0$ and $f_{m_2}(\theta) = f(\theta)$. This yields $Z_p = f_{m_2} - f_{m_1} = f(\theta)$ and therefore, under our isotropic scatterer assumption $f(\theta,\omega)\equiv f(\omega)$

$$\sigma_0 = 2\pi Z_p^2 \tag{3.21}$$

Eq. (3.19) then yields

$$\langle I_p\rangle = \frac{N_r^2\overline{\delta}^2 E_0\sigma_0}{2\pi} + 2N_rT_0\sigma_n^2 \tag{3.22}$$

c) Expressions of defect detection contrasts

I_{def} and I_{av} from the contrast definition in Eq. (2.21) correspond here to the previously-derived expected intensity values $\langle I_p \rangle$ given in Eqs. (3.22) and (3.12), respectively :

$$I_{def} = \frac{N_r^2 \overline{\delta}^2 E_0 \sigma_0}{2\pi} + 2N_r T_0 \sigma_n^2 \tag{3.23}$$

and

$$I_{av} = 2N_r\, T_0\, \sigma_n^2 \tag{3.24}$$

Therefore contrast defined in Eq. (2.21) can be written as

$$\mathcal{C} = \gamma \chi \sigma_0 \tag{3.25}$$

where

$$\gamma = \frac{N_r \overline{\delta}^2}{4\pi} \tag{3.26}$$

is a term related to the geometrical configuration of the sensor network with $\overline{\delta}$ defined in Eq. (3.15), and

$$\chi = \frac{E_0}{T_0 \sigma_n^2} \tag{3.27}$$

is the emission signal-to-noise ratio.

It is important to note that the expression of the contrast given in Eq. (3.25) does not take into account reverberation in the plate. Indeed, since only the first wave arrivals are considered, the result is theoretically valid for an unbounded plate. However, reverberation will essentially affect the parts of the image close to the plate boundaries. For a defect near the plate center, an image centered around this defect location should be relatively similar to ours without taking reverberation into account.

Another effect that is not taken into account in the derivation above is the diffraction-related side lobes in the image. These lobes are related to the sensor network geometrical configuration. They will induce a saturation of contrast for high values of the scattering cross-section, since the image background will be dominated by them. For small σ_0 values, contrast is essentially affected by measurement noise $n(t)$, as is assumed in our derivation.

Thus theoretical contrast expression given in Eq. (3.25) constitutes a linear approximation valid for moderate σ_0. This will be verified through simulation below and by experimental results further in section 3.2.2.

d) Wave scattering simulation in an infinite thin plate

In order to confirm the theoretically obtained contrast and scattering cross-section relationship described in this section, there has been developed a wave scattering simulation in a thin plate.

We assume that received signal in frequency domain is equal to emitted signal multiplied by a propagation factor depending only on distance between emitter and receiver. So neither absorption, nor boundary reflections are taken into account : it is infinite plate approximation. We assume also a single propagating Lamb mode in the plate, i.e. flexural wave which corresponds to low-frequency approximation of A0 mode. This assumption is taken according to the experimental condition discussed previously where A0 mode is dominant in the frequency range of 1-20 kHz for asymmetric vertical excitation (displacements of different signs from top and bottom surfaces of the plate).

As an emission signal u_e we use one-cycle of sine with Hanning window at $f_{em} = 10$ kHz of duration $\Delta t = 50$ ms. A direct received signal u_{dir} in frequency domain can be expressed as :

$$u_{dir}(\omega) = \frac{1}{\sqrt{r_{ER}}} u_e(\omega) e^{-ik(\omega)\, r_{ER}}\,, \tag{3.28}$$

where r_{ER} is an emitter-receiver distance, $k(\omega)$ is a wavenumber corresponding to A0 mode.

Then to simulate scattering from the defect, signals propagating from emitter to receiver via the defect are multiplied by a scattering amplitude $f(\theta, \omega_0)$ at angular frequency $\omega_0 = 2\pi f_{em}$ and scattering angle θ. It will be shown in section 5.2 that the defect-plate contact size ($\sim 10^{-5}$ m) is much smaller than the central wavelength ($\sim$ some cm), so the scatterer can be considered point-like with a known scattering amplitude $f(\theta, \omega_0)$. In this simulation, under assumptions of isotropic defect and narrow band, scattering amplitude is constant $f(\theta, \omega_0) \equiv f_d$. So the scattered signal is defined as :

$$u_{sc} = f_d \frac{1}{\sqrt{r_{EdR}}} u_e(\omega) e^{-ik(\omega)\, r_{EdR}}\,, \tag{3.29}$$

where r_{EdR} is a sum of distances from the emitter to the defect and from the defect to the receiver.

We also add some Gaussian noise u_{noise} to the received signal to break the perfection of simulation with a given variance σ_n^2.

As a result, total signal at the receiver is a sum of direct signal from emitter, scattered signal and noise.

$$u_r = u_{dir} + u_{sc} + u_{noise} \tag{3.30}$$

The relationship between the scattering amplitude $f(\omega_0, \theta)$ and the scattering cross-section is established in Eq. 1.11 which in case of constant $f(\omega_0, \theta) = f_d$ is equivalent to :

$$f_d = \sqrt{\frac{\sigma}{2\pi}} \tag{3.31}$$

This formula allows one to get scattering amplitudes f_d corresponding to the values of scattering cross-sections σ obtained in the experiment described above. For each f_d a simulation of wave scattering in an infinite plate was performed and then by applying back-propagation algorithm for active static experiments localization images were obtained and image contrast was estimated as in Eq. (2.21) along with Eq. (3.82).

Fig. 3.1 illustrates dependency of an image contrast on a defect scattering cross-section. A continuous line represents theoretical equation derived in this section, $\mathcal{C} = \chi\gamma\sigma$, stars connected with lines represent results from the infinite plate simulation. It is observed that at low values of scattering cross-section theoretical approximation agrees with infinite plate simulation, whereas when σ exceeds a certain threshold simulation curve experiences saturation deviating from a theoretical line.

This can be explained by the various nature of dominant image background noise for different scattering cross-sections. For small σ values, electronic noise plays the dominating role, as assumed in the derivation of theoretical formula Eq. (3.25) for the contrast, therefore, theoretical line agrees well with simulations and experimental data. However, for high σ values, diffraction-related side lobes from sensor network become essential, which causes the contrast saturation.

The theoretical formula for contrast Eq. (3.25) allows to estimate a detection scattering cross-section threshold σ_{th}. Indeed, assuming that minimal acceptable contrast is equal to 1, $\sigma_{th} = \frac{1}{\gamma\chi}$, which for the performed simulations was around 0.065 mm.

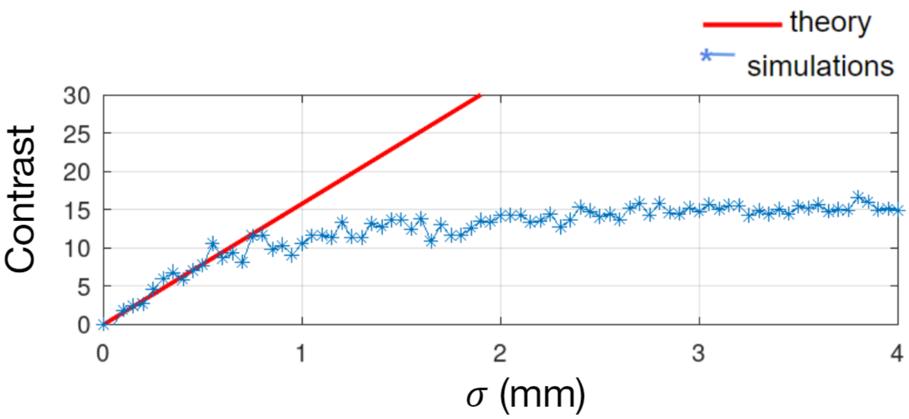

FIGURE 3.1 – Image contrast versus defect scattering cross-section for active static case : theoretical approximation and scattering simulation in an infinite plate.

3.1.2 Synchronized pump-probe detection

In this section, the image contrast for detection process applied in section 2.3.1 is estimated.

Eqs. (2.13) and (3.1) yield

$$\Delta s_{m,i}(t) = (f_m - \bar{f_m})\, \Delta s_{0,i}(t) + n_{m,i}(t) \tag{3.32}$$

where $\bar{f_m}$ is the average defect strength over pump vibration.

a) Residual speckle

In the defect-free case, $f_m = 0$ and therefore :

$$\Delta s_{m,i}(t) = n_{m,i}(t) \tag{3.33}$$

Incoherent imaging

Taking expected value of Eq. (2.16), we get :

$$\langle I_m \rangle = T_0 \left\langle \mathrm{bpf}_m^2 \right\rangle = T_0\, \sigma^2_{\mathrm{bpf}_m} \tag{3.34}$$

Here again, considering that back-propagated noises from each receivers are independent yields

$$\sigma^2_{\mathrm{bpf}_m} = N_r \sigma^2_{F_{m,i}} \tag{3.35}$$

with

$$\sigma^2_{F_{m,i}} = \sigma^2_{\Delta s_{m,i}} = \sigma^2_n \tag{3.36}$$

Thus

$$\langle I_m \rangle = N_r\, T_0\, \sigma^2_n \tag{3.37}$$

Finally Eq. (2.17) implies $\langle I_{\mathrm{inc}} \rangle = \langle I_m \rangle$ and thus

$$\langle I_{\mathrm{inc}} \rangle = N_r\, T_0\, \sigma^2_n \tag{3.38}$$

Coherent imaging

Eqs. (2.20) and (2.18) yield respectively

$$\langle I_{\mathrm{coh}} \rangle = T_0 \left\langle BPF^2 \right\rangle \tag{3.39}$$

and

$$\left\langle BPF^2 \right\rangle = \frac{1}{M}\sigma^2_{\mathrm{bpf}_m} = \frac{1}{M} N_r\, \sigma^2_n \tag{3.40}$$

Therefore

$$\langle I_{\mathrm{coh}} \rangle = \frac{1}{M} N_r\, T_0\, \sigma^2_n \tag{3.41}$$

b) Defect-related spot

Based on derivation presented in section 3.1.1 along with Eq. (3.32), it is easy to show that the pixel intensity on the defect is

$$\langle I_{\mathrm{inc}} \rangle = N_r^2\, \bar{\delta}^2\, E_0\, \frac{1}{M} \sum_{m=1}^{M} g_m^2 + N_r\, T_0\, \sigma^2_n \tag{3.42}$$

for incoherent imaging and

$$\langle I_{\mathrm{coh}} \rangle = N_r^2\, \bar{\delta}^2\, E_0 \left[\frac{1}{M} \sum_{m=1}^{M} a_m g_m \right]^2 + \frac{N_r\, T_0\, \sigma^2_n}{M} \tag{3.43}$$

for coherent imaging with $g_m = f_m - \bar{f_m}$.

We will consider here an average scattering cross-section over the modulated defect states :

$$\bar{\sigma}_0 = \frac{1}{M} \sum_{m=1}^{M} \sigma_{0_m} \tag{3.44}$$

where σ_{0_nm} is defined as a modified version of Eq. (3.21) :

$$\sigma_{0_m} = 2\pi g_m^2 \tag{3.45}$$

Therefore $\frac{1}{M} \sum g_m^2 = \bar{\sigma}_0 / 2\pi$ and Eq. (3.42) yields

$$\langle I_{\text{inc}} \rangle = \frac{N_r^2 \, \bar{\delta}^2 \, E_0 \, \bar{\sigma}_0}{2\pi} + N_r \, T_0 \, \sigma_n^2 \tag{3.46}$$

The pump modulation is expected to cause a periodic variation of the defect strength, which we will assume to be a sine waveform. Therefore we will consider

$$g_m = A \cos(\omega_p t_m) \tag{3.47}$$

where ω_p is the pulsation of the pump vibration.

In the synchronous detection procedure described in section 2.3, the weighting coefficients a_m are thus given, in accordance with Eq. (2.19), as

$$a_m = \cos(\omega_p t_m) \tag{3.48}$$

Under those assumptions, we have

$$\frac{1}{M} \sum_{m=1}^{M} g_m^2 \simeq \frac{1}{T_p} \int_0^{T_p} A^2 \cos^2(\omega_p t_m) \, dt = \frac{A^2}{2} \tag{3.49}$$

and

$$\frac{1}{M} \sum_{m=1}^{M} a_m g_m \simeq \frac{1}{T_p} \int_0^{T_p} A \cos^2(\omega_p t_m) \, dt = \frac{A}{2} \tag{3.50}$$

which yield respectively :

$$\frac{A^2}{2} = \frac{\bar{\sigma}_0}{2\pi} \tag{3.51}$$

and

$$\left[\frac{1}{M}\sum_{m=1}^{M} a_m g_m\right]^2 = \frac{A^2}{4} \tag{3.52}$$

Consequently

$$\left[\frac{1}{M}\sum_{m=1}^{M} a_m g_m\right]^2 = \frac{\bar{\sigma}_0}{4\pi} \tag{3.53}$$

and thus from Eq. (3.43)

$$\langle I_{\text{coh}}\rangle = \frac{N_r^2\,\bar{\delta}^2\,E_0\,\bar{\sigma}_0}{4\pi} + \frac{N_r\,T_0\,\sigma_n^2}{M} \tag{3.54}$$

c) Contrast expressions

Contrast can be deduced in incoherent and coherent cases from Eqs. (3.46) and (3.38), and Eqs. (3.54) and (3.41), respectively :

$$C_{\text{inc}} = 2\gamma\chi\bar{\sigma}_0 \tag{3.55}$$

and

$$C_{\text{coh}} = M\gamma\chi\bar{\sigma}_0 \tag{3.56}$$

where γ and χ are defined as in the static case above (Eq. (3.26) and Eq. (3.27), respectively).

We see here that theoretical contrast in coherent imaging is $M/2$ times the one in incoherent imaging. Actually, this contrast improvement is limited by the asymptotic contrast value caused by secondary diffraction-related lobes, as explained in the previous section. This is consistent with the results presented in section 2.3.1 in fig. 2.9, where coherent images with $M = 700$ signal slices reach the asymptotic contrast value (which is around 15 in the given configuration).

3.1.3 Non-synchronized pump-probe and random sign compensation

In this section, the expressions for localization image contrast are obtained for non-synchronized incoherent imaging and coherent imaging with random sign compensation that are described in section 2.3.2.

a) Residual speckle without defect

Incoherent imaging

From Eq. (2.17), the expected value of pixel intensity over pairs of loading states is given by :

$$\langle I_{\text{inc}} \rangle = \langle I_p \rangle \tag{3.57}$$

Using expression Eq. (3.12) for $\langle I_p \rangle$ in Eq. (3.57) yields

$$\langle I_{\text{inc}} \rangle = 2N_r \, T_0 \, \sigma_n^2 \tag{3.58}$$

Coherent imaging

The expected value of speckle intensity in the coherent imaging case is obtained from Eq. (2.20) :

$$\langle I_{\text{coh}} \rangle = T_0 \left\langle \text{BPF}^2 \right\rangle \tag{3.59}$$

Then Eq. (2.18) yields

$$\left\langle \text{BPF}^2 \right\rangle = \sigma_{\text{bpf}_p}^2 \tag{3.60}$$

Finally, using Eq. (3.11) we obtain

$$\langle I_{\text{coh}} \rangle = 2N_r \, T_0 \, \sigma_n^2 \tag{3.61}$$

Comparison of Eqs. (3.61) and (3.58) shows that noise-related intensity is the same for coherent and incoherent imaging cases. In the absence of a defect, constructive interference does not occur, so regardless of how the intensity is calculated, statistically noise makes identical contribution to the image.

b) Defect-related spot

Incoherent imaging

Taking $\langle I_p \rangle$ from Eq. (3.19) and, finally, invoking Eq. (3.57) we obtain :

$$\langle I_{\text{inc}} \rangle = N_r^2 \, \overline{\delta}^2 \, E_0 \, \sigma_Z^2 + 2N_r T_0 \sigma_n^2 \tag{3.62}$$

Optimal coherent imaging

Introducing now Eq. (3.14) into Eq. (2.18) yields

$$\mathrm{BPF}(t) = \frac{1}{P}[N_r\overline{\delta}\, u_0(t)\, S_P + \sum_{p=1}^{P} a_p N_p(t)] \tag{3.63}$$

with $S_P = \sum_{p=1}^{P} a_p Z_p$.

As explained in section 2.3.2, the optimal situation occurs when $a_p = \alpha_p = |Z_p|/Z_p$ (see Eq. (2.24)), i.e. when this coefficient indicates the sign of differential defect strength $Z_p = f_{m_2} - f_{m_1}$.

Introducing Eq. (3.63) into Eq. (2.20) and (2.24), and taking the expected value yields :

$$\langle I_{\mathrm{opt}} \rangle = \left\langle I_{\mathrm{coh}}|_{(a_p=\alpha_p)} \right\rangle = \frac{1}{P^2} N_r^2 \overline{\delta}^2\, E_0 \left\langle S_P^2 \right\rangle + \frac{1}{P} 2 N_r T_0 \sigma_n^2 \tag{3.64}$$

with E_0 defined in Eq. (3.18).

In the optimal case, $a_p = \alpha_p$, so $S_p = \sum_{p=1}^{P} |Z_p|$ and it is easy to show that :

$$\left\langle S_P^2 \right\rangle = P\sigma_{|Z|}^2 + P^2 \mu_{|Z|}^2 \tag{3.65}$$

Therefore :

$$\langle I_{\mathrm{opt}} \rangle = N_r^2 \overline{\delta}^2\, E_0\, (\sigma_{|Z|}^2 + P\mu_{|Z|}^2) + 2 N_r T_0 \sigma_n^2 \tag{3.66}$$

To conclude, an expected value of intensity at the defect spot depends on the radiated energy E_0, defect strength ($Z = f_{m_1} - f_{m_2}$), number of considered pairs of loading states P, geometrical spreading factor, and number of receivers N_r. Since f also has a physical meaning of a scattering amplitude, which again shows the importance of defect scattering characteristics for imaging that will be studied in the next sections of this chapter.

Coherent imaging with random sign compensation

We consider here again Eq. (3.63), with the additional condition $a_p = \beta_p$ (see Eq. (2.27)), where β_p is the sign vector selected among a set of W sign vectors and maximizing the pixel intensity I_{coh} at the defect location.

Invoking Eqs. (2.27) and (2.20) yields :

$$I_{\mathrm{sel}} = \frac{1}{P} N_r^2 \overline{\delta}^2 \, E_0 \, Q_W \tag{3.67}$$

where $Q_W = S_P^2|_{(a_p=\beta_p)}$.

By definition, as explained above, Q_W is the maximum value among a set of W realizations $S_{P_w}^2 \equiv S_P^2|_{a_{pw}}$ of S_P :

$$Q_W = \max_{1 \leq w \leq W} S_{P_w}^2 \tag{3.68}$$

and the expected value of the pixel intensity at the defect location is then, from Eq. (3.67) :

$$\langle I_{\mathrm{sel}} \rangle = \frac{1}{P} N_r^2 \overline{\delta}^2 \, E_0 \, \langle Q_W \rangle \tag{3.69}$$

The cumulative distribution function F_{Q_W} of Q_W can be easily estimated, simply starting from its definition :

$$F_{Q_W}(x) = \mathrm{Prob}[Q_W \leq x] = \mathrm{Prob}\left[\bigcap_{1 \leq w \leq W} S_{P_w}^2 \leq x \right] \tag{3.70}$$

Assuming statistical independence of all events $(S_{P_w}^2 \leq x)$, this yields

$$F_{Q_W}(x) = \prod_{w=1}^{W} \mathrm{Prob}\Big[S_{P_w}^2 \leq x\Big] = \Big[F_{S_P^2}(x)\Big]^W \tag{3.71}$$

For sufficiently large values of P (typically $P > 25$ to 30), the central limit theorem implies that the statistical law of S_P is close to a normal distribution with variance $\sigma_{S_P}^2 = P\sigma_Z^2$ and zero mean. Therefore, the standard normal random variable defined as $a_p = S_P^2/\sigma_{S_P}^2$ is distributed according to the chi-squared distribution with one degree of freedom $\chi^2(1)$, whose cumulative distribution and probability density functions are denoted $F(x,1)$ and $f(x,1)$, respectively.

Consequently, Eq. (3.71) entails that the probability density function of Q_W is given by

$$f_{Q_W}(x) = \frac{dF_{Q_W}}{dx} = \frac{W}{\sigma_{S_P}^2} \, f\Big(x/\sigma_{S_P}^2, 1\Big) \; F^{W-1}\Big(x/\sigma_{S_P}^2, 1\Big) \tag{3.72}$$

Then Eq. (3.69) can be rewritten as

$$\langle I_{\mathrm{sel}} \rangle = \frac{1}{P} N_r^2 \overline{\delta}^2 \, E_0 \int_0^{+\infty} x \, f_{Q_W}(x) \, dx \tag{3.73}$$

c) Expressions of defect detection contrasts

Combining equations derived above provides theoretical expressions of the image contrasts defined in Eq. (2.21) $\mathcal{C}_{\text{inc}}$, $\mathcal{C}_{\text{opt}}$ and $\mathcal{C}_{\text{sel}}$, in the different considered versions of signal processing.

- For incoherent $\mathcal{C}_{\text{inc}}$, I_{def} is given by Eq. (3.62) and I_{av} by Eq. (3.58)
- For optimal coherent (reference) $\mathcal{C}_{\text{opt}}$, I_{def} is given by Eq. (3.66) and I_{av} by Eq. (3.61)
- For coherent with random sign compensation $\mathcal{C}_{\text{sel}}$, I_{def} is given by Eq. (3.73) and I_{av} by Eq. (3.61)

Final results are thus :

$$\mathcal{C}_{\text{inc}} = \frac{N_r \overline{\delta}^2\, E_0\, \sigma_Z^2}{2\, T_0\, \sigma_n^2} \tag{3.74}$$

$$\mathcal{C}_{\text{opt}} = \frac{N_r \overline{\delta}^2\, E_0\, (\sigma_{|Z|}^2 + P\mu_{|Z|}^2)}{2\, T_0\, \sigma_n^2} \tag{3.75}$$

$$\mathcal{C}_{\text{sel}} = \frac{N_r \overline{\delta}^2\, E_0\, \int_0^{+\infty} x\, f_{Q_W}(x)\, dx}{2P\, T_0\, \sigma_n^2} \tag{3.76}$$

From these expressions, we can also define the contrast ratios (or contrast gain) relatively to the incoherent imaging case $r_{\text{opt}} = \mathcal{C}_{\text{opt}}/\mathcal{C}_{\text{inc}}$ and $r_{\text{sel}} = \mathcal{C}_{\text{sel}}/\mathcal{C}_{\text{inc}}$ as

$$r_{\text{opt}} = \frac{\sigma_{|Z|}^2 + P\mu_{|Z|}^2}{\sigma_Z^2} \tag{3.77}$$

and

$$r_{\text{sel}} = \frac{\int_0^{+\infty} x\, f_{Q_M}(x)\, dx}{2P\, (\sigma_0 - \mu_f^2)} \tag{3.78}$$

An elementary variable substitution shows that r_{sel} is actually independent of P and σ_Z^2 and depends only on W :

$$r_{\text{sel}} = \int_0^{+\infty} x\, g_W(x)\, dx \tag{3.79}$$

with

$$g_W(x) = W f(x,1)\, F^{W-1}(x,1) \tag{3.80}$$

The expression of r_{sel} given in Eq. (3.79) can be easily estimated by numerical integration or, alternatively, quite closely approximated by :

$$r_{\text{sel}} \simeq \sqrt{\pi}\, \ln(W) \tag{3.81}$$

The corresponding curve is plotted in fig. 3.2. This curve is a result of central limit theorem application, i.e. it is only valid for sufficiently large number of loading states pairs P, when the deterministic process of defect modulation can be approximated with normally distributed scattering characteristics. In this case, coherent imaging with random sign compensation provides results better than incoherent imaging. For a given value of W, contrast and, therefore, expected contrast gain r_{sel}, depend on the defect scattering cross-section, number of receivers and, in case of passive monitoring, on number of noise sources, as it will be shown later in section 4.2.

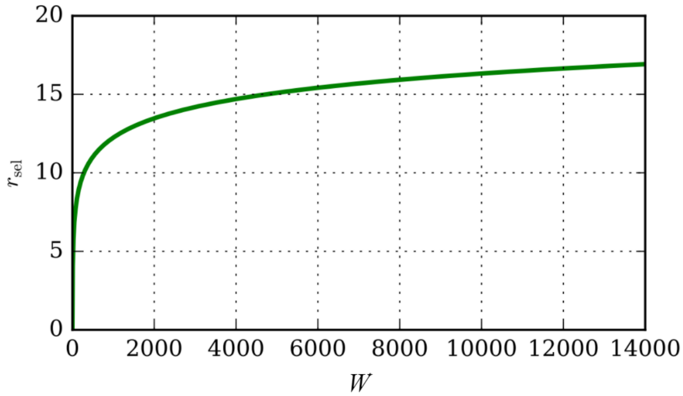

FIGURE 3.2 – Theoretical evolution of r_{sel} as a function of number of sign vectors W. Parameter r_{sel} is an expected contrast gain of coherent imaging comparing to incoherent imaging.

Hence, for instance, we can see that a random selection of a set of $W = 5000$ sign vectors is sufficient to obtain an expected contrast gain of a factor 15.

3.2 Study on image contrast and CAN scattering cross-section : static experiments

This section describes studies on contrast on different parameters. It is of interest to understand limitations of the developed algorithm and to find the optimal conditions for passive reference-free experiment.

3.2.1 Influence of angle between ruler and plate on image contrast

This section is concerned with preliminary so called static experiments. The localization algorithm here is based on a pristine reference : differential signals Δs are obtained by subtracting signals measured on a plate with defect s^w and signals measured on the same plate without defect $s^{w/o}$. The defect was the same as described before (sphere pressed against the plate). Emission signals is 1 cycle burst of $\Delta T = 100$ ms duration generated at $f = 10$ kHz (see fig. 3.3). Both s^w and $s^{w/o}$ are obtained after averaging over 20 ΔT-acquisitions. Differential signal obtained from the n^{th} receiver is defined as :

$$\Delta s_n(t) = s_n^w(t) - s_n^{w/o}(t)$$

Then back-propagation is performed similarly to the procedure described in section 2.3.1 of chapter 2 for $M = 1$ slice and localization images are obtained according to Eq. (2.17). Weber contrast denoted by $\mathcal{C}$ is calculated from Eq. (2.21) with averaged intensity over all x and y defined as

$$I_{av} = \frac{1}{N_{pixel}} \sum_{(x,y)} I(x,y) \tag{3.82}$$

where $I(x,y)$ is given by Eq. (2.16), N_{pixel} stands for the number of considered candidate defect positions.

One of the parameters that might influence localization image contrast and is, therefore, of interest to study is defect strength. In the current experimental setup it can be regulated by manual turning of a micrometer screw (see fig. 3.4) in the defect attaching mechanism. It changes the angle between ruler and plate, which in turns means a local change in stress at CAN (sphere-plate contact).

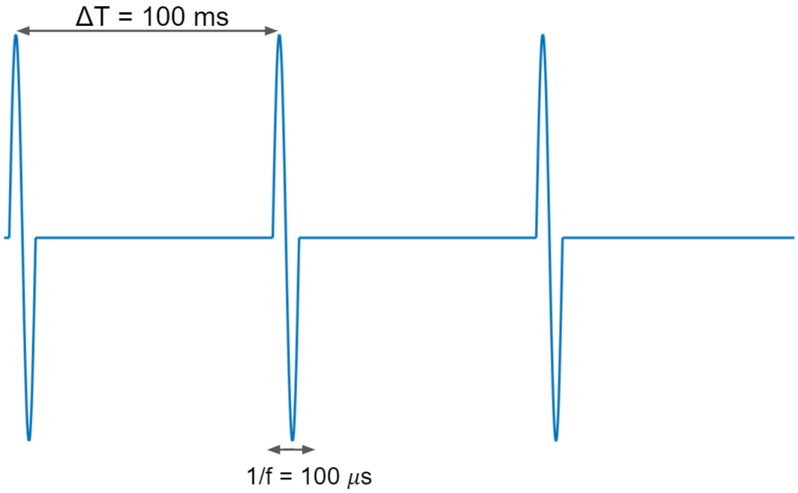

FIGURE 3.3 – Emission signal in static experiments : a sequence of 100 ms one-cycle sine bursts at 10 kHz.

This mechanism is rather subtle, so the important fact to check was a reproducibility of experiments. To do so, measurements of image contrast are performed at different angles, some of the angles are repeated several times in a way that such sequence of static experiments imitates an excitation by a one period sine wave. First, we do a static experiment at a particular angle (acquisition 0), then we turn screw clockwise (fig. 3.5 a) by 6° or 1 μm between two ticks on a screw scale and conduct another static experiment (acquisition 1), we repeat it 5 times (acquisitions 1-5), after that we turn screw counterclockwise (fig. 3.5 b) by 1 μm 10 times while doing another series of static experiments (acquisitions 6-15), finally, again turn screw clockwise (fig. 3.5 a) 5 times and conduct the last series of experiments (acquisitions 16-20) and at the end come back to the initial angle (acquisition 20 is equivalent to an acquisition 0, as well as an acquisition 10). A scheme of this experimental sequence is illustrated in fig. 3.5 c : these are ticks on the screw micrometer scale (as in fig. 3.4) where numbers correspond to the order of experimental acquisitions. So acquisitions 0, 10 and 20 are preformed with the same micrometric screw angle, which means the contrast values are expected to be similar but as observed in fig. 3.6, they are not. The same for pairs of acquisitions 1 and 9, 2 and 8, etc. Overall, the dependency is expected to be periodic but it is not. The observed effect is hysteresis related to presence of friction in the sphere-plate contact. This means that angle on a

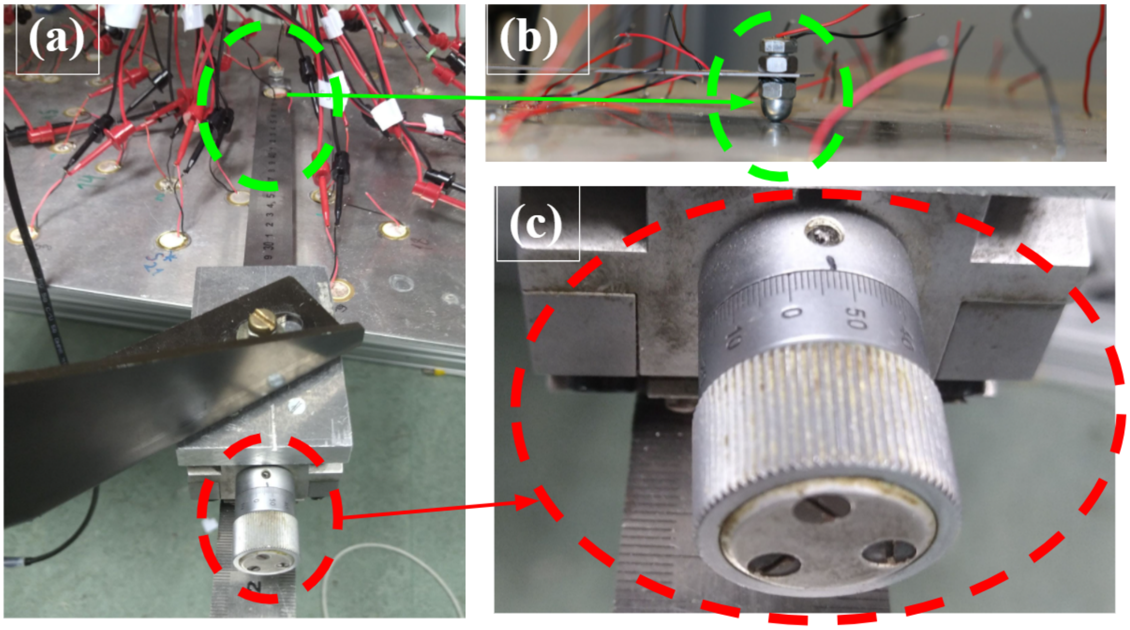

FIGURE 3.4 – Micrometer screw in the defect attaching mechanism allowing to change the angle between the ruler and the plate. (a) - Defect attaching mechanism, (b) - Zoom on the defect, (c) - Zoom on the micrometer screw.

micrometer is not firmly related to particular contact conditions. Thus, experiments with a specific angle are not reproducible.

Then we assumed that the problem of reproducibility can be solved by enhancing a poor sphere-plate contact, thus, we added in the next experiments, first, water and then oil in order to improve coupling. However, as you can see in fig. 3.7 and fig. 3.8 contrast values at acquisitions 0, 10 and 20 are not similar, which means even with enhanced sphere-plate contact there is no reproducibility of experiments with different angles. Increasing of the angle affects image contrast non-monotonously, therefore, micrometric screw is not a proper parameter to control image contrast.

As is obvious from theoretical derivations presented in section 3.1.1, the defect parameter influencing the detection contrast is the scattering cross-section. The non-reproducible results observed in the present section then tend to show that, due to complex and not well-calibrated contact phenomena, no bijective relationship can be deduced between the micrometric angle and the contrast and, hence, scattering cross-

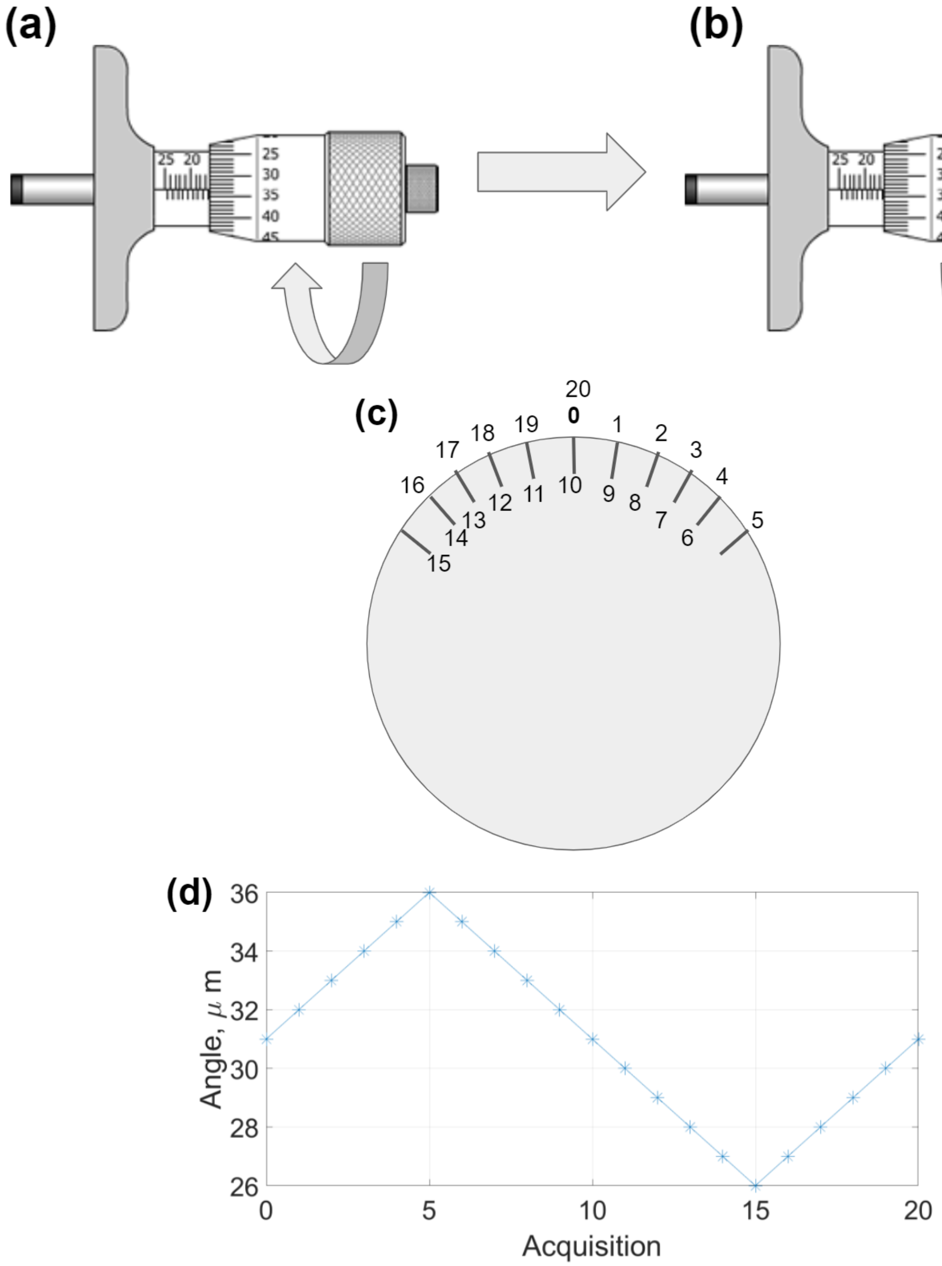

FIGURE 3.5 – Scheme of the experiment with hysteresis : (a) - Turn of a micrometric screw clockwise, (b) - Turn of a micrometric screw counterclockwise, (c) - Schematically shown order of acquisitions (0-20) on the micrometric screw with the distance between two ticks equal 1 μm, (d) - Readings on the micrometric screw at different ruler-plate angles as a function of acquisitions.

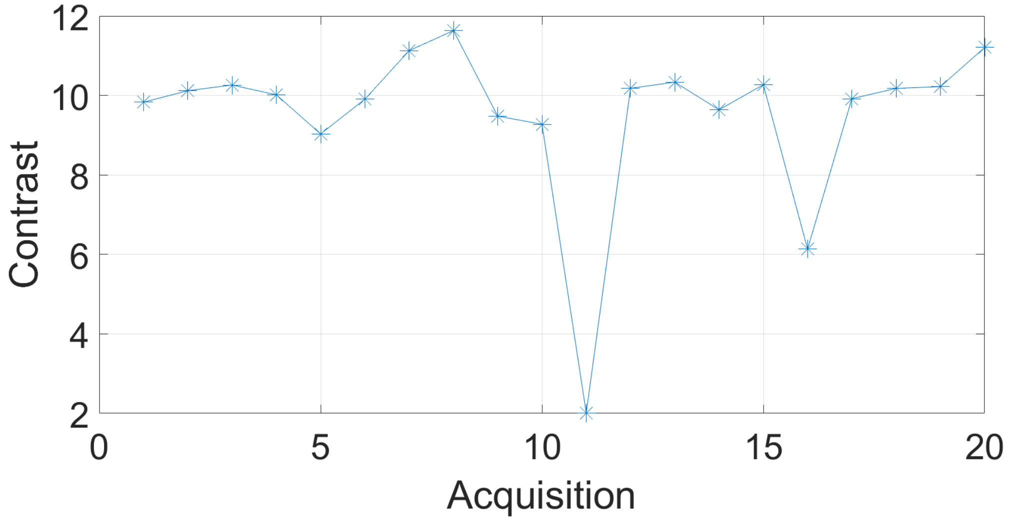

FIGURE 3.6 – Image contrast versus acquisition at different micrometric screw angles (see fig. 3.5).

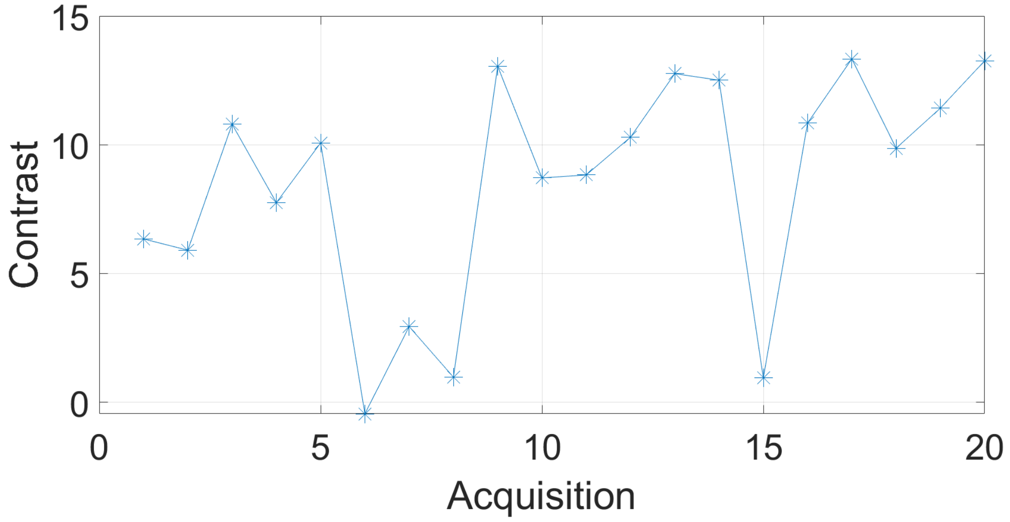

FIGURE 3.7 – Image contrast versus acquisition at different micrometric screw angle. Sphere-plate contact is water-soaked.

section in our experiment. This will be verified in the next section, where the defect scattering cross-section will be directly estimated for different angles. Then, it will be

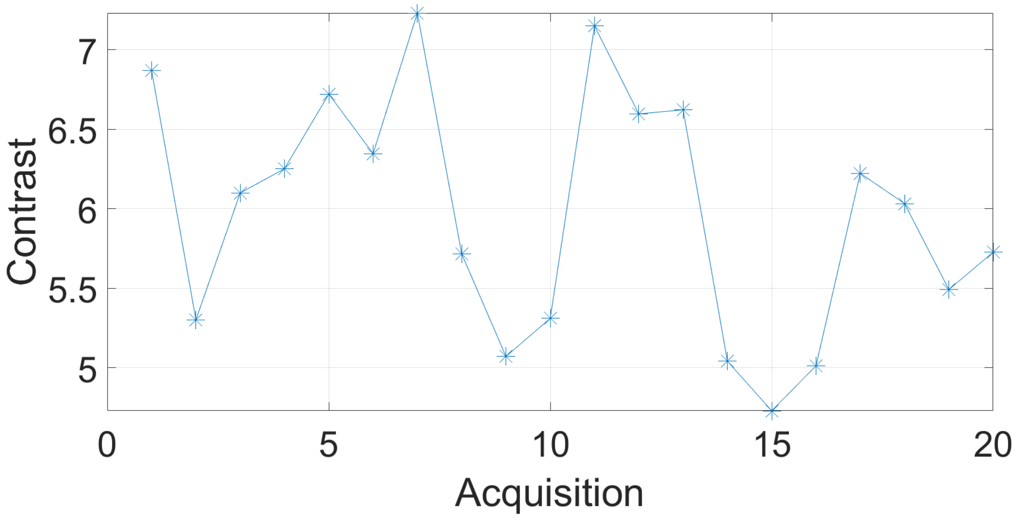

FIGURE 3.8 – Image contrast versus acquisition at different micrometric screw angle. Sphere-plate contact is impregnated with olive oil.

confirmed that the scattering cross-section is the pertinent defect-related parameter and theoretical contrast-scattering cross-section relationships from section 3.1.1 will be validated.

3.2.2 Contrast and CAN scattering cross-section relationship in static experiments

As discussed before in chapter 1, scattering cross-section represents the rate of interaction between sound wave and a scatterer (defect). If a value of scattering cross-section is sufficiently high, the defect is detectable. To evaluate the defect's scattering cross-section, experimental approach based on statistical properties of scattered flexural waves is applied [87].

First, active static measurements are conducted with defect s^w and without defect $s^{w/o}$: twenty sine bursts are excited at $f = 10$ kHz with $\Delta T = 0.05$ s between pulses. Then these signals are filtered in a frequency band of [9-11] kHz. Narrow band filtering allows to consider that scattering cross-section is a constant in this frequency range. Also signals are averaged over number of pulses to increase signal-to-noise ratio. After that envelope of an averaged signal is extracted : $env(s^{w/o})$.

Then the two-steps fitting procedure described in section 1.4 of chapter 1 is applied in order to experimentally estimate the defect scattering cross-section denoted by σ.

The next step is to establish relationship between image contrast and scattering cross-section. To do so, series of 72 active static experiments with different screw angles has been conducted. In this experiments, signals obtained at the angle 60 were considered as a reference $s^{w/o}$. The results are demonstrated in fig. 3.9 : as expected, contrast is increasing monotonously with an increase in the defect's scattering cross-section. It is important to note that scattering cross-section in static experiments is in mm range.

Fig. 3.9 illustrates dependency of an image contrast on a defect scattering cross-section from the experimental measurements. This curve matches the one obtained in simulations in fig. 3.1 and the theoretical linear curve for low σ. For higher σ, the curve experiences saturation related to diffraction side lobes from sensor network, as explained before in section 3.1.1.

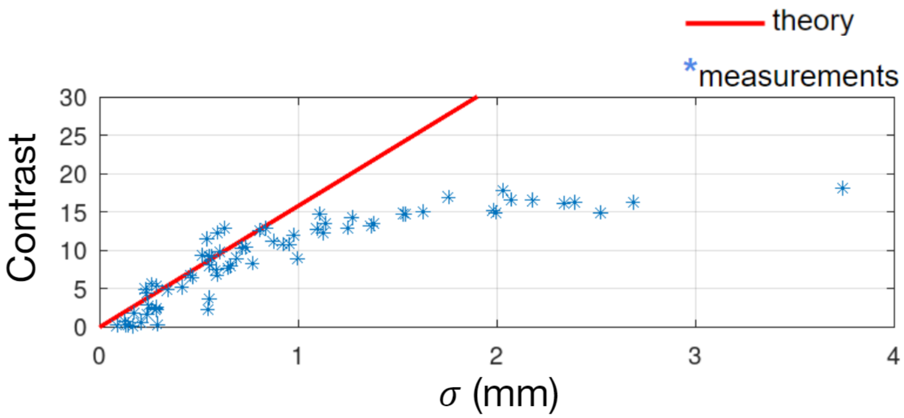

FIGURE 3.9 – Image contrast versus defect scattering cross-section for active static experiment : experimental measurements.

3.3 Measurement of CAN scattering cross-section for dynamic experiments

3.3.1 Dynamic experiments : measurement of scattering cross-section

Dynamic non-synchronized pump-probe experiments were conducted at $f_{pump} = 1$ Hz. The probe wave is a sequence of $M = 800$ one-cycle sine bursts at $f_{probe} = 10$ kHz of duration $\Delta T = 0.05$ s each.

At first, we tried to measure scattering cross-section by processing the recorded signals as a series of static experiments (see section 3.2.1). The received signals are qualitatively similar to the one shown in fig. 2.2. These signals are cut into M slices. Mean over slices plays the role of a reference $s^{w/o}$. For each ΔT-slice and mean over slices $s^{w/o}$ scattering cross-section is measured by following the differential signal envelope fitting procedure described in the section 1.4 for active static experiment. Every ΔT-slice separately is considered static.

Static measurements are based on linear superposition, so this procedure could be questioned when nonlinearity is involved. However, as it was shown in section 2.2, CAN is activated mostly by powerful pump (causes three orders of magnitude higher strain), so the probe propagation can be considered mostly linear, especially, after filtering out low frequencies, we get linear signals and linear imaging based on superposition.

However, this measurement technique appeared to be rather challenging, since squares of envelopes of differential signals do not attenuate exponentially being hidden by high level of noise (see fig. 3.10a). Thus, fitting is not possible. The reason for that is absence of signals averaging that would reduce the electronic noise level. Contrary to the static case, where the signals s^{w} and $s^{w/o}$ are averaged over 20 repetitive acquisitions, here it is not possible to do within one ΔT slice corresponding to one contact state.

To increase signal-to-noise ratio, signals have been averaged in a different way, namely, over number of pump periods. In fig. 3.11 the averaging process is explained. By calculating mean value of acquisitions made at instants denoted by circles, we obtain averaged signal 1 at the beginning of pump period. Similarly, mean value of acquisitions at instants denoted by triangles give us signal 2. Averaging of rhombuses forms signal 20 at the end of pump period. As a results we have 20 pulses-acquisitions

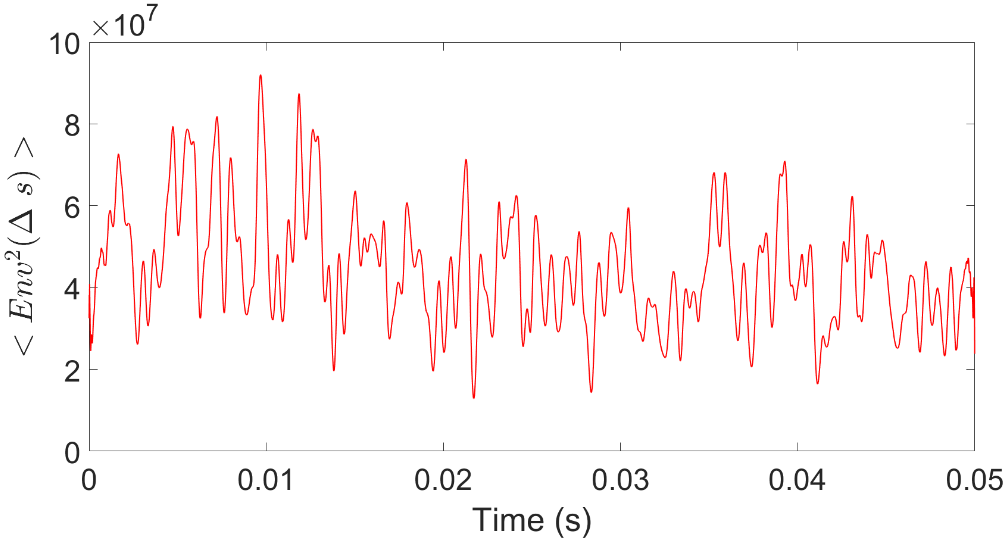

(a) Squared envelope of differential signal against time. Dynamic scattering cross-section measurement without averaging over periods.

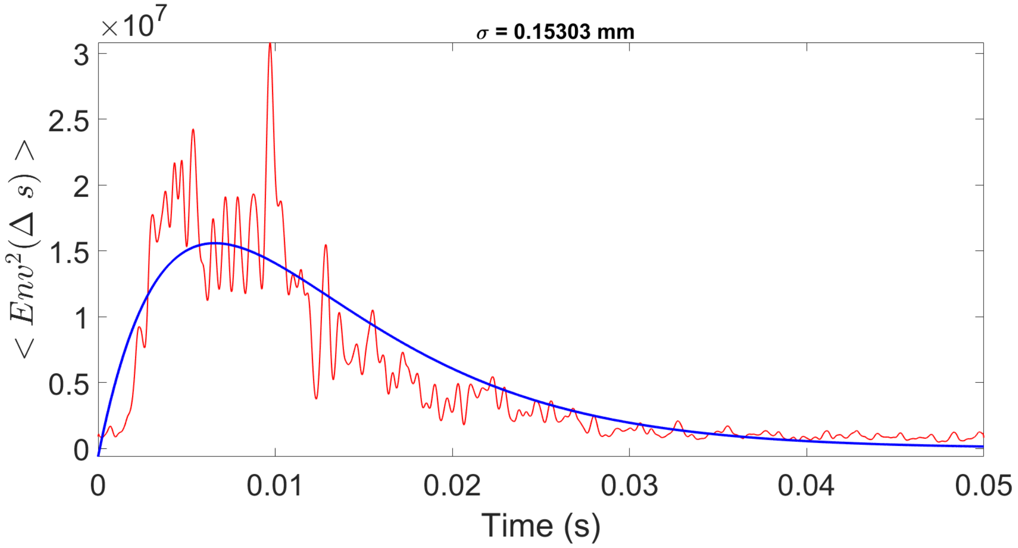

(b) Dynamic scattering cross-section measurement with averaging over periods (typical fitting).

Figure 3.10 – Dynamic scattering cross-section measurements by fitting averaged over receivers envelope of differential signal : challenge and solution.

with a total duration of one pump period.

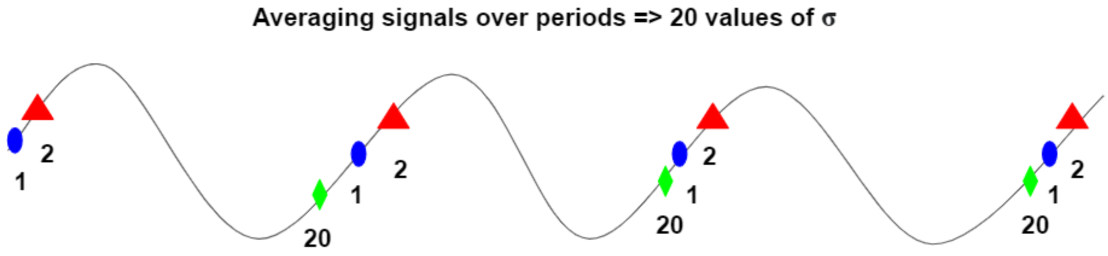

FIGURE 3.11 – Averaging signals over periods for scattering cross-section measurement in pump-probe experiments.

After averaging, fitting for the squared envelope of differential signals becomes possible (see fig. 3.10b), therefore scattering cross-section can be estimated for each acquisition.

In fig. 3.12a scattering cross-section is shown as a function of acquisition, i.e. time within one pump period. It is interesting to note that order of magnitude for apparent scattering cross-section in dynamic experiment is about 16 times lower than in static counterpart : maximum scattering cross-section is around 0.19 mm, whereas for static it was 3 mm. However, this value is higher than the detection threshold $\sigma_{th} = 0.065\ mm$, which shows that the proposed localization algorithm is reliable for active dynamic experiments.

As for contrast, we computed an image using back-propagation procedure at every acquisition instant (20 images) for the signals averaged over periods. In fig. 3.12b there are results of a study on contrast as a function of acquisition, in other words, time during one pump period after averaging. Both scattering cross-section (fig. 3.12a) and contrast (fig. 3.12b) general periodic behavior is observed as expected. However, there is a small synchronization issue between scattering cross-section and contrast : minimum of contrast is at acquisition 10, whereas for σ it is at acquisition 8. The reason why the contrast and σ are a little out of sync for a single pump-probe experiment is the subject for the future works.

In fig. 3.12b three variants of Weber contrast were computed. In the first definition of contrast (circles) in Eq. (2.21), intensity I_{def} at the actual defect position in nominator is considered. In the second definition (asterisks), maximum intensity in a square 2×2 cm around the defect is put into nominator of Eq. (2.21). In the third definition (crosses), maximum intensity in the entire plate is considered in a

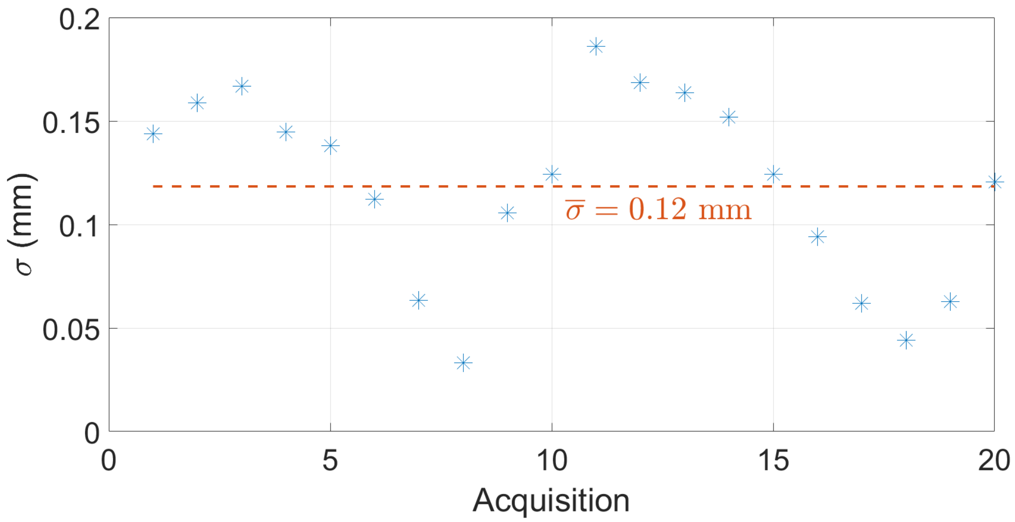

(a) Scattering cross-section versus number of acquisitions in pump-probe experiment.

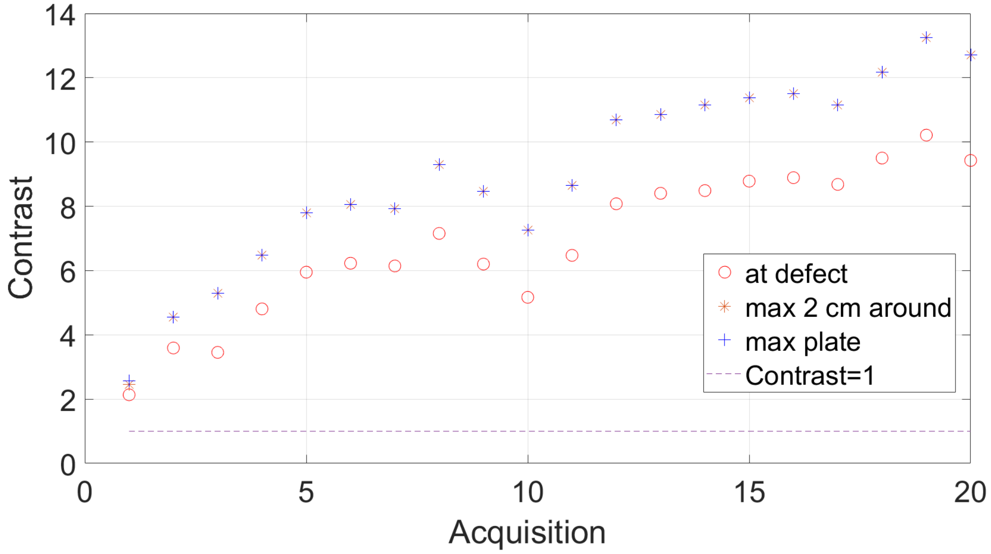

(b) Comparison between different definitions of contrast versus number of acquisitions in pump-probe experiment.

FIGURE 3.12 – Scattering cross-section (a) and contrast (b) as functions of acquisitions within one period of pump wave in active dynamic experiment with averaging over periods.

nominator of Eq. (2.21). All three curves follow similar trend of a periodic function in terms of phase with modulated amplitude. Values for contrast of the second definition are higher than for the first one, because sometimes defect is moving a little to the side and there is imprecision of the localization algorithm of 1 cm. Values of the second and third definition coincide, so further in this work we use contrast of the second definition to take this imprecision into account.

3.3.2 Comparison of different dynamic experiments to each other in terms of contrast and scattering cross-section

It is of interest to compare scattering cross-section in different dynamic experiment to find conditions for maximum of σ and image contrast, so we can reproduce them while making passive dynamic tests.

However, scattering cross-section varies during one experiment (see fig. 3.12a). For this matter, it was decided to take a mean value over 20 scattering cross-section values during one period : $\overline{\sigma}$ represents one dynamic experiment.

First, the series of experiments with different pump amplitudes was conducted. According to fig. 3.13, $\overline{\sigma}$ grows monotonously with increase in pump amplitude and reaches its maximum at $A_{pump} = 4.5$V.

The « incoherent » contrast is introduced for this series of experiments. By definition, it is a contrast of the mean of images corresponding to 20 different acquisitions within one pump period for the signals averaged over periods. Fig. 3.14 illustrates the « incoherent » contrast as a function of scattering cross-section in pump-probe experiments with different pump amplitudes. The contrast grows with increase in scattering cross-section, which in turn grows with increase in pump amplitude. This means that a pump amplitude is a good parameter to control quality of localization images.

To summarize, pump amplitude is an appropriate parameter for scattering cross-section contrast control and therefore improving image contrast.

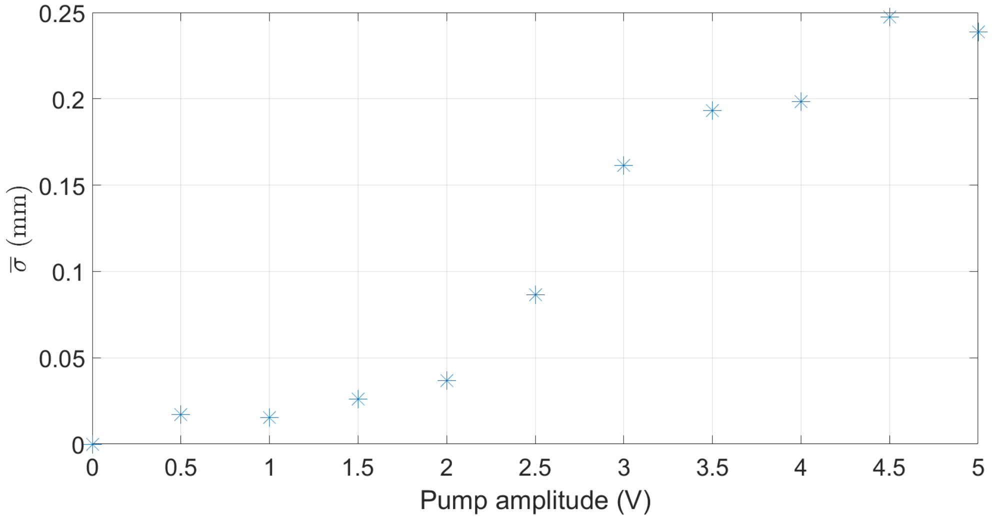

FIGURE 3.13 – Scattering cross-section against pump amplitude in active dynamic experiment.

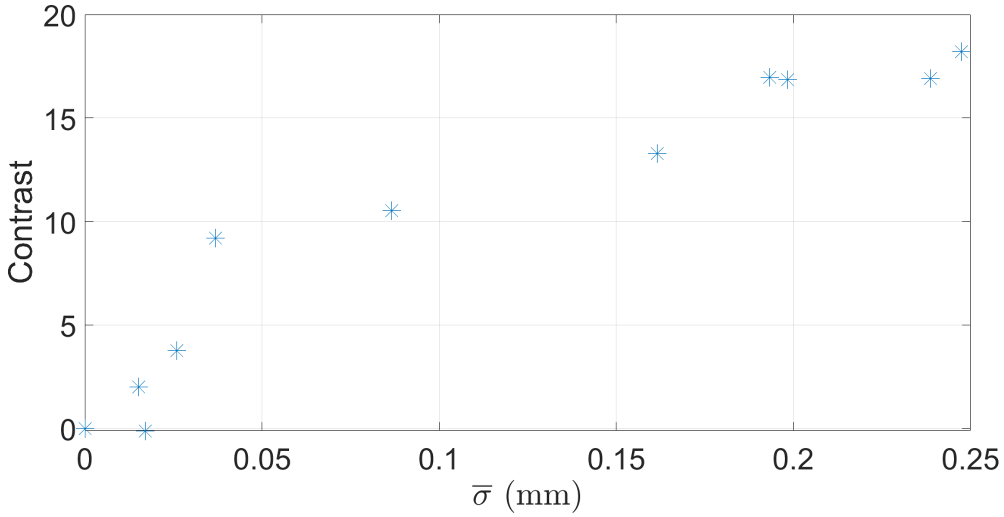

FIGURE 3.14 – Contrast against mean scattering cross-section in active dynamic experiments with different pump amplitudes.

Conclusions

It has been shown here that image contrast depends monotonically on the defect scattering cross-section, and is directly proportional to it for small scattering cross-sections. This statement has been confirmed by experimental measurements, numerical simulation of scattering in infinite plate and theoretical derivation for active static experiments. In dynamic experiments, scattering cross-section values are much smaller than in static case, yet it is sufficient to get a satisfactory detection. CAN with scattering cross-section from the order of hundredths of a millimeter to several millimeters can be resolved by the proposed localization algorithm. The estimated detection threshold in terms of scattering cross-section is 0.065 mm for the considered experimental setup. The detection is possible at such small scattering cross-section values, since dynamic contrast is M times higher than the static one, where M is number of the considered loading states.

In pump-probe experiment, image contrast can be improved by increasing pump amplitude or changing the defect strength, i.e. angle between ruler and the plate. However, this angle is not firmly related to particular contact conditions. Thus, experiments with a specific contact state are not reproducible due to hysteresis of the contact with friction. Also image contrast is proportional to number of receivers and signal-to-noise ratio in both static (with and without defect) and dynamic experiments according to the obtained theoretical formula.

In the next chapter, we will discuss the application of the developed method to the passive baseline-free case. We will see that initial configuration of sensors array considered for active experiments is not sufficient to obtain satisfactory defect detection in passive case and we will propose an improved configuration.

Chapter 4

Passive baseline-free dynamic experiments for damage localization : proof of concept

Contents

Introduction

This chapter is concerned with experimental development of a passive reference-free localization algorithm of CAN in thin plates. In this chapter, passive probe signal is white noise emitted simultaneously by a set of PZT transducers.

The defect detection method is based on estimation of Green's function derived from analysis of differential noise correlations for short samples of signals induced by low frequency pumping. Localization is provided with back-propagation technique described in a greater detail in [68, 70, 89] adapted for pump-probe experiment similar to the way it is described in the chapter 2 for active case.

The improved parameters for the pump-probe experiment enabling defect detection in passive mode are found thanks to quantitative analysis of image contrast and defect scattering cross-section relationship derived in chapter 3.

4.1 Preliminary pump-probe passive experiments

This section describes preliminary passive pump-probe experiments and the control parameters allowing to increase image contrast.

4.1.1 Experiment with a set of controlled simultaneously emitting white noise sources

In this section, the pump-probe experiments are similar to the ones described in chapter 2 : the same aluminum plate with a CAN in a form of 1 cm steel sphere pressed against the plate is excited by the same harmonic continuous pump wave of $f_{pump} = 1$ Hz. High frequency white noise plays the role of a probe signal. The signal resulting from pump wave and high frequency noise is recorded by the set of PZT patches glued on the top surface of the plate.

To retrieve Green's function from noise correlation, we need homogeneously distributed acoustic diffuse field with wide band of frequencies. For this purpose, we use a set of $N_s = 14$ PZT sources of the same kind as $N_r = 14$ receivers distributed on the top surface of the plate. They emit uncorrelated Gaussian white noise simultaneously of 40 s duration. Both emission and reception are operated with a multichannel digital sampling board (24 I/O MOTU, 96 kS/s, 24 bits digitizer). The shaker firmly attached to the plate emits a continuous sine wave at $f_{pump} = 1$ Hz (see fig. 4.1).

Noise spectral range for emission is between 1 and 30 kHz which corresponds to the range of high frequency recordings in successful active experiments shown in chapter 2. The idea is to keep the same frequency range, as it was for signals in active experiments.

For every recording, low-pass filtering is applied to retrieve the LF pump vibration $s_{pump}(t)$. As for the high frequency signal, band-pass filtering between 1 and 30 kHz is applied, followed by a whitening procedure consisting in temporal and spectral normalization [102]. This procedure is aimed at improving Green's function

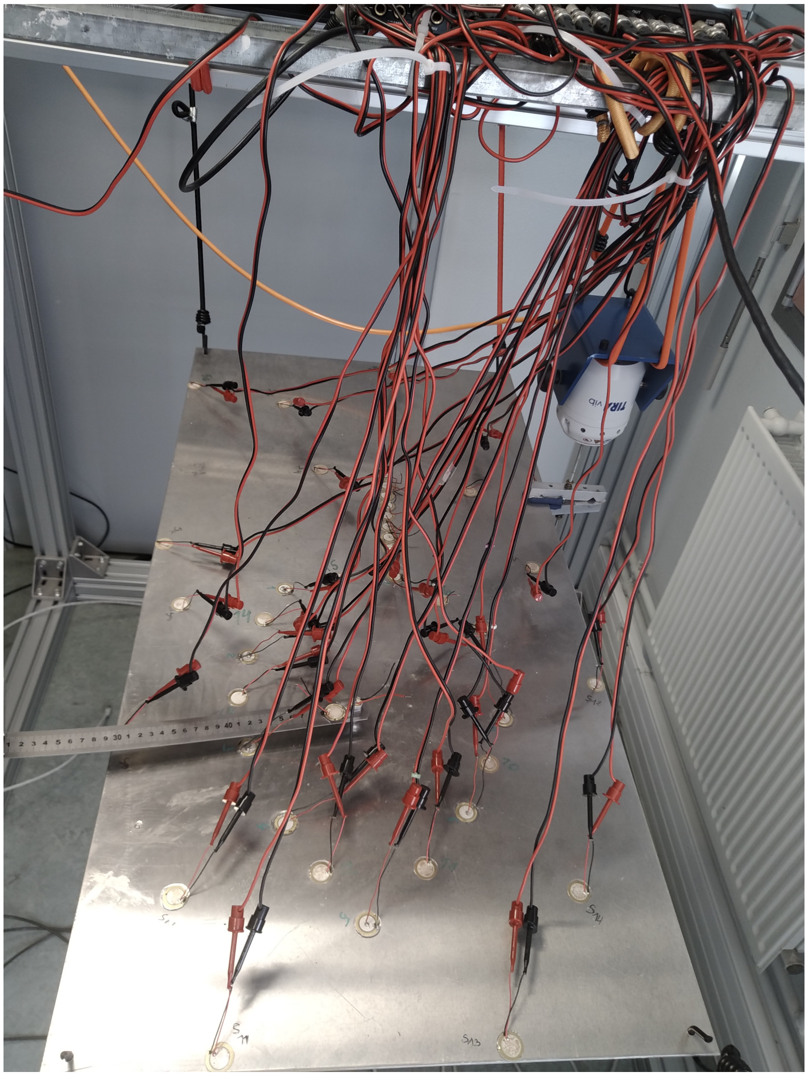

FIGURE 4.1 – Passive experimental setup with multiple simultaneous noise sources.

quality by making noise spectrum more flat. Whitening starts with temporal normalization, which is necessary to correct time fluctuations of raw signals from signals with constant amplitude :

$$s_{norm}(t) = \frac{s(t)}{\sqrt{env(s^2(t))}}$$

Here « *env*() » stands for signal envelope extracted using the method that consists in Squaring and Low-pass Filtering the input raw data. The raw input signal is squared and then passes through a low-pass filter. Squaring the signal effectively demodulates the input. Indeed, the input plays the role of a carrier wave for its squared version. This means that half the energy of the signal is pushed up to higher frequencies and half is shifted down toward low frequencies. Low-pass filtering eliminates the high frequency energy resulting in the low-frequency envelope. Finally, to maintain the correct scale, we perform two additional operations : we multiply the signal by a factor of two, since we are keeping only the lower half of the signal energy, and we take the square root of the signal (see fig. 4.2).

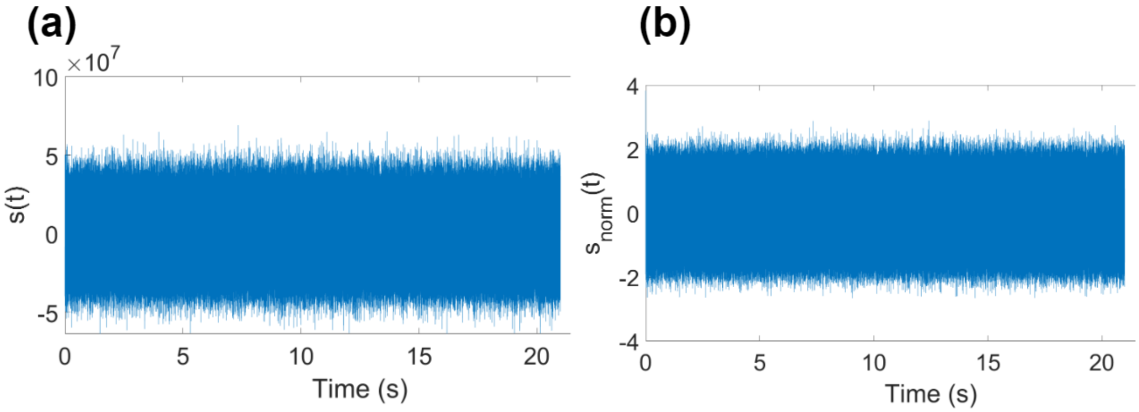

FIGURE 4.2 – Recorded signal : (a) before and (b) after the normalization in time.

After that, normalization is carried out in frequency domain with a Fourier transform of s_{norm} :

$$s_{white}(\omega) = \frac{s_{norm}(\omega)}{\sqrt{env(2|s_{norm}(\omega)|^2)}}$$

A factor 2 is introduced to take into account both positive and negative frequencies. An inverse Fourier transform of $s_{white}(\omega)$ completes the whitening procedure. In the following description we will omit subscript « white » for convenience. The spectrum of signals before and after whitening procedure is presented in fig. 4.3. After whitening, the spectral flatness increases making a signal closer to white noise.

To apply similar to the chapter 2 differential procedure, signals at different loading states are required. To get them, whitened signal received at the n^{th} sensor is cut into M short slices of duration $\Delta T \ll 1/f_{pump}$ smoothed with Hanning window.

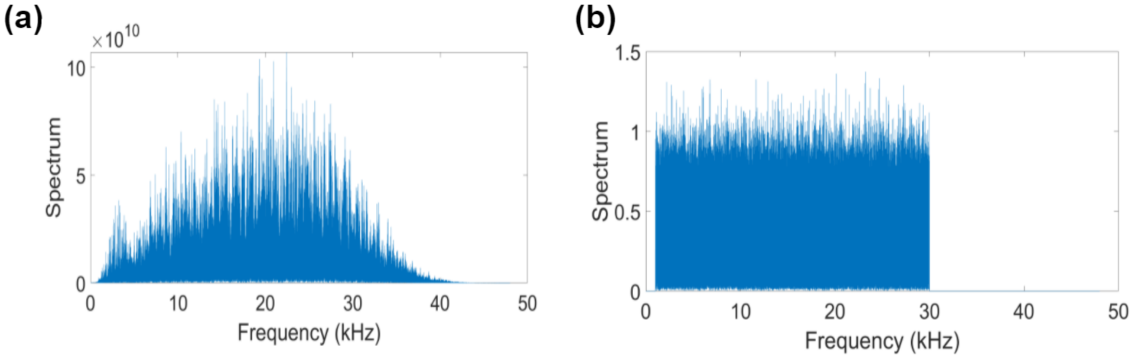

FIGURE 4.3 – Spectrum of the received signals : (a) before and (b) after the whitening procedure.

Each slice represents a particular contact loading state. Let us denote $s_{n,m}(t)$ the m^{th} slice of a signal recorded by the receiver R$_n$. Instead of actual emitter in active experiments, one of the receivers R$_{VE}$ plays the role of a virtual emitter : in practice, it remains a receiver, but in theory, for Green's function reconstruction we can consider it as the "reference sensor", the recording from which is being cross-correlated with all the other receivers in the array. Then for the m^{th} slice and receiver R$_n$, cross-correlation $C_{n,m}$ between signal recorded by this receiver $s_{n,m}$ and signal recorded by virtual emitter $s_{VE,m}$ is computed in frequency domain according to Eq. (1.10) and convolution theorem as :

$$C_{n,m}(\omega) = s_{VE,m}(\omega)s^*_{n,m}(\omega) \tag{4.1}$$

As a result for each slice, N_r correlations are obtained. After that, an inverse Fourier transform is applied to each correlation. Examples of cross-correlations as functions of time for a 10 ms window duration are shown in fig. 4.4. Quality of the retrieved Green's function depends on these curves symmetry extent with respect to $t = 0$ [64]. After whitening procedure, cross-correlation becomes more symmetric with respect to y-axis in fig. 4.4 b, therefore Green's function quality is improved.

Differential correlations for the m^{th} slice and n^{th} receiver are defined as follows

$$\Delta C_{n,m}(t) = C_{n,m}(t) - \frac{1}{M}\sum_{m=1}^{M} C_{n,m}(t)\,. \tag{4.2}$$

Then back-propagation procedure is applied to this differential correlation.

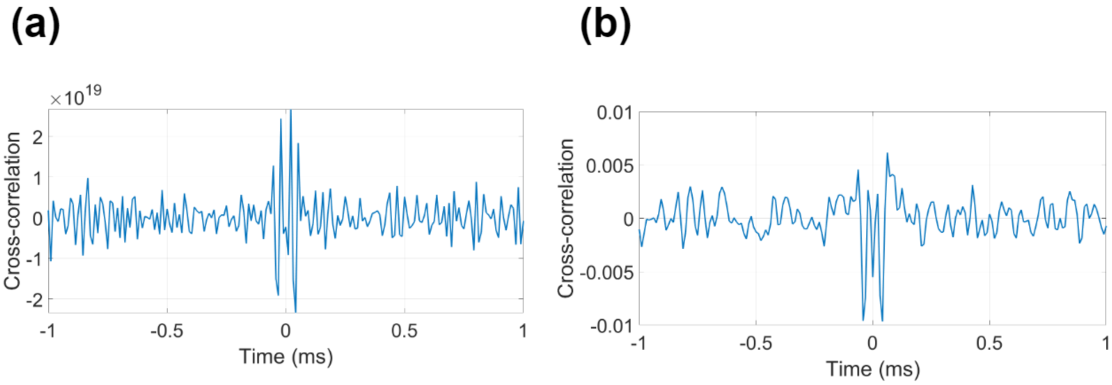

FIGURE 4.4 – Example of cross-correlation function between signals recorded by receivers R_1 and R_{14} (a) without and (b) with whitening procedure. Cross-correlation of whitened signals are more symmetric with respect to y-axis, that implies improved quality of Green's function reconstruction.

Similarly to eq. (2.14) phase function is given by :

$$F_{n,m}(x,y,\omega) = \Delta C_{n,m}(\omega)\, e^{j\, k(\omega)\, r_{n,VE}(x,y)}\,, \tag{4.3}$$

where $r_{n,VE}(x,y)$ is the sum of distances from receiver R_n and virtual emitter R_{VE} to pixel (x,y), $k(\omega)$ is the wavenumber fulfilling dispersion relationship for $A0$ mode (Eq. (1.2)). Then a back-propagation function for the m^{th} slice is given by Eq. (2.15).

After returning to the time domain, coherent imaging with synchronous detection (as in section 2.3.1) is carried out by using Eq. (2.18) for coherent summation of back-propagation functions multiplied by pump amplitude ponderation coefficients (Eq. (2.19)) and computing pixel intensity for imaging (Eq. (2.20)).

The localization result presented in fig. 4.5 is not satisfactory as the defect is not localized. To understand the reasons of such a low image contrast, the current experimental parameters are briefly analyzed below and ways of improvement are proposed.

4.1.2 Results and discussion

The localization result presented in fig. 4.5 is unsatisfactory. This might occur due to poor quality of the Green's function reconstruction from correlation of diffuse

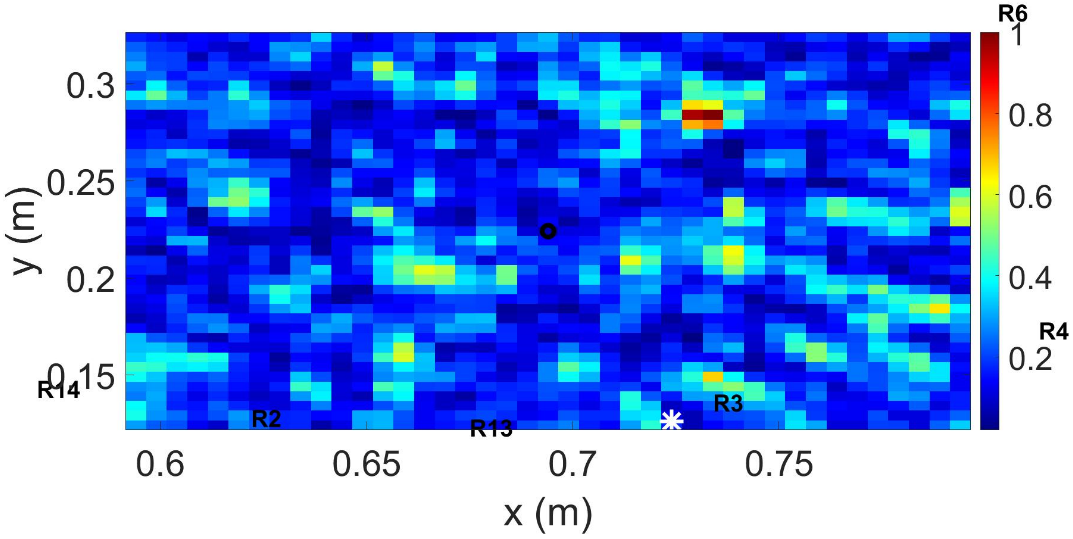

Figure 4.5 – Localization result for passive pump-probe experiment $N_s = 14$ simultaneously emitting uncorrelated noise sources. $N_r = 14$. Unsuccessful detection.

waves. Accuracy of the Green's function reconstruction is discussed in [103], where the statistical model based on relative noise level (RNL) estimation is developed.

For receivers R_i and R_j cross-correlation of the recorded reverberated signals can be expressed as

$$C_{ij} = D_{ij} + n_{ij} \, , \tag{4.4}$$

where D_{ij} represents a deterministic term containing causal and anticausal parts of the Green's function between the two receiver locations and n_{ij} is a residual noise term or Green's function reconstruction error. The ratio of energy between the reconstruction error and the deterministic part is called relative noise level and defined as

$$RNL = \frac{\int n_{ij}^2(t)dt}{\int D_{ij}^2(t)dt} \, . \tag{4.5}$$

RNL estimation might help us answer the question whether it is hypothetically possible to localize a defect with a given scattering cross-section under given experimental conditions (plate geometry and number of noise sources) using back-propagation algorithm.

It is shown that for the reverberated signals in plates RNL can be expressed as follows [103] :

$$RNL = \frac{1}{N_s}(\alpha - 1 + \frac{2\pi\eta_0}{\tau})\,, \tag{4.6}$$

where N_s is number of noise sources, τ is attenuation time related to exponential decay of reverberated signals, α is a plate shape factor ($\alpha = \frac{9}{4}$ for a rectangular plate [104]), η_0 is the modal density which is equal to :

$$\eta_0 = \frac{S}{4\pi}\sqrt{\frac{2\rho d}{D}}\,,$$

where S is a plate area, d is a plate half-thickness, D is a flexural stiffness given by Eq. (1.7).

In fig. 4.6 there is a graph of relative noise level estimated for series of experiments with different number of noise sources based on Eq. (4.6) and with the following parameters $S = 0.5\ m^2$, $\rho = 2700\ kg/m^3$, $2d = 3\ mm$, $\nu = 0.35$, $E = 69\ GPa$, $\tau \approx 10\ ms$.

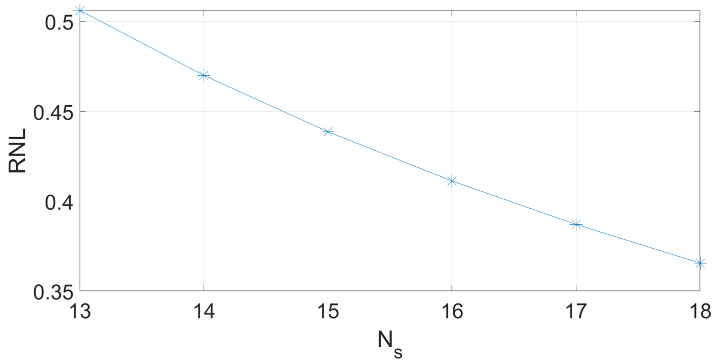

FIGURE 4.6 – Dependency of relative noise level on number of noise sources.

The synchronous detection principle described (and applied to the active case) in section 2.3.1 is applied here for the correlation functions C_{ij}. Therefore the principle of theoretical contrast derivation is similar to Sec. 3.1.2, except for a subtlety associated to the stationarity of noise sources locations.

Indeed, $n_{i,j}$ in Eq. (4.4) is not an actual noise, but a (deterministic) reconstruction error related to the number (and location) of the noise sources, as explained in [103]. For different receivers, these reconstruction noises can be assumed independent and thus Eq. (3.35) holds. However, the back-propagation of them associated to summation over receivers (bpf_m from Eq. (2.15)), will not result in independent terms for different defect states m, since noise sources are the same for all states.

Therefore, here coherent summation over m will not divide noise variance by M as in Eq. (3.41) and instead residual speckle intensity will be similar to the incoherent case :

$$\langle I \rangle = N_r \, T_0 \, \sigma_n^2 \,, \tag{4.7}$$

where σ_n^2 corresponds to the numerator of Eq. (4.5).

Consistently, the defect-related spot will be given as a modified version of Eq. (3.54) :

$$\langle I \rangle = \frac{N_r^2 \, \bar{\delta}^2 \, E_0 \, \bar{\sigma}_0}{4\pi} + N_r \, T_0 \, \sigma_n^2 \,, \tag{4.8}$$

where E_0 corresponds to $\int D_{ij}^2(t)dt$ (denominator of Eq. (4.5)).

From Eqs. (4.7) and (4.8), the corresponding contrast expression is thus

$$C = \gamma \chi' \bar{\sigma}_0 \tag{4.9}$$

with γ given by Eq. (3.26), and χ' corresponding here to the signal-to-noise ratio associated to the passive Green's function reconstruction, which is quantified by the inverse of RNL.

Considering the same experimental parameters as for fig. 4.6 the RNL estimated from Eq. (4.6) for $N_s = 14$ is around 0.47.

Direct application of Eq. (4.9) with $\bar{\sigma} \approx 0.2$ mm and $N_r = 14$ would yield a contrast value of around 0.02, which could explain the non-detection observed in fig. 4.5.

Actually things are slightly more complex than that because in the presence of a defect, the Green's function reconstruction error not only depends on the plate properties, but also on the defect features.

Formally, this reconstruction error when the defect is in a given state m can be written as

$$n_{ij,m} = n_{ij,0} + \delta n_{ij,m} \,, \tag{4.10}$$

where $n_{ij,0}$ is the Green's function reconstruction noise when the defect is in the state taken as reference (average over a pump period here).

Then we can define the RNL related to the modulation of the defect by the pump as

$$\delta RNL = \left\langle \frac{\int \delta n_{ij,m}^2(t)dt}{\int D_{ij}^2(t)dt} \right\rangle \tag{4.11}$$

and then $\chi' = 1/\delta RNL$ in the contrast expression Eq. (4.9).

Estimation of δRNL is not straightforward and will require further theoretical work in perspective. However, noticing that χ' is homogeneous to inverse of RNL, and that RNL is itself homogeneous to inverse of the number of sources N_s (from Eq. (4.6), it seems reasonable to assume proportionality between χ' and N_s.

To conclude, in the current passive reference-free experiment defect is not detected using Green's function reconstruction. Nevertheless, based on Eq. (4.9), we can increase the image contrast by :

— Increasing χ' (decreasing RNL and δRNL) by augmenting number of noise sources N_s (up to 18 in our case).

— Increasing γ by augmenting number of receivers N_r (up to 19 in our case) which γ is proportional to.

— Increasing the defect scattering cross-section $\bar{\sigma_0}$ by exciting the plate with higher pump amplitude as discussed in section 3.3.2.

In the next section, optimization of experimental parameters based on the reasoning discussed here and on quantitative analysis described in the chapter 3 rewards us with a successful localization result.

4.2 Improved experiments and parametric study

In this section, the pump-probe passive experiments with a set of uncorrelated noise sources distributed on the top surface of the plate described in the previous section 4.1.1 are conducted with the modified parameters obtained from the quantitative analysis of active and passive experiments (see the chapter 3 and the previous section for details) and aimed at improving the image contrast. The parametric studies on N_r, N_s, and virtual emitter position are discussed.

A scheme of the experimental setup is shown in fig. 4.7. It contains $N_s = 18$ noise sources and $N_r = 19$ receivers. Signal processing applied to experiments in this section is the same as described in the previous section 4.1.1.

In fig. 4.8 results of active (chapter 2) and passive reference-free localization algorithms are compared. Here the passive experiment is done with $N_s = 18$ emitters and

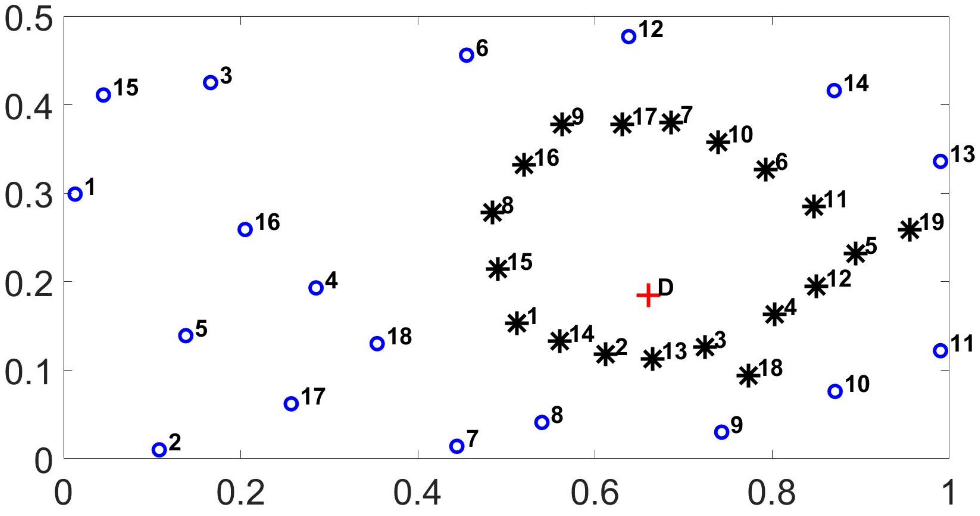

FIGURE 4.7 – Schematic configuration of the considered experiment. The circles denote noise emitters, the asterisks are for receivers and the cross represents defect (CAN) position.

$N_r = 15$ receivers. Both experiments are conducted with the same defect scattering cross-section $\overline{\sigma}$ ($f_0 = 10$ kHz) $= 0.18$ mm (i.e. the same ruler-plate angle, here we neglect variation of contact condition between two successive experiments related to friction), same set of receivers, virtual emitter selected for passive signals processing is the same PZT patch emitting in the active experiment with the coordinates (0.438, 0.277) m, same pump amplitude 4.8 V. For active experiment $M = 780$ slices of $\Delta T = 50$ ms are considered and for passive counterparts there are $M = 3900$ windows of $\Delta T = 10$ ms duration. Contrast for active image is $\mathcal{C}_a = 22$, whereas for passive one $\mathcal{C}_p = 3$, which means that the quality of the passive image is around 7 times lower comparing to the active one under the same conditions. Indeed, in the passive image a lot of background speckles are observed, which points out that the Green's function reconstruction error $n(t)$ (see Eq. (1.9) in section 1.2.2) is essential.

In fig. 4.9 scattering cross-section against time within one pump period is illustrated supplementing the localization results in fig. 4.8. The result resembles harmonic function which is consistent with the pump periodicity and similar to previously obtained results (see section 3.3.1).

To improve signal-to-noise ratio of the image, the number of receivers was increa-

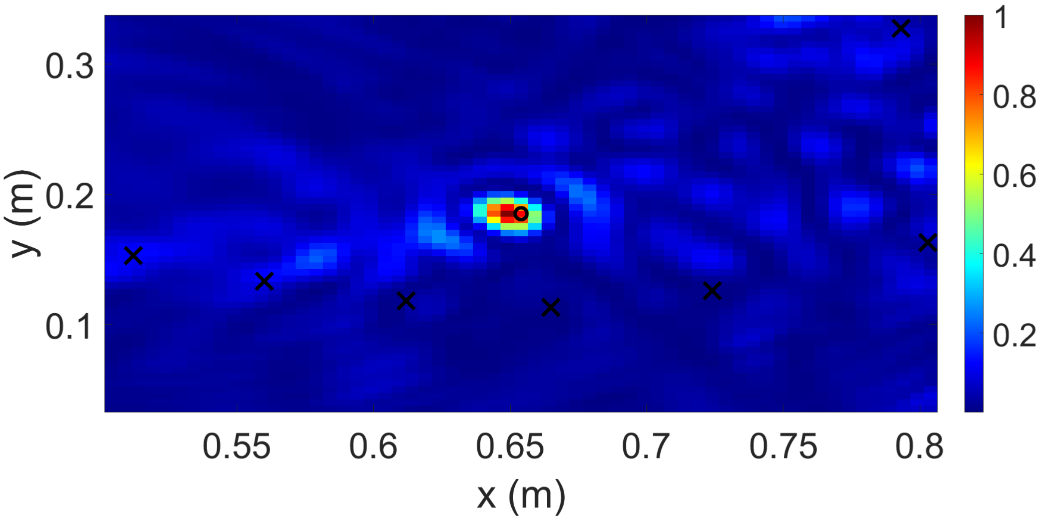

(a) Active result.

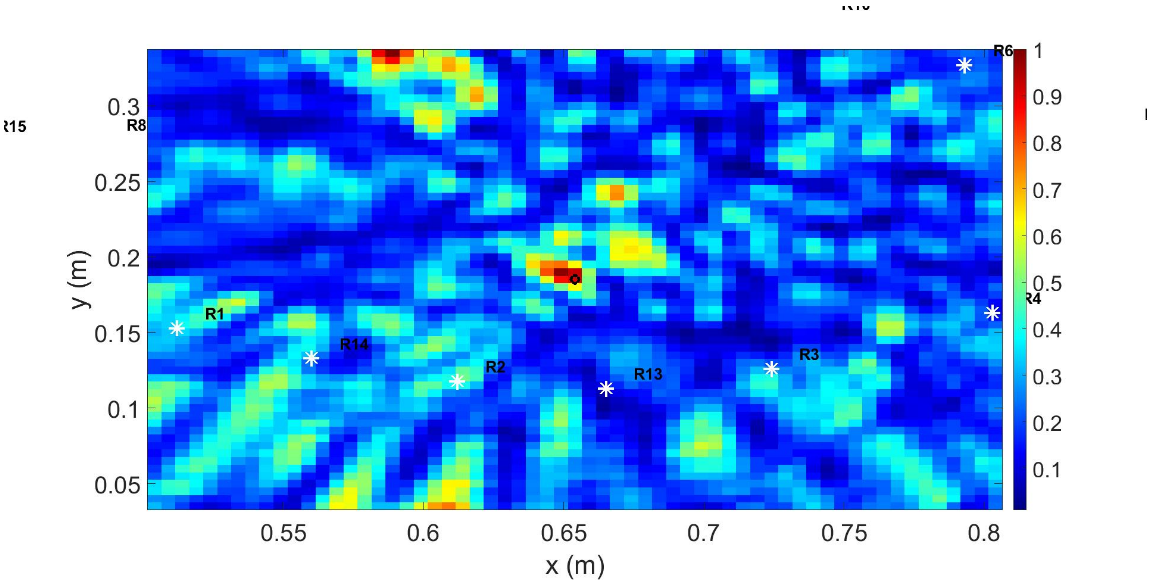

(b) Passive result.

FIGURE 4.8 – Localization results of active vs passive imaging. $N_s = 18$ emitters and $N_r = 15$ receivers. The active emitter (0.438, 0.277) m is the same PZT transducer as the one used as a virtual emitter in passive localization. Defect is located at (0.654,0.185) m.

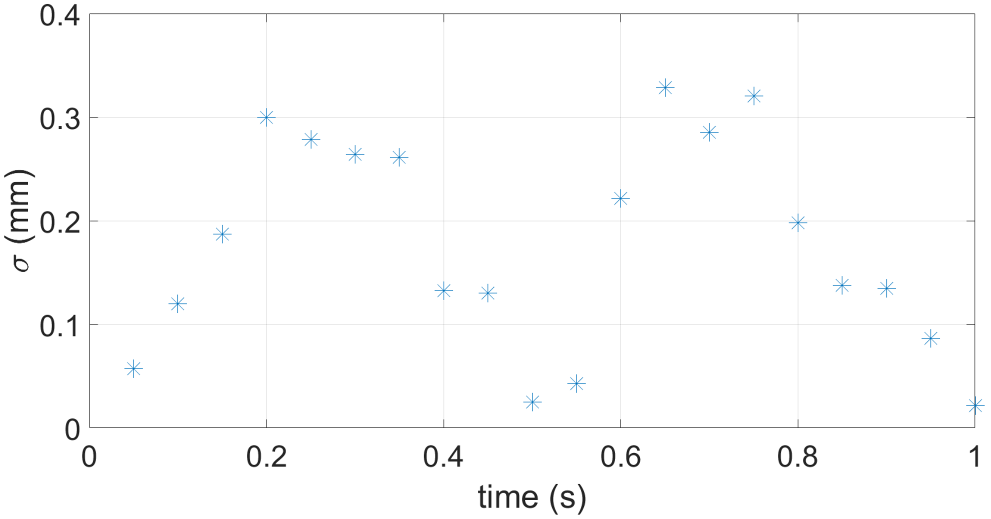

FIGURE 4.9 – Scattering cross-section against time within one pump-period for the experiment comparing active and passive localization algorithm under the same conditions.

sed up to $N_r = 19$. A localization result of this experiment is given in fig. 4.10. The contrast of this image is higher than in fig. 4.8 : $\mathcal{C} \approx 4$. The virtual emitter is located at (0.724, 0.126) m, there are $M = 3900$ windows of duration $\Delta T = 10$ ms.

Finally, for deeper investigation, dependence of image quality on the different involved parameters is studied.

Dependency on number of receivers

Localization results of the study on number of receivers are presented in fig. 4.11. Starting from $N_r = 7$ the defect is well pronounced in the image. Contrast of each image is computed and shown in fig. 4.12 as a function of N_r with $N_s = 18$ noise sources, $M = 3900$ windows of $\Delta T = 10$ ms duration. The graph follows the linear trend with coefficient of determination $R^2 = 0.83$: contrast is proportional to the number of receivers as predicted by theoretical formula Eq. (4.9) for the contrast.

Dependency on number of noise sources

Another study is concerned with contrast dependency on number of noise emitters. Localization images for N_s from 13 to 18 are shown in fig. 4.13. In these experiments

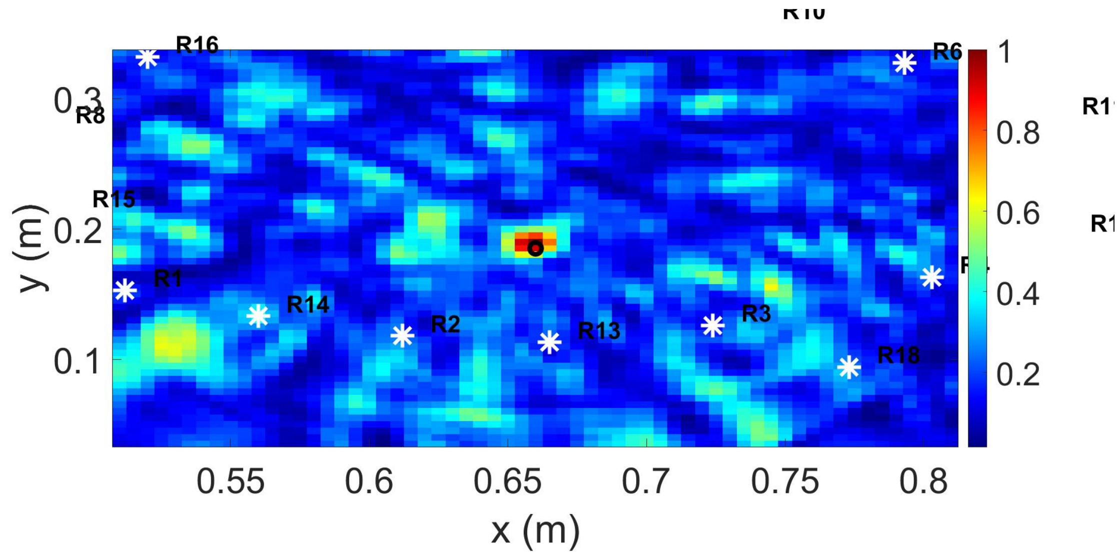

FIGURE 4.10 – Passive dynamic reference-free localization image of a CAN obtained with $N_s = 18$ noise emitters and $N_r = 19$ receivers. Defect is located at (0.66,0.185) m.

there are $N_r = 19$ receivers, $M = 390$ windows of $\Delta T = 100$ ms duration are considered, virtual emitter is located at (0.438,0.277) m. In this case, the defect is detected in all the images. However, in fig. 4.14 it is shown that in this series of experiments the contrast is not proportional to number of sources. The reason for this could be the fact that we tested only one configuration of noise sources for each N_s (as in fig. 4.7). Indeed, this proportionality to N_s is only a theoretical average behaviour over all possible sets of sources that might not be obvious on a single set.

Dependency on virtual emitter position

The last series of experiments was aimed at studying contrast dependency on a virtual emitter position. Localization images are presented in fig. 4.15 for virtual emitters from R_1 to R_{19} and the last image is the sum of all the previous images (incoherent sum). For this series of experiments, there are $M = 2600$ windows with a duration of $\Delta T = 15$ ms.

So with only one virtual emitter, localization quality significantly depends on the mutual positioning of receivers and the defect and also their proximity to the plate boundaries. This drawback, presumably, can be mitigated for the passive method

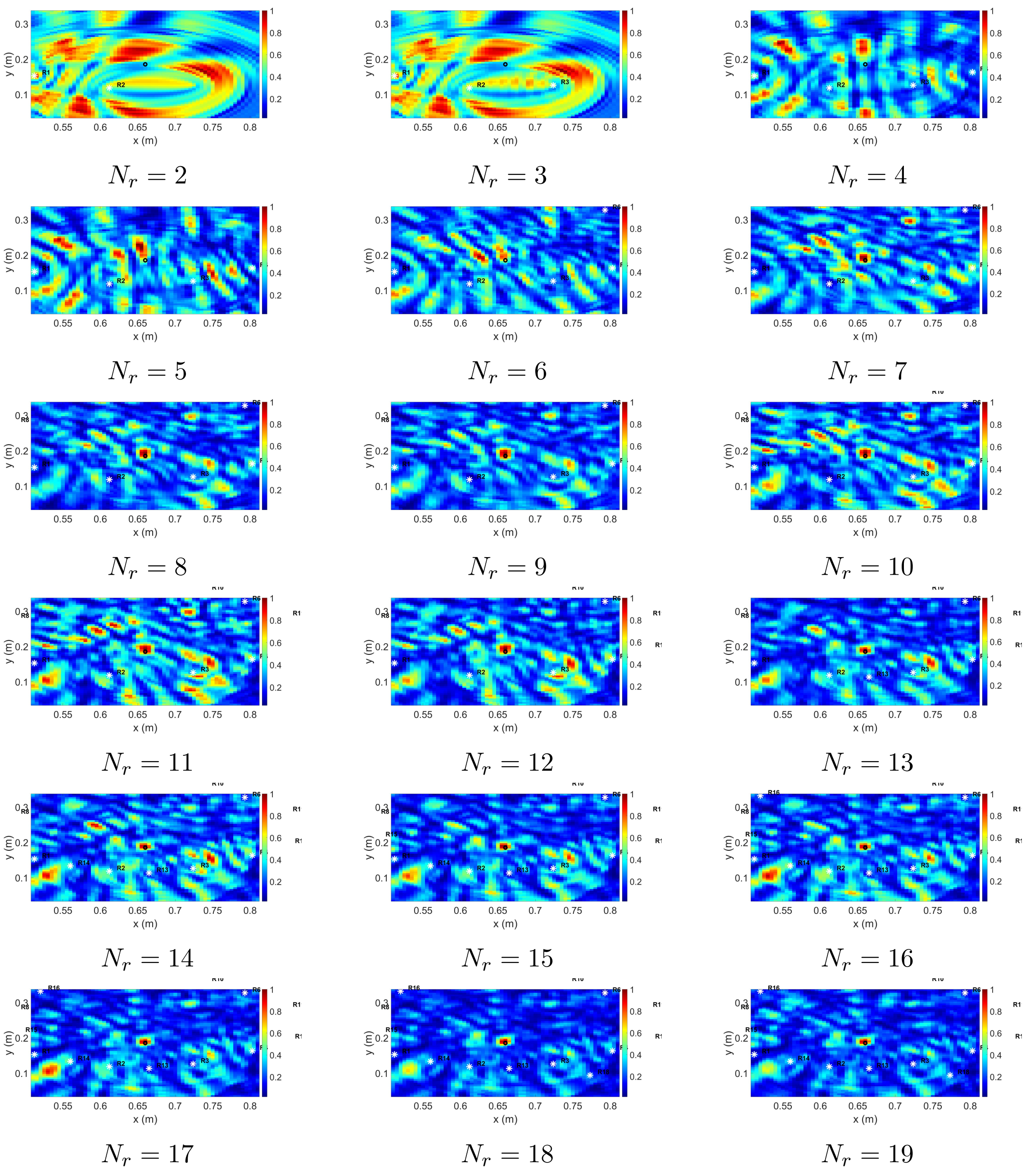

$N_r = 2$ $N_r = 3$ $N_r = 4$

$N_r = 5$ $N_r = 6$ $N_r = 7$

$N_r = 8$ $N_r = 9$ $N_r = 10$

$N_r = 11$ $N_r = 12$ $N_r = 13$

$N_r = 14$ $N_r = 15$ $N_r = 16$

$N_r = 17$ $N_r = 18$ $N_r = 19$

FIGURE 4.11 – Passive localization images with different number of receivers. Number of noise sources $N_s = 18$.

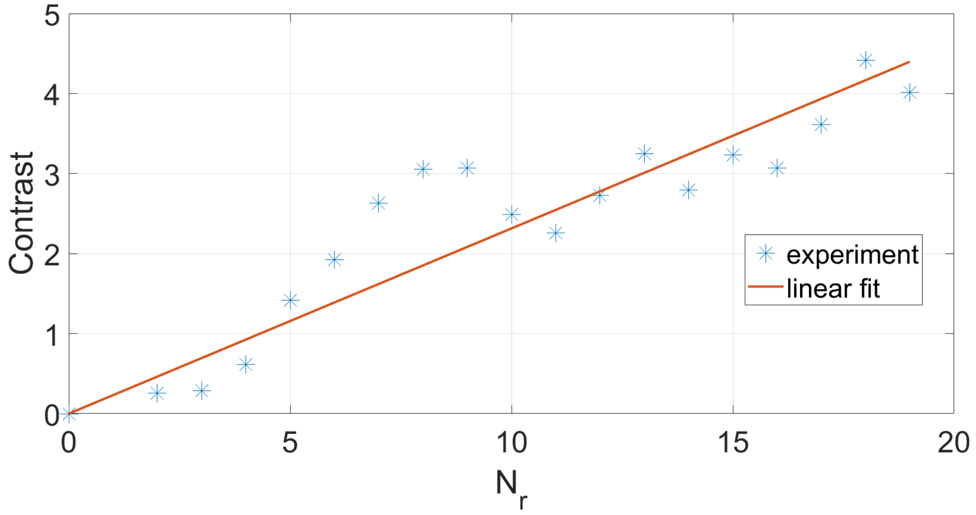

FIGURE 4.12 – Dependency of image contrast on number of receivers.

with using full correlation matrix and coherent imaging.

Even though in some images the defect is not detected, in the last image corresponding to the sum of images obtained with different virtual emitters the defect is well pronounced.

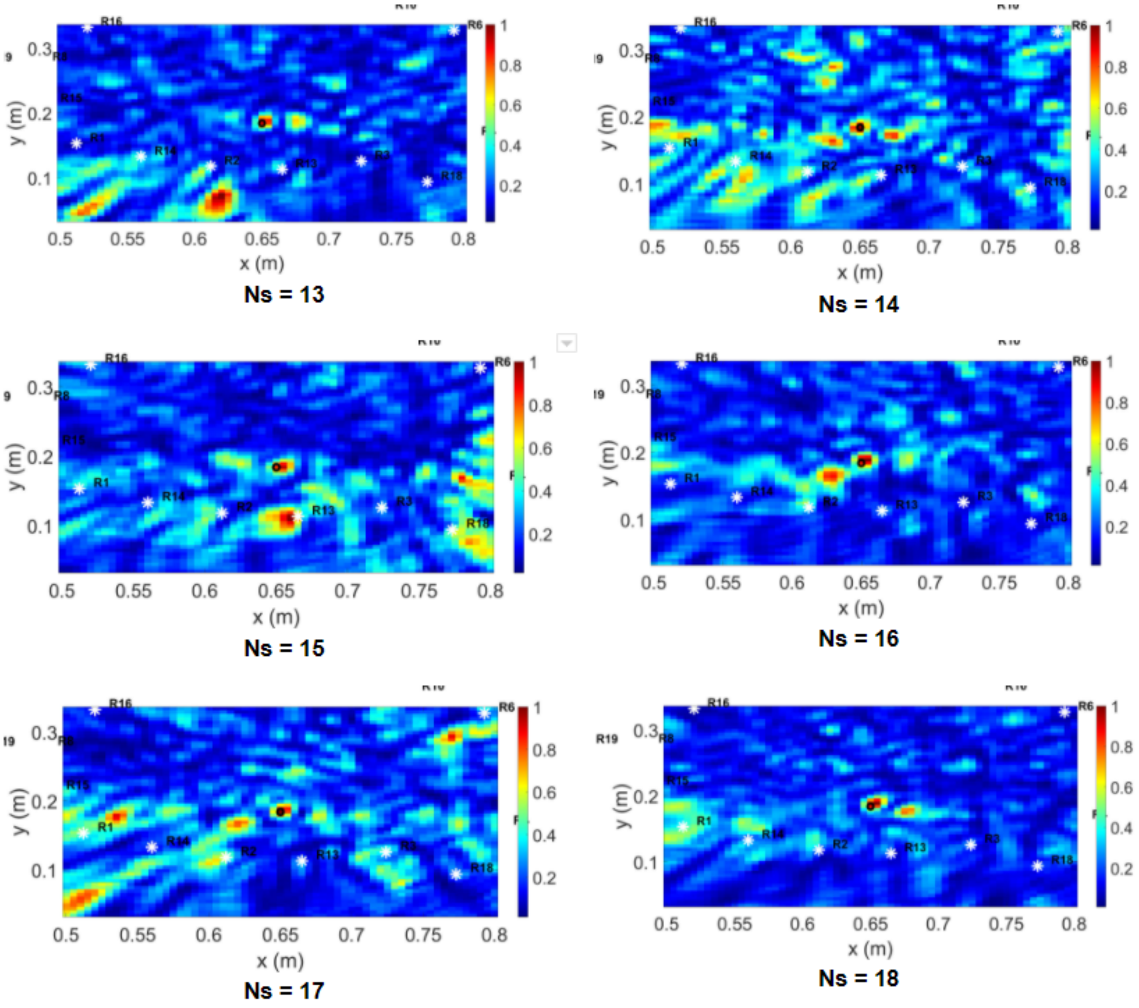

Ns = 13

Ns = 14

Ns = 15

Ns = 16

Ns = 17

Ns = 18

FIGURE 4.13 – Localization images with different number of noise sources N_s.

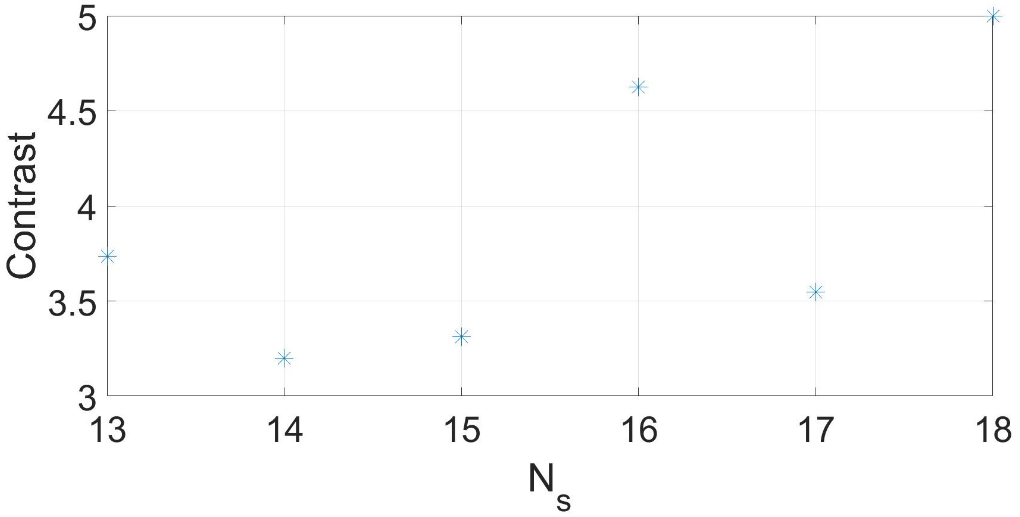

Figure 4.14 – Dependency of image contrast on number of noise sources.

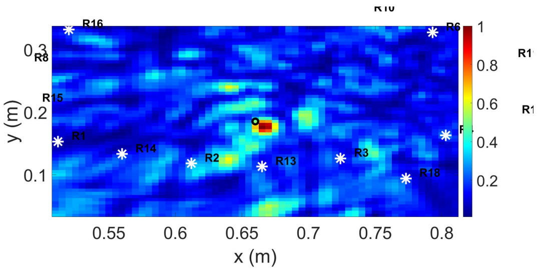

R_1

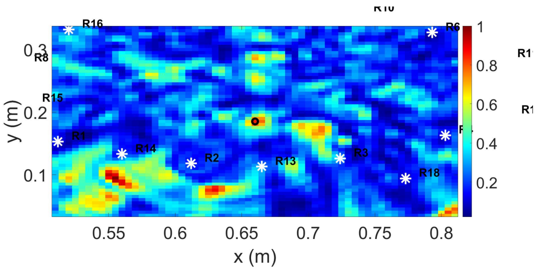

R_2

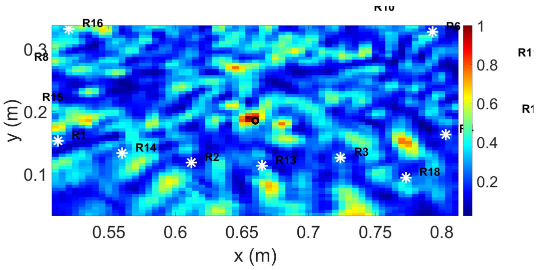

R_3

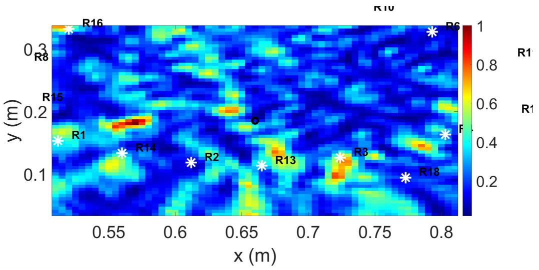

R_4

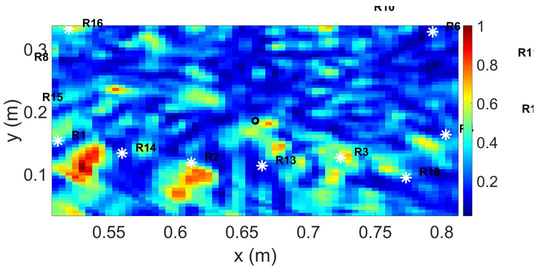

R_5

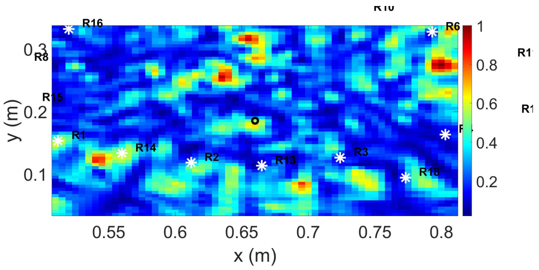

R_6

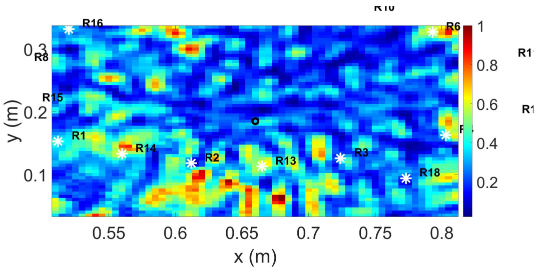

R_7

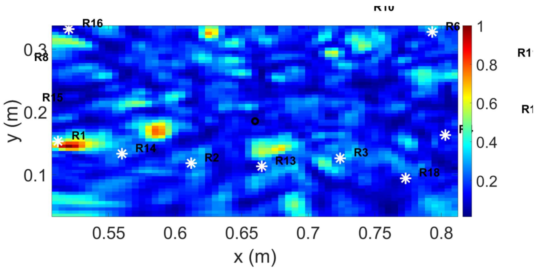

R_8

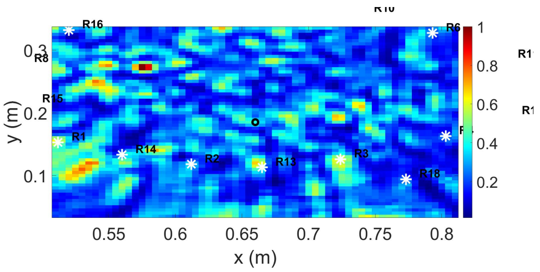

R_9

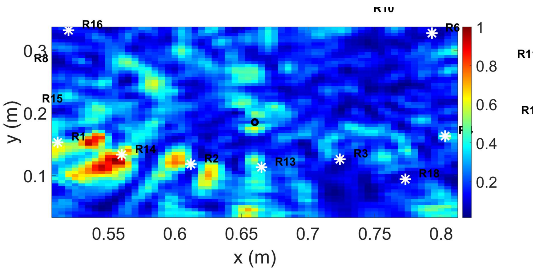

R_{10}

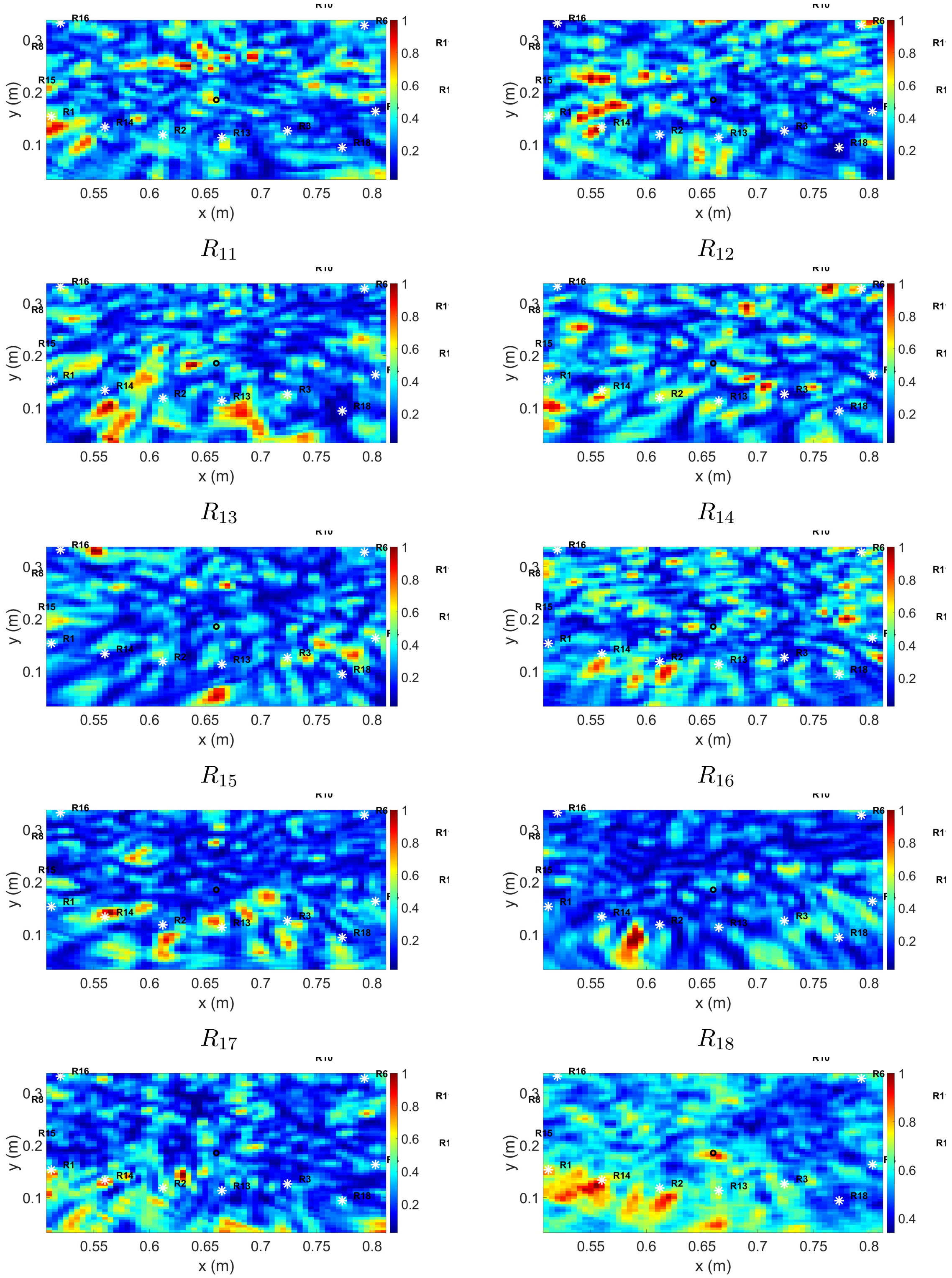

R_{11} R_{12} R_{13} R_{14} R_{15} R_{16} R_{17} R_{18} R_{19}

Sum of images with R_1, R_2,...,R_{19}.

Figure 4.15 – Results of passive dynamic experiments for different virtual emitter positions. The last image is the sum of images with virtual emitters 1-19.

Conclusions

Passive reference-free localization algorithm based on a combination of pump-probe experiment, Green's function retrieval from noise correlations and back-propagation is proposed as a proof of concept of passive dynamic SHM. Contact acoustic nonlinearity has been successfully detected. Successful damage localization images have been obtained.

The guidelines to optimize parameters of the passive pump-probe experiment are the following : high number of sources N_s, high number of receivers N_r, high pump amplitude, the micrometric screw angle should be selected to maximize the defect scattering cross-section.

Chapter 5

Modeling for acoustic wave propagation in a thin plate with an artificial CAN

Contents

Introduction

This chapter is concerned with physical modeling for ultrasonic waves propagation in a thin plate in the presence of localized contact acoustic nonlinearity (CAN). We recall an existing approach to modeling frictional contacts excited by arbitrary signals and calculate a load-displacement relationship in that situation. In the considered example, the contact is activated by the Lamb wave propagation in a thin plate that generate a specific response in terms of contact loads that, in turn, perturbs the propagation medium and induces secondary waves in there. The secondary waves propagating in the plate are qualitatively similar to whose generated in the experiments described in chapter 2. The chapter is concluded by presentation of a modeling tool that takes into account the above-mentioned phenomena and imitates wave-contact interactions in simplified 2D plate-like geometry. This numerical tool can be used as a prototype for real numerical support software accompanying structural health monitoring experiments such as those described in the chapter 2.

As noted, real contact acoustic nonlinearity occurs most often in the presence of damage (cracks, delaminations, etc.) or degradation of artificially produced joints (welds, glue joints). In these cases usually of interest for SHM, the contact is between areas of rough surfaces with friction excited by a complex shaped acoustic signal. However, in this work we consider a model contact nonlinearity representing a Hertz-Mindlin type contact, in which the frictional contact interaction occurs between two geometrically smooth axisymmetric bodies, i.e. in our case between a sphere and a plate. The next section describes the existing model of contact interaction in such a system when it is excited by arbitrary in time normal and tangential displacements (method of memory diagrams). The method was originally developed for axisymmetric bodies but, under some additional assumptions, can also be applied to the contact of rough surfaces. The resulting relation between the stresses and displacements in the contact area is a boundary condition for the acoustic problem whose solution is the purpose of the theoretical part of this thesis.

5.1 Load-displacement relationship in contact acoustic nonlinearity under arbitrary oblique excitation

5.1.1 Normal component of contact interaction for axisymmetric bodies and for rough surfaces

The classical problem for the force N and displacement a arising from the normal compression of two balls is solved by H. Hertz [91], who obtained the following result :

$$\begin{cases} N(a) = \frac{4}{3}E^{*}R^{*1/2}a^{3/2} \\ c = \sqrt{Ra}\,. \end{cases} \tag{5.1}$$

Here E^{*} is effective elastic modulus and R^{*} is effective radius. E^{*} is defined in Eq. (2.5) where $E_{1,2}$ are Young's moduli and $\nu_{1,2}$ are Poisson's ratios for materials in contact. Here R^{*} is given by

$$\frac{1}{R^{*}} = \frac{1}{R_1} + \frac{1}{R_2}\,.$$

In the considered case radius of half-space $R_2 = \infty$ and, consequently, $R^{*} = R_1 \equiv R$, where R is sphere's radius.

This solution can be generalized (Galin [105]) for the contact of two axisymmetric bodies of arbitrary (not necessarily spherical) shape. For two axisymmetric bodies [106] the key relationships can be written as follows :

$$\begin{cases} N = \dfrac{2E^{*}}{1-\nu^2}\Big(ca - \displaystyle\int_0^c \frac{rz(r)}{\sqrt{c^2-r^2}}\mathrm{d}r\Big) \\ a = \displaystyle\int_0^c \frac{cz'(r)}{c^2-r^2}\mathrm{d}r\,, \end{cases} \tag{5.2}$$

where r is the radial coordinate, c is the contact radius, $z(r)$ is a function describing the gap between the two bodies in the unstrained state (the total gap equals $2z(r)$), $z'(r)$ is its derivative, and ν is Poisson's ratio. When $z(r) = R - \sqrt{R^2 - r^2}$, Eqs. (5.2) yield Hertz's solution (5.1).

For rough surfaces, description of the normal interaction by exact mechanical methods is hardly possible and is constructed here with the use of model considerations instead. The model proposed here is based on the following principles.

Contact of rough surfaces can be described using three different parameters related to the contact area : the nominal contact area A_n defined by replacing rough surfaces by ideally plane ones, the real (atomic) contact area A, and the geometric (truncated) contact area A_g obtained in a virtual situation when rough profiles can freely penetrate into each other or, equivalently, when all roughness elements of each surface located higher than a certain height are virtually cut off. Two of these contact areas are also illustrated in fig. 5.1. As can be observed, the real atomic contact area A between two bodies with rough surfaces is only a small part of the nominal area A_n. The proportionality $A \sim N$ was proposed by Bowden and Tabor in 1939 [107] ; a more recent discussion on the proportionality can be found in [108]. Both empirical and theoretical arguments suggest that

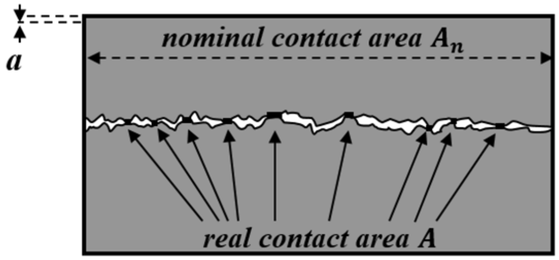

FIGURE 5.1 – Illustration of the nominal contact area A_n and the real contact area A.

$$A = \frac{2\kappa(1-\nu^2)}{Eh'}N \tag{5.3}$$

with h' equal to the root mean square of the random surface slope, and $\kappa \approx 2$ (see [109] and references therein for experiments, [110] for theory, [111] for the discussion on the coefficient κ, [112] for theoretical and numerical examples).

Further, we introduce the random gap ξ between the surfaces (2ξ is the full gap, ξ is related to one body) and denote $\phi(z)$ as its distribution. Then it is easy to express the ratio A_g/A_n from purely geometric consideration as

$$\frac{A_g}{A_n} = \int_0^a \phi(z)dz\,. \tag{5.4}$$

Finally, the real and geometric contact areas can be linked by a model relationship. In particular, if all microcontact spots are approximated by strained spheres, a simple relation

$$\frac{A}{A_g} = \eta = \frac{1}{2} \tag{5.5}$$

follows from the Hertz theory [91] (see also second equation in Eqs. (5.1) below). For non-spherical shapes of asperities, the value of η can deviate from 1/2. Combining Eqs. (5.3), (5.4) and(5.5) we obtain an analytical expression linking N and a,

$$N(a) = \frac{\eta h' E}{2\kappa(1-\nu^2)} \int_0^a \phi(z) \mathrm{d}z \,. \tag{5.6}$$

In case of negative normal displacement a – when two bodies move away from each other, – we set N equal to zero which actually corresponds to the absence of adhesion. Equation (5.6) means that the normal reaction of a crack section is determined by the gap (aperture) distribution which, in turn, depends on the nature of a crack. Since typical acoustic excitations can always be considered as small perturbations, the normal reaction in the acoustical strain range will mainly depend on the tangent to the curve $\phi(z)$ at $z = 0$ (i.e. the first-order Taylor series approximation) illustrated in fig. 5.2.

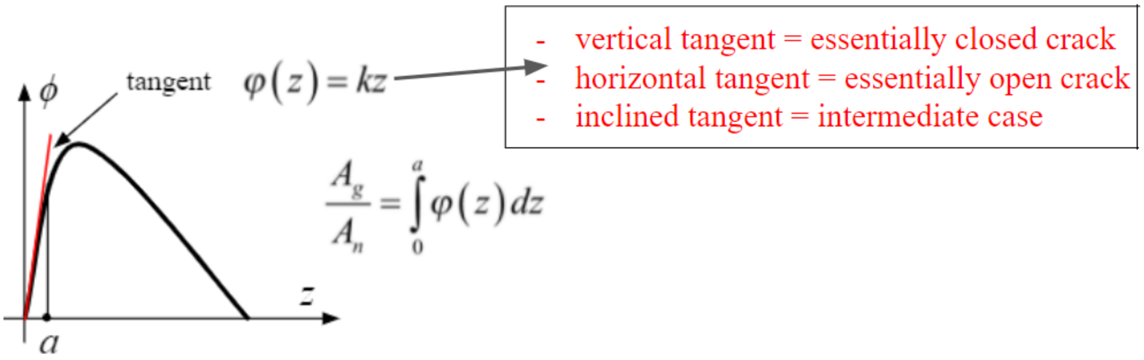

FIGURE 5.2 – Example of the gap distribution function $\phi(z)$ illustrating the type of crack depending on the slope of its tangent at $z = 0$.

As such, three cases can be distinguished : a vertical tangent, a horizontal one, or a tangent with inclination angle between 0 and $\pi/2$. A vertical tangent implies that even for a small compressive displacement a, a non-zero contact area will be immediately formed. In practice, this refers to highly conforming surfaces at the atomic level. Secondly, a horizontal tangent refers to an essentially open crack in which points in atomic contact practically do not appear. Finally, an intermediate tangent inclination coefficient $k (0 < k < \infty)$ results in the approximation which yields the following result :

$$N(a) = \frac{\eta h' E k}{4\kappa(1-\nu^2)} a^2, a > 0\,. \tag{5.7}$$

The same second-order dependency ($N(a) \sim a^2$) has been introduced by Biwa et al. [113] based on existing experimental data for aluminum-aluminum contact and was already used by Yuan et al. [114] for modeling the nonlinear interaction of a compressive wave with a soft contact interface between two solid blocks of aluminum. This suggests that the quadratic dependency is a possible approximation for two globally plane surfaces with uncorrelated roughness brought into contact. As an extension we assume that Eq. (5.7) is also approximately valid for fatigue cracks since the internal stresses released during cracking and the associated microscopic displacements result in a similar loss of conformity at the atomic scale. Microscale composite roughness (related to the random gap between two surfaces) that mainly contributes to the acoustic response can thus be considered as uncorrelated.

The quadratic approximation is not the only possible form for modeling the normal load-displacement relationship. In [115, 116] it is shown that rough surfaces with various fractal dimensions correspond to different powers in approximation of the kind of Eq. (5.7).

So, in any of the considered cases the law of the normal interaction is given by the analytical formula $N = N(a)$. For the model CAN used in our experiments, this is power law with an exponent of 3/2. For rough surfaces corresponding to a real defect, the exponent will be different. However, the general solution for axisymmetric bodies makes it possible to simulate this dependence by selecting the gap function $z(r)$. In the present work, the contact between the sphere and the plate is used for simplicity. In the following, we will show that such a system can approximate, in terms of acoustic behavior, the contact between rough surfaces with some statistical properties, even though the law of contact interaction is different for these systems. This fact can be an argument in favor of using the chosen model CAN instead of the real damage in SHM problems.

5.1.2 Tangential component of frictional contact interaction for axisymmetric bodies and for rough surfaces

Calculating the tangential component of the contact interaction in the presence of friction is more challenging than modeling for the normal component. First of all, friction is a hysteretic process i.e. a one-to-one relationship between the tangential force T and the tangential displacement b is absent. Besides, Coulomb's law of dry friction, which is a typical model form of frictional interaction, does not provide any relation between T and b at all, but only defines at what relation between normal and tangential forces there will be slip, and at what relation there will not. Further, if the contacting bodies have relief, Coulomb's law has to be set not for the bodies as a whole but at the level of local stresses and displacements in the contact area. Different fragments of the contact area are loaded differently, resulting in sliding in some areas and in stick in others. This situation can be called partial slip, which is therefore an additional mode of contact interaction besides the obvious two - full slip in the whole contact area and loss of contact. All of these factors require a multi-step analysis, which should eventually lead to some kind of integral model [117] developed a few years ago by our research team.

a) Constant load and partial slip

First of all, let us outline here a method for solving the axisymmetric problem in the case of partial slip (fig. 5.3). For spherical bodies this case is called the Hertz-Mindlin problem [118] or the Cattaneo-Mindlin problem [119]. If the normal force is kept constant while the tangential one increases, the solution is written down in the following simple form :

$$\begin{cases} T = \frac{4\mu E^*}{3R^*}(c^3 - s^3) \\ b = \frac{\mu\theta}{R^*}(c^2 - s^2)\,, \end{cases} \tag{5.8}$$

where μ is a dry friction coefficient, R^* is an effective radius defined in Eq. (5.1.1), c is a radius of a contact zone, s is a radius of stick zone, E^* is defined in Eq. (2.5).

It is important to note here that this result is obtained by neglecting the dissimilarity effects which arise due to differences in elastic constants and shapes of the strained bodies in contact. Thus, for example, two non-identical spheres in a purely normal interaction can experience slip only due to a different pattern of tangential deformations in each body caused by the Poisson effect. The disregard of dissimilarity effects is quantified by the requirement of Dundur's constant β to be small

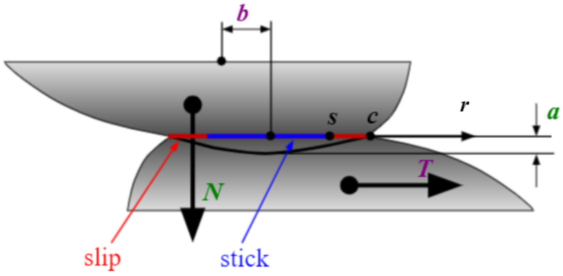

FIGURE 5.3 – Illustration of the partial slip regime for an example of two spheres pressed against each other. Blue segment denotes stick zone, red segments are for slip zone.

$$\beta = \frac{G_2(\kappa_1 - 1) - G_1(\kappa_2 - 1)}{G_2(\kappa_1 + 1) + G_1(\kappa_2 + 1)} \,. \tag{5.9}$$

Here $G_{1,2}$ are shear moduli, $\kappa_{1,2} = 3 - 4\nu_{1,2}$, and $\nu_{1,2}$ are Poisson's ratios of the materials (see, for instance, [120]). The elastic similarity means that normal and tangential interactions are uncoupled in some sense. In many practical cases, even if the above conditions of elastic similarity are not exactly fulfilled, the dissimilarity effects are found to be numerically small [121, 122, 123, 124].

Note now that the expression Eq. (5.8) is similar to the solution

$$\begin{cases} N = \frac{4E^*}{3R} c^3 \\ a = \frac{c^2}{R} \end{cases} \tag{5.10}$$

of Hertz problem. This fact makes it possible to rewrite the Cattaneo-Mindlin solution [122], [119] in a compact form, which turns out to be true for the contact of arbitrary axisymmetric bodies as well :

$$\begin{cases} T = \mu(N(c) - N(c = s)) \\ b = \theta\mu(a(c) - a(c = s)) \,, \end{cases} \tag{5.11}$$

where θ is a constant depending on materials of contacting half-spaces (sphere and plate, steel and aluminum) [106] :

$$\theta = \frac{\frac{(2-\nu_1)(1+\nu_1)}{2E_1} + \frac{(2-\nu_2)(1+\nu_2)}{2E_2}}{\frac{1-\nu_1^2}{E_1} + \frac{1-\nu_2^2}{E_2}} \,.$$

Here $a(c)$ and $N(c)$ are the analytical relations (see Eqs. (5.10)) relating the normal displacements and forces to the contact radius. Moreover, if the law of normal interaction is known $N = N(a)$, it is easy to represent the previous relation as

$$\begin{cases} T = \mu(N(a) - N(a = q)) \\ b = \theta\mu(a - q) \end{cases} \tag{5.12}$$

in which the geometric parameters of the contact are not present explicitly. Here q is defined as $q = a(c)|_{c=s}$. These parameters, however, are contained here implicitly in the dependence $N(a)$. The form in Eq. (5.12) has an important consequence, which is that if the laws of normal interaction of two contact systems are the same, then their tangential behavior will also be the same. Hence, in particular, it follows that the contact of two rough surfaces can be replaced by the contact of axisymmetric bodies with the same normal reaction – their tangential behavior will also be the same. This conclusion is strictly valid for surfaces in which all asperities are spherical in shape. As a model assumption, one can also assume that this property holds for arbitrary (non-spherical) asperities if their random shape is isotropic, i.e., in particular, there is no direction in which the roughness pattern will be statistically more elongated than in the other one.

The solution in Eq. (5.12) is called the Reduced Elastic Friction Principle [122], which means that the tangential interaction is determined by the difference between the actual normal load-displacement relationship and the same relationship in which the contact radius is replaced by the slip zone radius (so that the corresponding load is virtually reduced).

b) Arbitrary oblique load and partial slip

Suppose now that the forces (or displacements) loading the contact are not constant over time, but vary in an arbitrary law, with their vectors not leaving the same plane. This means that the contact interaction is described by the relationship between the forces $N(t)$, $T(t)$ and displacements $a(t)$, $b(t)$. This relationship can be calculated using the Method of Memory Diagrams (MMD), which is a semi-analytical solution to the problem in which all the key relationships are given analytically, but the input parameters are determined by the algorithm.

These analytical relationships for tangential force T and displacement b are as follows

$$\begin{cases} b = \theta\mu \int_0^a D(\alpha)\mathrm{d}\alpha \\ T = \mu \int_0^a D(\alpha)\frac{\mathrm{d}N}{\mathrm{d}a}|_{a=\alpha}\mathrm{d}\alpha \,, \end{cases} \tag{5.13}$$

where $D(\alpha)$ is an internal function of the system in question, which encapsulates all the information about the memory in it, and is called a memory diagram. Whereas the tangential load and displacement are given by analytical expressions, we shape of the memory diagram sitting inside is defined by an algorithm. In particular, with a simple loading protocol indicated in (fig. 5.4 a), it has a simple form expressed as follows (see fig. 5.4 b)

$$D(\alpha) = \begin{cases} 1, 0 \leq \alpha < q \\ 0, q \leq \alpha \leq a\,. \end{cases} \tag{5.14}$$

Substituting it into the system Eq. (5.13), provides a known result from Eq. (5.12). With an arbitrarily varying load (fig. 5.4 c), its form is more complex (fig. 5.4 d)

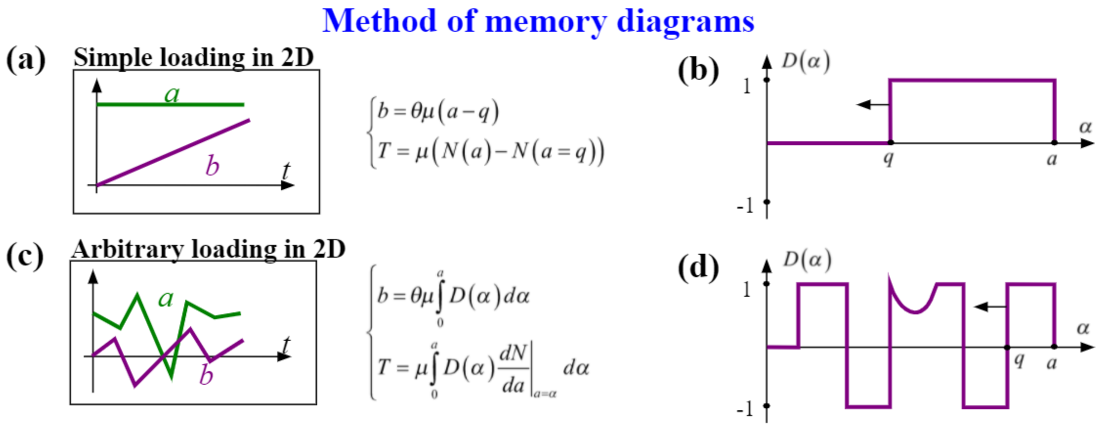

FIGURE 5.4 – Examples of memory diagrams (b) and (d) for simple (a) and complex (c) loading protocols, respectively. For the simple case, load-displacement relationship is known, for the complex one, method of memory diagrams is applied to find it.

The algorithm is discussed in detail in [125] and [117]. It updates the shape of the memory diagram at each change of input parameters of the system by small values ΔN and ΔT for the force-driven system, or Δa and Δb for the displacement-driven system. Thus, if the arguments in the problem are displacements and the functions are forces, then based on the known values Δa and Δb, the algorithm calculates current change in the memory diagram $D(\alpha)$, which satisfies the first equation in (5.13) written for increments. The memory diagram is then used to compute the responses ΔN and ΔT using known $N(a)$ and the second equation in (5.13). As a result, for any loading history the tangential response of the system is automatically calculated with the known normal loading curve $N(a)$, in which the entire system geometry is encoded.

c) General case of arbitrary in time oblique excitation

So, the MMD allows one to calculate the tangential response of the system to an arbitrary in time oblique shift, but only in the case of partial slip. Let us consider what happens when the non-slip zone decreases to the point $r = 0$ and then disappears completely.

For the force-driven system the tangential force will reach a critical value of μN and then, if this threshold is exceeded, a part of the tangential force cannot be compensated for by friction. In the absence of other forces, the non-equilibrated component causes accelerated motion. This description is highly undesirable as it goes beyond the closed-form relationship between forces and displacements and depends on the external conditions of the contact.

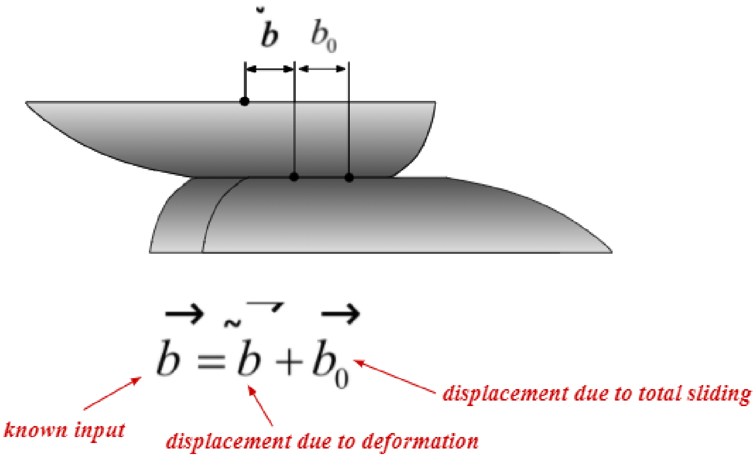

FIGURE 5.5 – Tangential displacement b contains two components corresponding to total sliding b_0 and partial slip $\tilde{b}$, respectively.

For the displacement-driven system, however, this difficulty does not arise. In order to build a closed-form load-displacement relationship, consider displacement b as the sum of two components : one part b_0 corresponding to total sliding and the other one $\tilde{b}$ to partial slip (fig. 5.5) :

$$b = b_0 + \tilde{b}\,. \tag{5.15}$$

The idea [126] behind this separation can be illustrated as follows. Suppose the tangential loading increases while keeping constant normal compression $N = N(a)$ corresponding to a certain normal displacement a. The bodies in contact move away from each other under load in both normal and tangential directions. In addition, the tangential receding $\tilde{b}$, in contrast to the normal one, a, is accompanied by partial slip. According to the MMD based on the Coulomb friction law, $\tilde{b}$ is not allowed to grow infinitely. Once the maximum value $\tilde{b}_{max} = \theta\mu a$ is achieved, the bodies can not deform anymore and a total sliding process develops when the very last stick point belonging to one face separates from its neighbor at the opposite one. The tangential displacement between those points is denoted b_0 and corresponds to the contribution from total sliding. In other words, b_0 is a reference point mismatch, in some sense.

Crack state	If	Then	Memory diagram
(i) Contact loss	$a < 0$	$\tilde{b} := 0 \quad b_0 := b$ $T = N = 0$	
(ii) Total sliding	$a \geq 0$ $\lvert\tilde{b}\rvert \geq \theta\mu a$	$\tilde{b} := \pm\theta\mu a \quad b_0 := b - \tilde{b}$ $T = \pm\mu N$	
(iii) Partial slip	$a \geq 0$ $\lvert\tilde{b}\rvert < \theta\mu a$	$b_0 := b_0 \quad \tilde{b} := b - b_0$ $T = MMD(\tilde{b})$	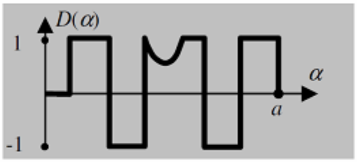

FIGURE 5.6 – Three possible contact states. For each case, the following information is supplied : conditions under which the case occurs, solutions for components and , solutions for forces N and T, and memory diagrams.

Fig. 5.6 provides an overview of the full concept in case both normal and tangential displacements a and b evolve in an arbitrary manner. The scheme explains how to calculate the forces N and T for any given value of displacements a and b. In order to do so, the tangential displacement components b_0 and $\tilde{b}$, together with the corresponding memory diagram should be updated. The updating operation for the tangential displacement components is denoted using the assignment operator « := », which means that values obtained at the previous time step are overwritten by new ones [126].

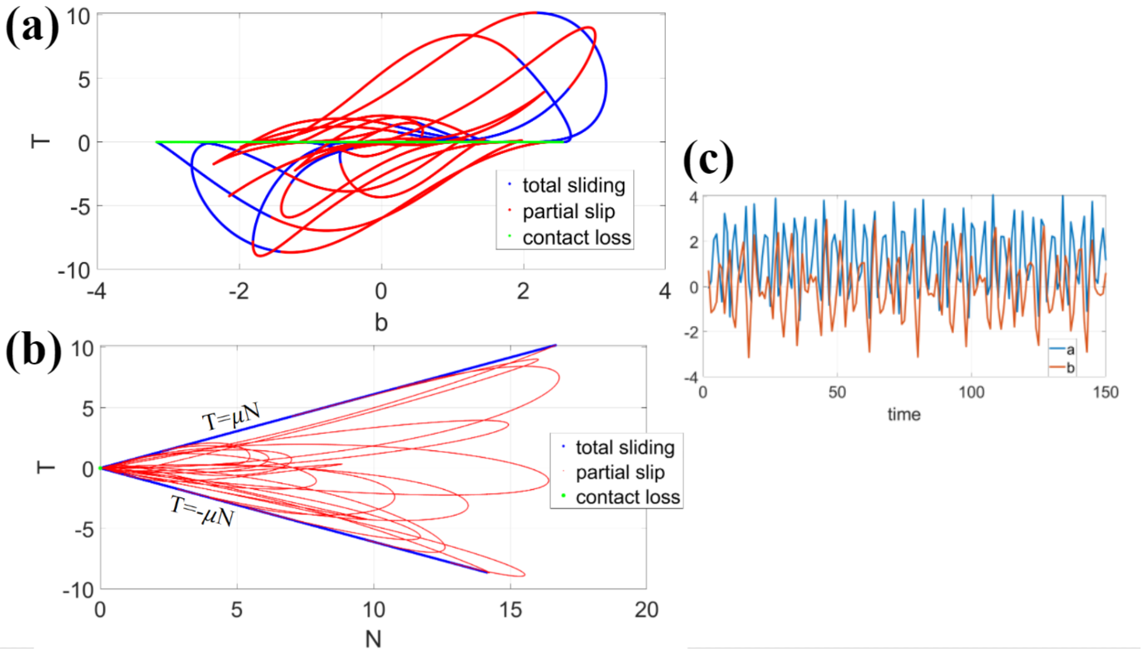

FIGURE 5.7 – (a) Tangential force as a function of tangential displacement and normal force (b) in case of particular displacement histories shown in (c).

A typical result provided by the MMD with some particular normal and tangential displacement histories is illustrated in fig. 5.7. In this example $a = 1.3 + 1.9\sin(1.7t) + 0.9\sin(2.4t)$, $b = \sin(t) + 1.5\sin(1.4t) + 0.8\sin(2.1t)$. Note that since the tangential force is a history-dependent function of two arguments a and b, its behavior is more complicated than typical patterns for uni-variate hysteresis with closed loops. The curve is composed of several fragments marked in fig. 5.7 a with different colours : blue stands for total sliding in which $T = \pm\mu N$, red stands for partial slip, and green is for contact loss.

The same regimes can be seen in fig. 5.7 b visualizing the link between the normal and tangential forces. As one can see, total sliding indeed corresponds to fragments $T = \pm\mu N$. Parts of curves $T = T(N)$ located in between the delimiting lines $T = \pm\mu N$ are related to the partial slip regime, while the case of contact loss corresponds to the point (0,0). This behavior is in complete agreement with the Coulomb's friction law.

The algorithm in fig. 5.6 completes the description of the contact model. It is formally valid for axisymmetric bodies ; however, under some limitations, can be considered as a good approximation for contact of rough surfaces as well. Indeed, following the Greenwood and Williamson approach [127], all asperities can be considered as spherical or axisymmetric. Even if they are not, i.e. individual microcontacts can have arbitrary shapes, in many cases it is reasonable to consider isotropic roughness when along all possible directions parallel to the global surface plane all statistical properties of roughness are the same (one of exceptions is rough surfaces obtained by grinding). In the isotopic case, each microcontact can be effectively replaces by a pair of equivalent axisymmetric bodies for which the above theory is applicable.

Finally, we will list the assumptions that were used explicitly or implicitly to construct the method.

1. Loading is in one plane only (i.e. in 2D) ; 3D extensions are discussed in [128].
2. Only shift is considered ; torsion and rolling are ignored.
3. The Coulomb friction law with friction coefficient μ is postulated for contact stress fields.
4. The model is quasi-static : differences between static and dynamic friction are not considered, inertial behavior in the material in the vicinity of the contact zone is neglected.
5. Plasticity and adhesion are ignored.
6. The normal to the contact area (or all normals to all microcontact areas for rough surfaces) does not rotate and stays in the same direction.
7. The normal solution is a known bi-unique function $N = N(a)$ independent of the tangential loading.
8. Dissimilarity effects are neglected.
9. The reduced elastic friction principle is valid for the considered geometry (exact for axisymmetric bodies and reasonable approximation for isotropic rough surfaces).

In the next section, the Method of Memory Diagrams (automated Hertz-Mindlin solution) will be used for computing forces excited by the Lamb waves at CAN location.

5.2 Modeling for contact acoustic nonlinearities excited by the Lamb waves

In this section, contact forces excited by the Lamb wave for two types of contact acoustic nonlinearities will be calculated from the known wave displacements : for the Hertz-Mindlin CAN (HM-CAN) and for rough surface CAN (RS-CAN). Here the HM-CAN corresponds to the physical model for damage used in the experiments that represents a contact between a sphere and a plate, whereas the RS-CAN refers to a more realistic case where a defect is a crack or a loose joint with rough surfaces. Both CANs produce nonlinear force reaction on acoustic excitation ; the obtained forces as functions of time can be interpreted as a secondary waves' source located at small area (practically a point) on the plate surface. In what follows we focus on the interaction of CANs and the Lamb wave in more detail.

5.2.1 Hertz-Mindlin CAN

In the considered geometrically idealized experimental case, a small steel ball pressed against a top surface of an aluminum plate is exited by the A0 Lamb mode. Then the coordinates of the ball's center of mass supposed to be zero when the bodies are unstrained are given as a superposition of wave displacements and contact displacements :

$$\begin{cases} x = b + u_x = 0 \\ y = a + u_y \,. \end{cases} \tag{5.16}$$

The former equation takes into account that horizontal motion is prohibited by a device positioning the sphere. This taboo comes from the experiment in which sphere's horizontal motion on the plate activates acoustic emission due to friction and makes the defect detection method reference-based due to the varying sphere's coordinate. The latter equation in the system (5.16) is to be combined with the equation of motion :

$$m\frac{\partial^2 y}{\partial t^2} = N_0 - N(a) \tag{5.17}$$

with m, the mass of the sphere. Here N_0 denotes precompression force that has two components, elastic prestress and gravity, and is positive for the y-axis directed downward, whereas the normal contact reaction force $N(a)$ is directed upward. The geometry of the problem is illustrated in fig 5.8b.

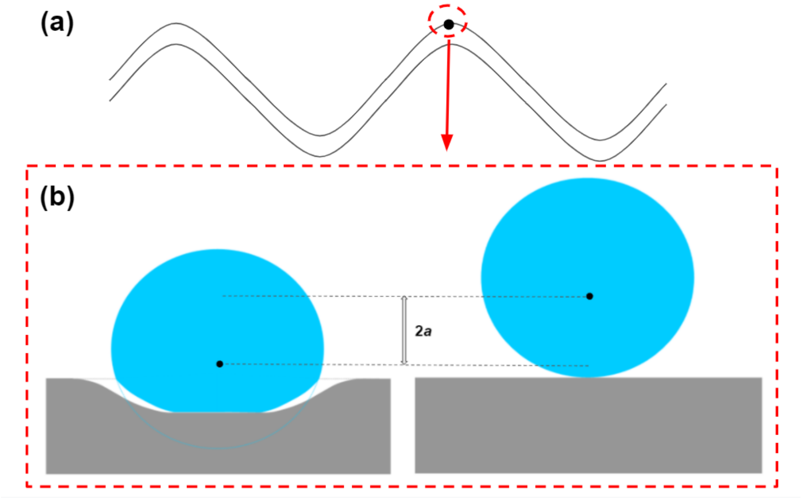

(a) Small ball pressed against a plate is exited by the Lamb wave (plate's deformation is highly exaggerated). (b) Zoom on the ball with the normal contact displacement shown.

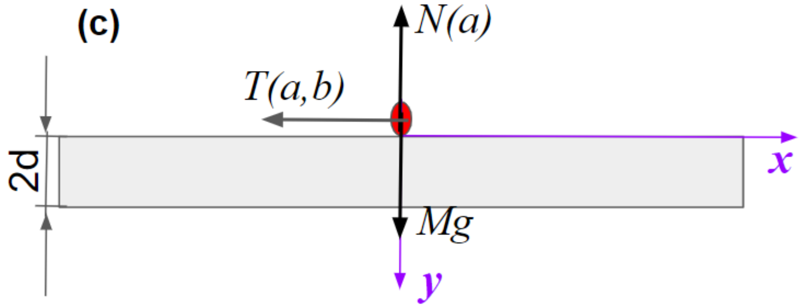

(c) Physical problem formulation for HM-CAN.

FIGURE 5.8 – Model of HM-CAN.

The equation of motion has to be supplemented by the calculation of the normal and tangential contact forces given by

$$\left\{ \begin{array}{l} N(a) = \frac{4}{3} E^* R^{*1/2} a^{3/2} \\ T(b,a) = T_{MMD}(b,a)\,, \end{array} \right. \tag{5.18}$$

where T_{MMD} is an automated analytical solution given by the Method of Memory Diagrams described before in section 5.1.2.

Besides, we have to specify explicitly the known solution Eq. (1.3) for the A0 Lamb wave. This stationary solution is fully harmonic in time $\forall t \in (-\infty, +\infty)$. However, in order to solve the equation of motion, one has to set initial conditions in terms of coordinates or contact displacements which are *a priori* unknown in the stationary wave regime. To avoid this difficulty, we assume the initial condition $a = a_0$, with a_0, contact displacement produced by force N_0, i.e. in the absence of wave. To comply with zero wave displacements at $t = 0$, the wave form is considered with a formal « ramp function » that equals zero at the initial moment and then gradually reaches 1 :

$$\left\{ \begin{array}{l} u_x = u_x^{Lamb} \cdot r(t) \\ u_y = u_y^{Lamb} \cdot r(t) \\ r(t) = 1 - e^{-(\frac{t}{t_{ramp}})^2}\,. \end{array} \right. \tag{5.19}$$

A formal requirement on the ramp duration $t_{ramp} \gg 1/f$, where f denotes acoustic excitation frequency, guarantees that the distortion introduced by using this technique is negligible.

Due to the presence of the Hertz nonlinearity and of the hysteretic friction force, the equation of motion Eq. (5.17) together with Eq. (5.18) have to be solved numerically. As far as initial problems for ordinary differential equations are concerned, at least two numerical approaches are commonly used : the Runge-Kutta and the Adams-Bashforth [129] methods. The both are precise and efficient enough and assume higher orders of approximation (e.g. 4^{th}, 5^{th}). However, the former one involves expressions to be calculated in between of time discretization points t_j, while the latter one is fully based on calculations at points t_j only. Since the MMD does not directly provide any values in between of time discretization points, the Adams-Bashforth method is more appropriate in that case. Having this in mind, we rewrite the equations (5.17) and (5.16) to be solved in a form suitable for Adams-Bashforth method of the 5th order application :

$$\begin{cases} \frac{\partial y}{\partial t} = y_d \\ \frac{\partial y_d}{\partial t} = \frac{1}{m}(N_0 - N|_{a=y-u_y(t)}) \end{cases} \tag{5.20}$$

in which the first time derivative y_d of the y-coordinate is defined explicitly. The numerical calculations are performed in accordance to the following scheme :

$$\begin{cases} y_{j+5} = y_{j+4} + \mathrm{d}t \sum_{i=0}^{4} k_{i+1} f(t_{j+5-i}, y_{j+5-i}) \\ y_1 = a_0 \,, \end{cases} \tag{5.21}$$

where $k_1 = \frac{1901}{720}$, $k_2 = -\frac{1387}{360}$, $k_3 = \frac{109}{30}$, $k_4 = -\frac{637}{360}$, $k_5 = \frac{251}{720}$, $\mathrm{d}t$ is a time step with $f(t_i, y_i) = 0$ for $i = 1, 2, 3, 4$. The latter equation indicates precompression at the initial moment of time.

Note that for making a new step in time the method requires knowledge of all variables on five previous time steps. This means that for five first steps of the algorithm, some of these previous values are not defined. However, since the procedure starts with zero initial conditions, we assume all such variables to be 0.

Now we know how to calculate forces exerted at HM-CAN from the known Lamb wave-driven displacement. Calculation results for the HM-CAN excited by the Lamb wave obtained via the above method are considered later in section 5.2.3. Here we first concentrate on an analogous description for the RS-CAN.

5.2.2 Rough surface CAN

The obvious difference between the case of real damage and the model HM-CAN is that for real damage no additional mass has to be considered. The only inertial behavior for contact of rough surfaces can be associated with thin layers of material comprising surface roughness that can react on bulk load with some delay. However, the corresponding relaxation time is related to microstructure and is therefore much smaller than the acoustic period and thus is negligible. The quasi-static approximation for the boundary conditions at rough surfaces of real damage remains valid for any acoustic excitation of interest.

In the experiments and simulations for the HM-CAN the ball is prestressed. A real crack can be prestressed either at least due to the following reason. During cracking, an external action is applied that separates crack faces by a distance significantly exceeding the atomic size. Upon releasing the action the crack faces tend to return back to the unstrained state, but due to micro-distortions of local surface shapes they can not do so with the atomic precision. The resulting shapes' mismatch acts as a thin layer of additional material « inserted » between crack faces which actually plays a role of prestress.

Implementing the above considerations, we assume the governing equation in the following form :

$$\begin{cases} a = a_0 - u_y \\ N = Ka^2 \\ x = b + u_x(t) = 0 \\ T = T_{MMD}(b, a)\,, \end{cases} \tag{5.22}$$

where $K = C^2 A_n$, and $C = 6 \cdot 10^{10}\ Pa^{1/2} m^{-1}$ is Biwa's empirical constant.

Here no mass is present so that the equation of motion is replaced by calculation of instantaneous reaction of the contact on the action of the Lamb wave. Displacement a_0 is responsible here for the prestress effect.

A graphical representation for the considered system is given in fig. 5.9a. The no-mass formulation corresponds to a contact between a surface and a small (much less then the wavelength) unmovable block whose coordinate y always stays equal 0 and therefore is not introduced. Certainly, other configurations are possible, but the considered one fully corresponds to Eq. (5.22) and is geometrically similar to the HM-CAN case. Here A_n is the nominal contact area (see section 5.1.1) and C is a constant [113] that can be either estimated from contact microgeometry parameters by using the model discussed in [125] or measured experimentally for a real contact in a way similar to Biwa et al. [113].

5.2.3 Comparison of reactions of both CANs on acoustic excitation

Here it is appropriate to discuss the compliance between the model and real damage CANs. Obviously, the powers in the normal reaction law are not the same in these cases (3/2 and 2). However, by selecting proper parameters, the normal load-displacement curves can be numerically matched. This procedure is required to quantitatively justify relevance of the model defect in the experiment (HM-CAN) as approximation of the real damage (RS-CAN). Also there is an unknown constant A_n in the expression for the force generated by RS-CAN. The choice of this constant is

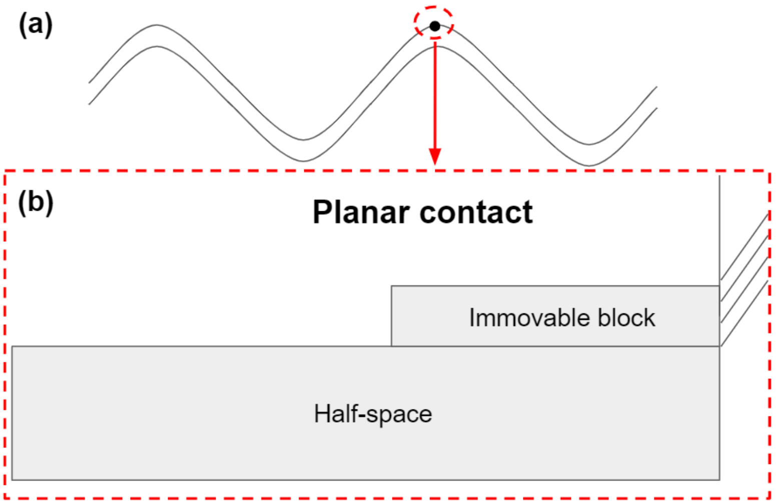

(a) Two rough surfaces in contact exited by the Lamb wave (plate's deformation is highly exaggerated). (b) Zoom on the RS-CAN.

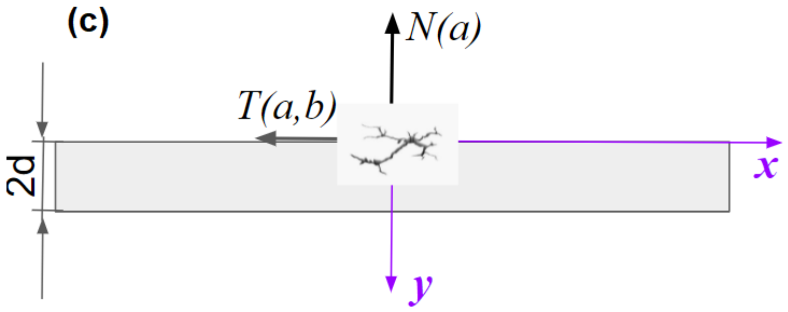

(c) Physical problem formulation for RS-CAN.

FIGURE 5.9 – Model of RS-CAN.

based on the equality of the initial normal displacements a_0 caused by precompression for both HM-CAN and RS-CAN. An example of numerical match between normal reaction in the both models is shown in fig. 5.10 in which the HM-CAN and the RS-CAN responses are observed to be qualitatively similar. The RS-CAN curve is matched to HM-CAN curve with the least squares method. Accepting the value of $C = 6 \cdot 10^{10}\ Pa^{1/2}m^{-1}$ measured by Biwa et al [113] for two aluminum blocks as a reference, we get the radius of nominal contact area $A_n \approx 6.2410^{-9}\ m^2$ that corresponds to the contact size of

$$r_{contact} \approx 4 \cdot 10^{-5}\ m.$$

This means that in both cases the contact size is much less than all macroscopic geometry dimensions and thus can be considered as punctual. Also it is the same order of magnitude as a scattering cross-section detection threshold $\sigma_{th} = 0.065$ mm estimated in section 3.1 of chapter 3. Diameter of the nominal contact area 8 mm is greater than σ_{th}, which confirms that the CAN can be detected.

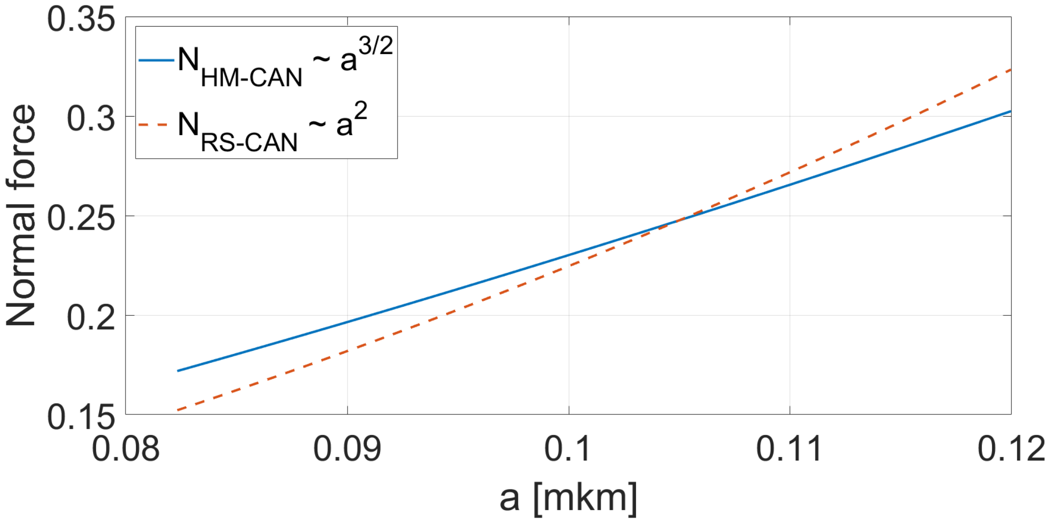

FIGURE 5.10 – The normal load-displacement curve for the HM-CAN and a close curve for RS-CAN with matched parameters for $m^* = 414$.

Despite similar normal responses, the reaction of the considered CANs on the acoustic excitation can be different. The reason is in dynamic effects that arise in the HM-CAN with the finite mass but does not occur in the case of massless RS-CAN.

In figs 5.11 and 5.12 we illustrate cases of various strength of the dynamic effects that consist in appearance of low-frequency modulation of the force response and in a general loss of periodicity with $1/f$ period. In fig. 5.11 they are almost negligible while in fig. 5.12 their magnitude is significant.

It is easy to quantify the expected dynamic effect level by calculating of the dimensionless mass m^* appearing in the dimensionless form of Eqs. (5.17),(5.16), (5.18),(5.19) for the HM-CAN :

Here

$$m^* = \frac{a_0 m f^2}{N_0} \tag{5.23}$$

is a combination of the inverse normal stiffness a_0/N_0 and the known parameter mf^2. To reduce the dynamic effects and make the HM model more adequate to real damage with no inertia, one has to increase the dimensionless mass m^* by increasing the real mass, exciting the plate with a higher frequency, or having a less stiff contact. In figs 5.11 and 5.12, the parameter m^* equals 414 and 155, respectively.

It is also important to mention that increasing prestress decreases overall nonlinearity of the problem. Nevertheless, the secondary waves are generated even for high prestress levels making it possible to detect localized CAN position via methods developed in chapter 2.

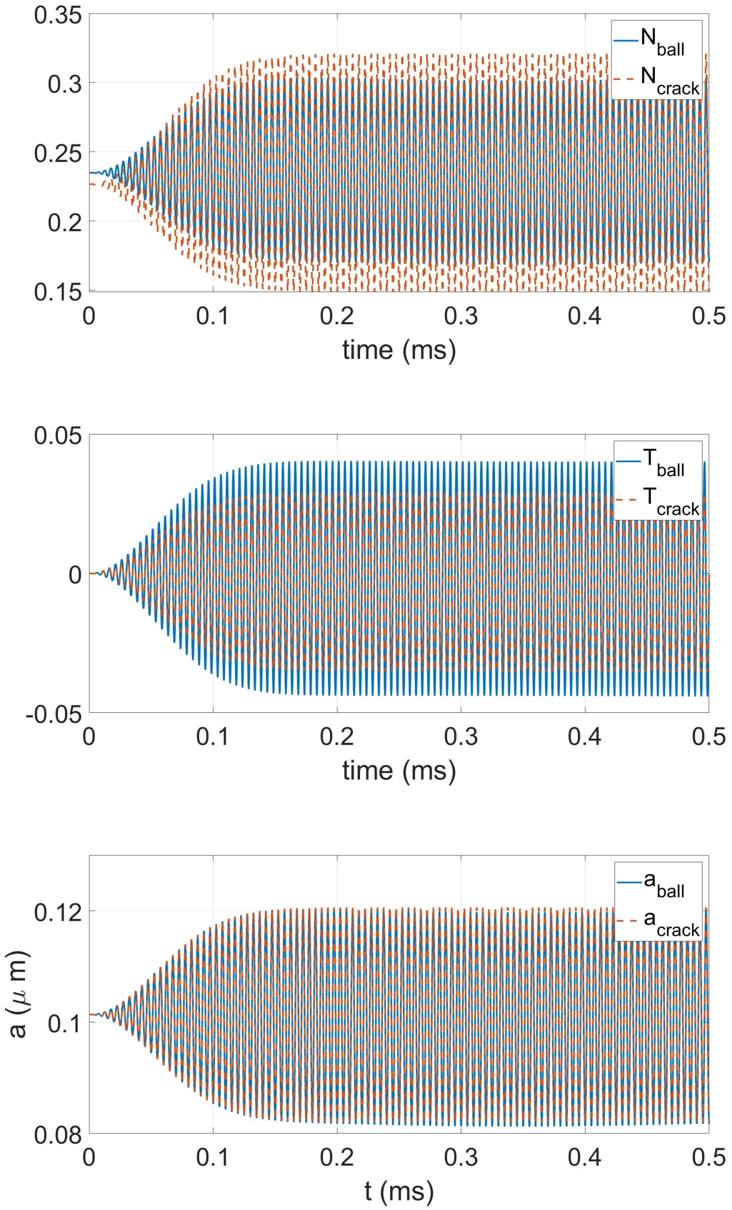

FIGURE 5.11 – Normal (a) and tangential (b) forces applied to the plate by the HM-CAN and RS-CAN with matched normal responses $N(a)$. Here $m^* = 414$ indicating weak dynamic effects. Frequency f=200 kHz, plate thickness $2d$=5 mm, radius of the sphere R=9 mm, no precompression, $B_{amp} = 0.1$ nm.(c) Normal displacement produced by the HM-CAN and RS-CAN with matched normal responses $N(a)$.

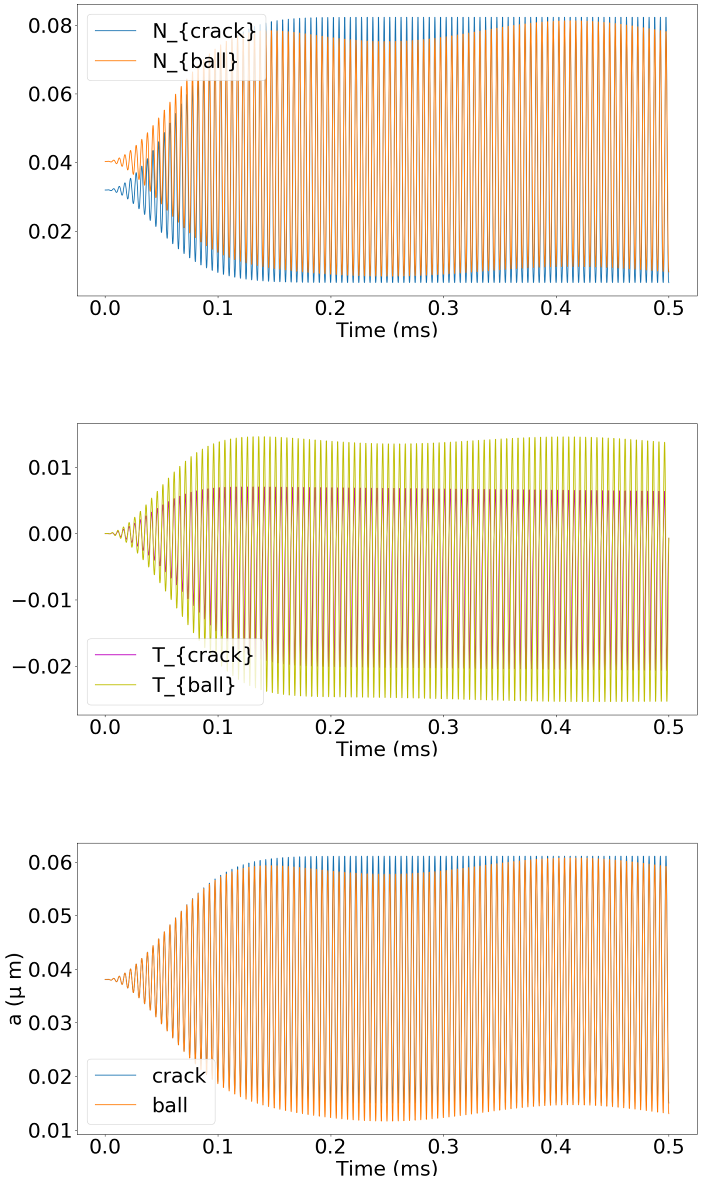

Figure 5.12 – Normal (a) and tangential (b) forces applied to the plate by the HM-CAN and RS-CAN with matched normal responses $N(a)$. Here $m^* = 155$ that corresponds to moderate dynamic effects. Frequency f=200 kHz, plate thickness $2d$=3 mm, radius of the sphere R=5 mm, no precompression, $B_{amp} = 0.15$ nm. This HM-CAN mimics real damage only qualitatively.(c) Normal displacement produced by the HM-CAN and RS-CAN with matched normal responses $N(a)$.

5.3 Numerical modeling for elastic waves interacting with the CAN in a thin plate

5.3.1 Modeling for Lamb waves using finite difference and finite element methods

This section is concerned with modeling for wave propagation in a thin plate in the purpose of calculating the normal and tangential displacements activating the CAN. In the experiments, the first flexural mode A0 is primarily excited whose analytical form is known in the fully harmonics case where $t \in (-\infty, +\infty)$. In practice, some non-stationary transient wave processes are always present at least due to a finite observation time. In addition, the numerical tool to be developed has to be flexible enough in terms of the choice of excitation. These features motivate us to build up a numerical description for the propagating waves, despite the existence of the analytical solution.

In many cases, nowadays numerical modeling for waves in solid structures is based on the finite element method. However, for learning purposes it is interesting to implement the classical finite difference method as well and then compare their efficiencies. Thus, in this section, we set the problem geometry for the both methods and implement the finite element and finite difference solutions in the case corresponding to a pure Lamb mode where the exact solution is known. Then the tested algorithms and codes can be used for modeling any transient wave process when the analytical solution is cumbersome.

Unfortunately, the performance of available computers is not sufficient for an adequate description of real experimental geometry (plate of $L \times w \times 2d$ dimensions suspended on elastic strings). Due to performance limitations we consider a $L \times 2d$ fragment in the 2D case in which geometric parameters L, d, and λ_{Lamb} (Lamb wavelength of A0 mode) are selected in accordance to the following requirements.

First of all, the representative fragment should be long enough to mimic the plate as an object with high geometric aspect ratio, i.e. $L \gg d$, $L \gg \lambda_{Lamb}$. Secondly, the experimental condition of preferential A0 mode excitation engenders a requirement in terms of the λ_{Lamb} and the plate half-thickness d. Indeed, the theoretical number of the antisymmetric Lamb modes that can travel in a plate of a certain thickness is given by Eq. (1.1) [19], therefore, if $[\frac{2d}{\lambda_{Lamb}}] = 0$, then $N_a = 1$, namely, only A0 mode is present.

These requirements are satisfied by selection of the following excitation and geometric parameters : $d = 2.5$ mm, $f = 200$ kHz, $L = 5\lambda_{Lamb} \approx 5$ cm. The $\lambda_{Lamb} = \frac{2\pi}{k_{A0}}$, where wavenumber k_{A0} is to be determined in an implicit way as a root of an algebraic equation (1.2) or equivalently :

$$\begin{aligned} &f(k) = (2k^2 - k_t^2)^2 \sinh\sqrt{(k^2 - k_l^2)}d \cosh\sqrt{k^2 - k_t^2}d \\ &-4k^2\sqrt{(k^2 - k_l^2)}\sqrt{(k^2 - k_t^2)} \cosh\sqrt{(k^2 - k_l^2)}d \sinh\sqrt{(k^2 - k_t^2)}d = 0 \end{aligned} \tag{5.24}$$

that is convenient to solve by a bisection method i.e. by repeatedly dividing the interval containing the root. Indeed, taking an initial interval $k_{A0} \in [1, 50000]$ m^{-1} ($f(1)$ is positive while $f(50000)$ is negative), after 100 bisections only we localize the root $k_{A0} = 540.1073572879936$ m^{-1} with the precision of 10^{-13} m^{-1}.

After locating the root corresponding to the Lamb wavelength, we proceed to numerical solving of the following wave propagation problem :

$$\begin{cases} \frac{\partial v_x}{\partial t} = \frac{1}{\rho}(\frac{\partial \sigma_{xx}}{\partial x} + \frac{\partial \sigma_{xy}}{\partial y}) \\ \frac{\partial v_y}{\partial t} = \frac{1}{\rho}(\frac{\partial \sigma_{xy}}{\partial x} + \frac{\partial \sigma_{yy}}{\partial y}) \\ \frac{\partial \sigma_{xx}}{\partial t} = (\lambda + 2\mu)\frac{\partial v_x}{\partial x} + \lambda\frac{\partial v_y}{\partial y} \\ \frac{\partial \sigma_{yy}}{\partial t} = (\lambda + 2\mu)\frac{\partial v_y}{\partial y} + \lambda\frac{\partial v_x}{\partial x} \\ \frac{\partial \sigma_{xy}}{\partial t} = \mu(\frac{\partial v_x}{\partial y} + \frac{\partial v_y}{\partial x}) . \end{cases} \tag{5.25}$$

In this equations (v_x,v_y) is the 2D-velocity vector, $(\sigma_{xx},\sigma_{yy},\sigma_{xy})$ is the stress tensor, λ and μ are Lamé coefficients. L is the plate length, d is a half of the plate's thickness.

Equation (5.25) describes the A0 Lamb wave if supplemented by the initial conditions in the form

$$\begin{cases} v_x(t = 0) = v_x^{Lamb}(t = 0) \\ v_y(t = 0) = v_y^{Lamb}(t = 0) \\ \sigma_{xx}(t = 0) = \sigma_{xx}^{Lamb}(t = 0) \\ \sigma_{yy}(t = 0) = \sigma_{yy}^{Lamb}(t = 0) \\ \sigma_{xy}(t = 0) = \sigma_{xy}^{Lamb}(t = 0) \end{cases} \tag{5.26}$$

and the boundary conditions

$$\begin{cases} \sigma_{yy}(x = 0) = \sigma_{yy}^{Lamb}(x = 0) \\ v_x(x = 0) = v_x^{Lamb}(x = 0) \end{cases} \tag{5.27}$$

and

$$\begin{cases} \sigma_{yy}(x=L) = \sigma_{yy}^{Lamb}(x=L) \\ v_x(x=L) = v_x^{Lamb}(x=L) \end{cases} \tag{5.28}$$

at the left and right edges of the plate. The boundary conditions at the top and bottom faces are stress-free and are given by

$$\begin{cases} \sigma_{xy}(y=\pm d) = 0 \\ \sigma_{yy}(y=\pm d) = 0\,. \end{cases} \tag{5.29}$$

Here variables with the superscript « Lamb » defined in Eqs. (1.3), (1.4), (1.5) correspond to the analytical solution for the A0 Lamb wave. It is straightforward to check that the solution in Eqs. (1.3), (1.4), (1.5) exactly satisfies the above equation Eq. (5.25). The geometry together with boundary conditions are illustrated in fig. 5.13.

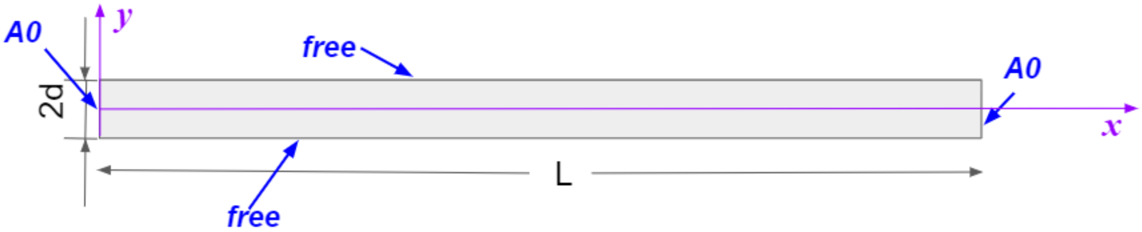

FIGURE 5.13 – Geometry and boundary conditions corresponding to the A0 Lamb mode in a thin plate.

a) Finite difference formulation

In the finite difference method, the derivatives in Eq. (5.25) are to be substituted with finite differences. They can be one-sided or centered which corresponds to the first or second order of approximation, respectively. The choice of the latter case results in a staggered grid formulation [130] in which some variables are defined at odd grid nodes while the others are defined at the even ones. This scheme is illustrated in fig. 5.14.

In particular, v_x is defined only on even y-layers and odd x-layers, v_y - on odd y-layers and even x-layers, σ_{xx} and σ_{yy} - on even y-layers and even x-layers, and σ_{xy} - on odd y-layers and odd x-layers. In fig. 5.14 time stepping is shown for v_x and

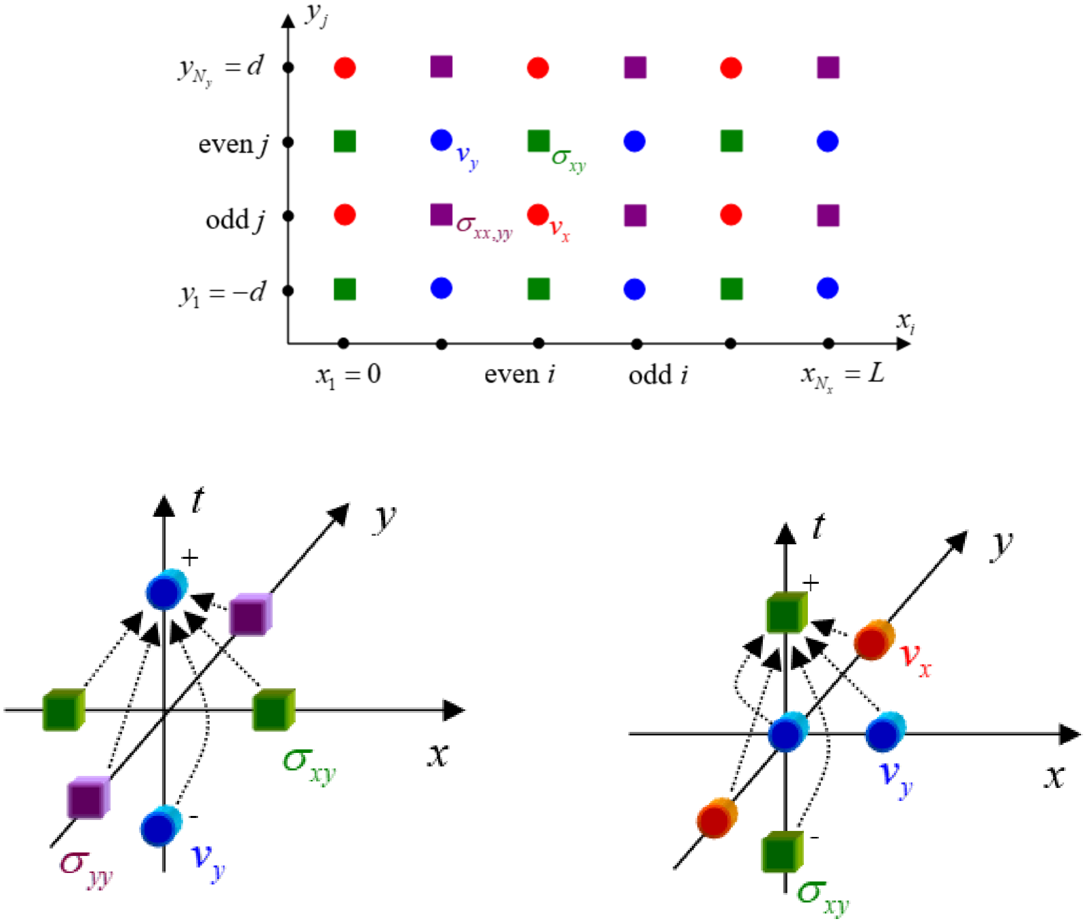

FIGURE 5.14 – Staggered grid formulation of the finite difference method for Eq. (5.25). (a) Each spacial layer contains nodes with odd and even numbers at which different variables are defined. (b) Examples of time stepping to the new time layer (variables marked with « + ») from the current one (unmarked variables) and the previous one (marked with « - »).

σ_{xy}. For other variables the procedure is analogous. Here label « + » stands for new time layer, label « - » is for the previous one.

Introducing the grids x_i, y_j, t_l in space and in time via expressions :

$$\begin{cases} x_i = (i-1)\Delta x \\ y_j = -d + (j-1)\Delta y \\ t_l = (l-1)\Delta t \end{cases}$$

with $i = 1, .., N_x$, $j = 1, .., N_y$, $l = 1, .., N_t$ and steps :

$$\begin{cases} \Delta x = \dfrac{L}{N_x - 1} \\ \Delta y = \dfrac{2d}{N_y - 1} \\ \Delta t = \dfrac{T_{comp}}{N_t - 1}, \end{cases}$$

we denote variables on this grid as $v_x(i,j)$, $v_y(i,j)$ for x- and y- velocity components respectively, $\sigma_{xx}(i,j)$, $\sigma_{xy}(i,j)$, $\sigma_{yy}(i,j)$ for stress tensor components. T_{comp} here stands for computation time.

Using the above scheme of time stepping, it is easy to write the corresponding discretized equations which take the form :

$$\begin{cases} v_x(i,j)^+ = v_x(i,j)^- + \frac{\Delta t}{\rho\Delta x}(\sigma_{xx}(i+1,j) - \sigma_{xx}(i-1,j)) + \frac{\Delta t}{\rho\Delta y}(\sigma_{xy}(i,j+1) - \sigma_x y(i,j-1)) \\ v_y(i,j)^+ = v_y(i,j)^- + \frac{\Delta t}{\rho\Delta x}(\sigma_{xy}(i+1,j) - \sigma_{xy}(i-1,j)) + \frac{\Delta t}{\rho\Delta y}(\sigma_{yy}(i,j+1) - \sigma_{yy}(i,j-1)) \\ \sigma_{xx}(i,j)^+ = \sigma_{xx}(i,j)^- + (\lambda+2\mu)\frac{\Delta t}{\Delta x}(v_x(i+1,j) - v_x(i-1,j)) + \lambda\frac{\Delta t}{\Delta y}(v_y(i,j+1) - v_y(i,j-1)) \\ \sigma_{yy}(i,j)^+ = \sigma_{yy}(i,j)^- + (\lambda+2\mu)\frac{\Delta t}{\Delta y}(v_y(i,j+1) - v_y(i,j-1)) + \lambda\frac{\Delta t}{\Delta x}(v_x(i+1,j) - v_x(i-1,j)) \\ \sigma_{xy}(i,j)^+ = \sigma_{xy}(i,j)^- + \mu\frac{\Delta t}{\Delta y}(v_x(i,j+1) - v_x(i,j-1)) + \mu\frac{\Delta t}{\Delta x}(v_y(i+1,j) - v_y(i-1,j))\,. \end{cases}$$

To represent the boundary conditions, it is convenient to take odd total numbers of points N_x and N_y. This selection fully corresponds to the boundary conditions(5.27),(5.28) at the plate edges written here in the form :

$$\begin{cases} \sigma_{xy}(1,j) = \sigma_{xy}^{Lamb}(x_1, y_j, t_l) \\ v_x(1,j) = v_x^{Lamb}(x_1, y_j, t_l) \\ \sigma_{xy}(N_x,j) = \sigma_{xy}^{Lamb}(x_{N_x}, y_j, t_l) \\ v_x(N_x,j) = v_x^{Lamb}(x_{N_x}, y_j, t_l)\,. \end{cases} \tag{5.30}$$

The stress-free boundary conditions (5.29) at the plate top and bottom surfaces should be replaced by the ones conforming to the staggered grid formulation :

$$\begin{cases} v_y(i,1)^+ = v_y(i,1)^- + \frac{2\Delta t}{\rho \Delta y}\sigma_y y(i,2) \\ \sigma_x y(i,1) = 0 \\ v_y(i,N_y)^+ = v_y(i,N_y)^- - \frac{2\Delta t}{\rho \Delta y}\sigma_{yy}(i,N_y-1) \\ \sigma_{xy}(i,N_y) = 0\,. \end{cases} \tag{5.31}$$

The initial conditions on the staggered grid read :

At $t = 0$:

$$\begin{cases} v_x(i,j)^- = v_x^{Lamb}(x_i,y_j,0) \\ v_y(i,j)^- = v_y^{Lamb}(x_i,y_j,0) \\ \sigma_{xx}(i,j)^- = \sigma_{xx}^{Lamb}(x_i,y_j,0) \\ \sigma_{xy}(i,j)^- = \sigma_{xy}^{Lamb}(x_i,y_j,0) \\ \sigma_{yy}(i,j)^- = \sigma_{yy}^{Lamb}(x_i,y_j,0) \end{cases} \tag{5.32}$$

At $t = \Delta t$:

$$\begin{cases} v_x(i,j) = v_x^{Lamb}(x_i,y_j,\Delta t) \\ v_y(i,j) = v_y^{Lamb}(x_i,y_j,\Delta t) \\ \sigma_{xx}(i,j) = \sigma_{xx}^{Lamb}(x_i,y_j,\Delta t) \\ \sigma_{xy}(i,j) = \sigma_{xy}^{Lamb}(x_i,y_j,\Delta t) \\ \sigma_{yy}(i,j) = \sigma_{yy}^{Lamb}(x_i,y_j,\Delta t)\,. \end{cases} \tag{5.33}$$

The considered time stepping is explicit i.e. each value at the text time step is obtained independently, in contract to implicit schemes in which they are coupled so that an additional equation should be solved. For explicit schemes, the Courant-Friedrichs-Lewy [131] conditions should be required :

$$c_{Lamb}\Delta t < \sqrt{(\Delta x^2 + \Delta y^2)}\,, \tag{5.34}$$

where $c_{Lamb} = \frac{\omega}{k_{A0}}$.

The comparison of the numerical solution via finite differences with the exact one will be done later. Now we turn to modeling for Lamb wave propagation using the finite element method.

b) Finite element solution

The finite element solution is performed with the help of a standard commercial package COMSOL Multiphysics that uses two second-order equations for the displacement components instead of Eq. (5.25) :

$$\begin{cases} \rho\frac{\partial^2 u_x}{\partial t^2} = (\lambda+\mu)\frac{\partial^2 u_x}{\partial x^2} + \frac{\partial^2 u_x}{\partial x \partial y} + \mu\frac{\partial^2 u_x}{\partial y^2} \\ \rho\frac{\partial^2 u_y}{\partial t^2} = (\lambda+\mu)\frac{\partial^2 u_y}{\partial x^2} + \frac{\partial^2 u_y}{\partial x \partial y} + \mu\frac{\partial^2 u_y}{\partial y^2}\,. \end{cases} \tag{5.35}$$

The package accepts boundary conditions formulated in terms of displacements such as

$$\begin{cases} u_x(x=0) = u_x^{Lamb}(x=0,y,t) \\ u_y(x=0) = u_y^{Lamb}(x=0,y,t) \\ u_x(x=L) = u_x^{Lamb}(x=L,y,t=0) \\ u_y(x=L) = u_y^{Lamb}(x=L,y,t=0)\,, \end{cases} \tag{5.36}$$

as well as stress-free boundary conditions as in Eq. (5.29).

The initial conditions are specified at $t = 0$ in the usual form for displacements and velocities :

$$\begin{cases} u_x(t=0) = u_x^{Lamb}(x,y,t=0) \\ u_y(t=0) = u_y^{Lamb}(x,y,t=0) \\ \frac{\partial u_x}{\partial t} = v_x^{Lamb}(x,y,t=0) \\ \frac{\partial u_y}{\partial t} = v_y^{Lamb}(x,y,t=0)\,. \end{cases} \tag{5.37}$$

The code automatically meshes the calculation domain using triangular elements (in our case) and uses a built-in solver to get all acoustic fields in the domain at any moment of time. The details are given in the following paragraph in which the comparison with the finite difference solution is discussed.

c) Stationary Lamb wave simulated via the finite difference and finite element methods

In this section, we make a comparison between the finite difference and finite element methods in terms of performance. This comparison is possible due to the existence of the exact solution Eq. (1.3) for the A0 Lamb mode. The deviation between the exact solution and the numerical ones expressed as a normalized root mean square (rms) error is an obvious performance measure for the both methods. To be more specific, the performance is a definite error magnitude achieved during certain time of calculation on the same computer.

There is, however, a technical difficulty associated with the fact that the both methods include discretization in space and in time, and the most efficient ratio between space and time discretization steps is *a priori* unknown. Indeed, finer space mesh and smaller time step usually both have positive effect on the calculation error but are related to higher calculation times. This aspect deserves an additional optimization.

To do so, the following simple technique can be used. We use different but fixed spatial meshes for the both methods and perform a series of computations for different time steps keeping other parameters unchanged. First we start with a very coarse time stepping and gradually increase the time discretization quality. In finite element computing, the calculation error immediately drops as long as the time step decreases, then the gain becomes smaller and finally almost disappears for very fine time grids. In this final situation the quality of numerical solution is mostly affected by the quality of space meshing. The optimal performance is obtained when the gain from refining the time grid starts saturating. A better estimation can be obtained by varying both space and time discretizations.

However, the opposite effect can occur when explicit finite difference calculations are used. A key feature in this case is the presence of Courant-Friedrichs-Lewy condition [131]

$$CFL \equiv \frac{|c|\Delta t}{\Delta x} < 1 \tag{5.38}$$

that determines the stability of calculations. Here c is the velocity, Δx and Δt are spatial and time steps, respectively. In other words, setting too large time step engenders error accumulation during subsequent time steps. A simple Von Neumann stability analysis of wave equation [132] shows that calculations are most precise when the condition Eq. (5.38) is just fulfilled ; the precision worsens when CFL is considerably less than 1.

It is instructive to cite these arguments here for completeness. For the simplest 1D wave equation

$$\frac{1}{c^2}\frac{\partial^2 u}{\partial t^2} = \frac{\partial^2 u}{\partial x^2} \tag{5.39}$$

the corresponding wave dispersion relationship is obtained by substituting $u = u_0 e^{i(\omega t - kx)}$ into Eq. (5.39)

$$-\frac{\omega^2}{c^2} u_0 e^{i(\omega t - kx)} = -k^2 u_0 e^{i(\omega t - kx)}$$

with the obvious result $k = \pm\frac{\omega}{c}$. The same harmonic solution substituted to the discretized equation

$$\frac{1}{c^2}\frac{u_j^+ - 2u_j + u_j^-}{\Delta t^2} = \frac{u_{j+1} - 2u_j + u_{j-1}}{\Delta x^2} \tag{5.40}$$

or substituting $u_j = u_0 e^{i(\omega t - kj\Delta x)}$ into Eq. (5.40) leads to another result :

$$\frac{\cos(\omega\Delta t) - 1}{c^2\Delta t^2} = \frac{\cos(k\Delta x) - 1}{\Delta x^2} \,. \tag{5.41}$$

(a) Finite difference method

time step, ns	3	2.9	2.5	1.7	1.25	1	0.8

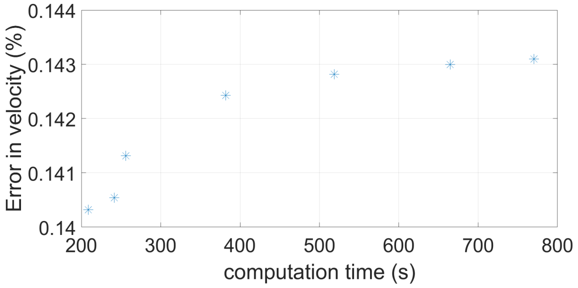

(b) Finite element method

time step, ns	62.5	50	41.7	35.7	31.25	27.8	25	22.7	20.8	19.2	17.9	16.7	15.6	14.7	13.9	13.16	12.5

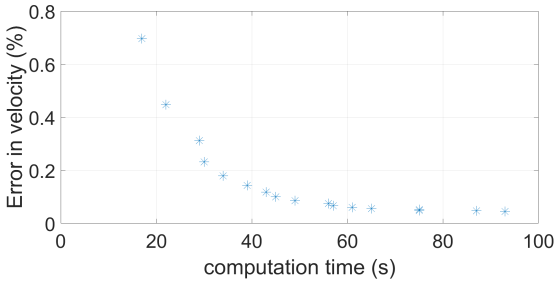

FIGURE 5.15 – Rms error of finite difference (a) and finite elements (b) method comparing to analytical solution for different time meshes as a function of computation time.

It is straightforward to check that the dispersion relationship Eq. (5.41) exactly corresponds to $k = \frac{\omega}{c}$ for

$$\Delta x = c\Delta t \tag{5.42}$$

and is different otherwise. The condition Eq. (5.42) requires that the parameter CFL be close to 1 i.e. the explicit finite difference scheme works best at the stability threshold. In other words, refining time discretization while keeping Δx constant is useless in this case. The calculation error can be decreased by simultaneous reducing Δt and Δx that obviously improve approximation of the finite difference scheme.

Fig. 5.15 illustrates the predicted effects and gives an idea on the comparative performance of the finite element and finite difference methods. The latter one is implemented in Fortran and Matlab having in this case a relative performance factor of 2.7 (Fortran wins).

Whilst Matlab finite differences realization and COMSOL finite element code show comparable performances, the finite element method is undoubtedly gains in terms of geometric flexibility. This feature underlies our decision to use the finite element method for further calculations.

5.3.2 Secondary waves generated by contact acoustic nonlinearity in a thin plate

This section is concerned with the propagation problem for secondary waves excited by the CAN that plays a role of a punctual force source. The geometry of the problem is same as for primary Lamb waves in the section 5.3.1 and is illustrated in fig. 5.16. A substantial difference is related to the boundary conditions. In the primary wave propagation problem, the boundary conditions corresponded to the exact Lamb solution. Since they are already satisfied, the conditions at the plate edges

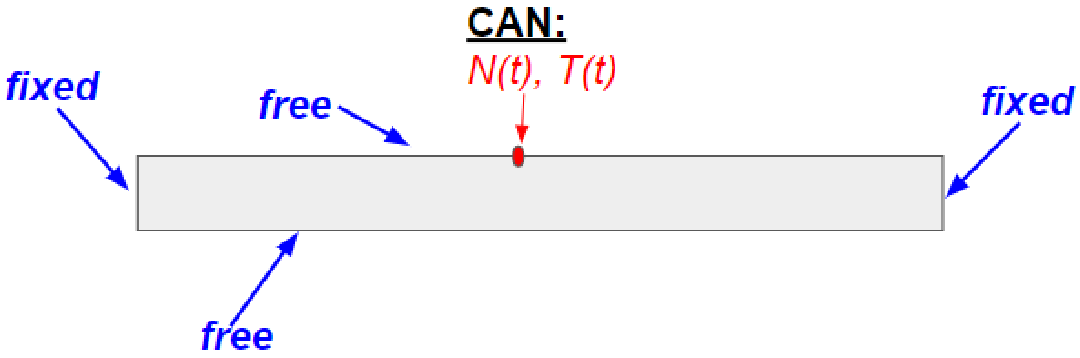

FIGURE 5.16 – Geometry of the secondary wave generation problem. The CAN is excited by the displacements obtained in section 5.3.1 and now, in turn, generates secondary waves via application of nonlinear punctual forces $N(t)$ and $T(t)$ calculated as explained in section 5.2.

for the secondary wave problem represent zero displacements (fixed boundaries). In our example, this formulation helps avoid activating the movement of the plate as a whole. Such movement would occur in a situation when the plate is excited by stresses or velocities without fixing displacements at least at some point of the boundary. In reality, the plate is suspended with elastic strings which are not considered in the present numerical model.

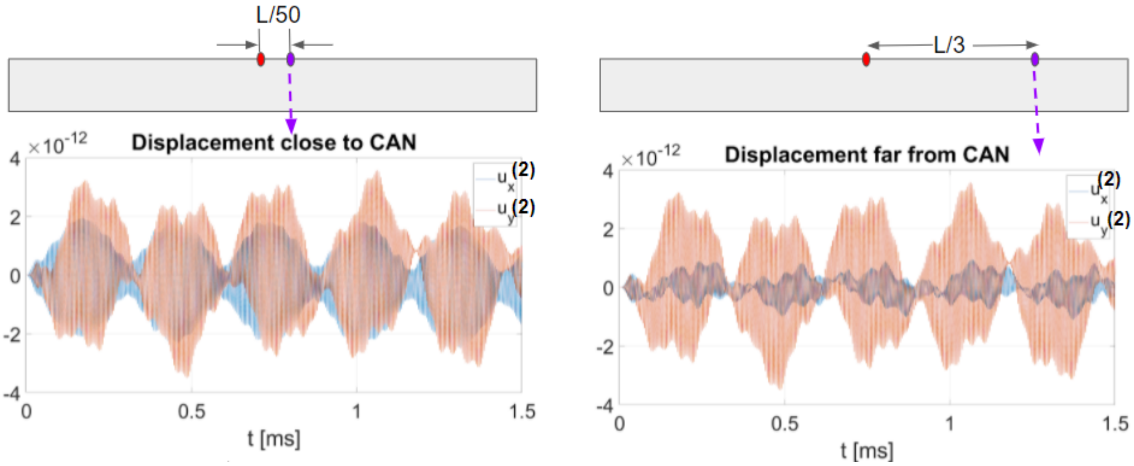

FIGURE 5.17 – Secondary waves emitted by Hertz-Mindlin CAN in a thin plate.

A typical profile of the secondary wave excited by forces depicted in fig. 5.11 is shown in fig. 5.17. To see more features in the secondary wave, we have considered a long sequence of the force excursions comprising 300 periods of the primary Lamb wave (cf. 100 periods in fig. 5.11 for the forces). It can be immediately noticed that a quasi-periodic force protocol excites a long series of reverberations from the edges of the small plate fragment (fig. 5.17). The multiply reflected wave interferes with itself producing a complex non-periodic signal. Besides the fundamental frequency imposed by the primary Lamb mode, it contains higher harmonics as well as low-frequency modulations. The character of the signal is determined by the fact that the secondary wave generation is asymmetric even though the secondary source is located exactly at the middle of the plate.

In practice, the damage localization algorithm deals with first arrivals rather than reverberated waves. Certainly, the complexity of the process shown in fig. 5.17 is due to multiple reverberations in the considered confined geometry that is usually avoided in real measurements (chapter 2). However, physical nature of the underlying processes remains the same and corresponds to the interaction between acoustic waves and a frictional contact.

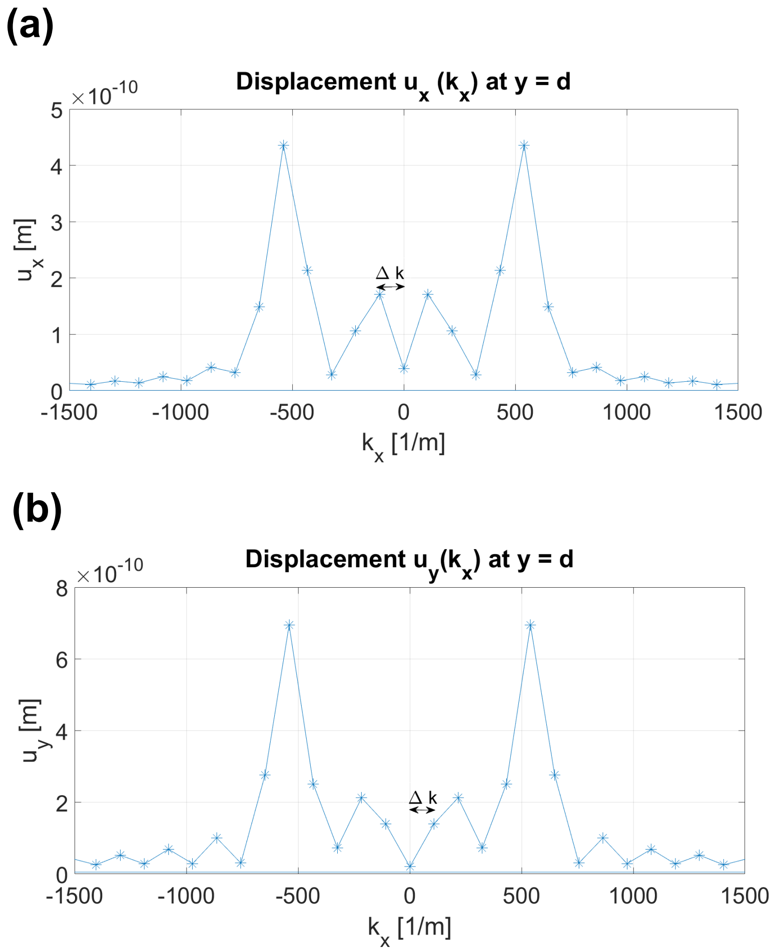

FIGURE 5.18 – Spatial Fourier analysis of secondary waves : displacement (a) u_x and (b) u_y as functions of wavenumber k_x on the top surface of the plate containing the contact acoustic nonlinearity. The dominant component is A0 Lamb wave ($k_x \approx 540.1$ 1/m) that the plate was excited with.

In the considered example, the secondary wave is about 10^{-4} times weaker in amplitude than the primary one. It is important to stress that even such a weak magnitude of the secondary signal is sufficient for successful damage locating in experiments.

It would be instructive to see the structure of spatial spectrum of secondary waves given at a certain (last) moment of time. The result of the 1D spatial Fourier transform as a function of spatial frequency k_x corresponding to x-coordinate on the top surface is depicted in fig. 5.18. A0 Lamb wave with $k = k_{A0} \approx 540$ 1/m remains dominant in the secondary wave spectrum. Peak of A0 mode has finite width, at least because the signal is limited in space by the plate boundaries. $A0$ is the slowest Lamb mode, which implies the largest wavenumber k_{A0}, as confirmed in fig. 5.18. There are also other spatial frequencies in the spectrum with $k < k_{A0}$. In contrast to the primary A0 mode selectively excited in our numerical modeling, these modes are generated altogether in a non-selective way. Note that the spatial frequency step Δk equals $\frac{\pi}{L}$ and can not be reduced without changing the plate length. This factor does not allow to see the spectral structure of these modes in detail.

5.3.3 Prototype of numerical tool accompanying SHM experiments for detecting damage in thin plates

As it was mentioned, there exists a substantial difference in geometric parameters between the simplified case described via the developed modeling tool and real SHM experiments in thin plates. Due to this reason, the developed tool can be seen as a prototype for a future more advanced numerical toolbox capable of imitating realistic secondary waves emitted by damage that contain information for damage locating algorithms. However, the principal stages of the modeling procedure are similar for the prototype and for a prospective working toolbox. The prototype tool comprises the following five steps.

1. Generation of stationary A0 Lamb wave or of a transitional wave process at a certain frequency in a fragment of a thin plate. This algorithm is implemented using COMSOL Multiphysics ; data for the normal $u_y(t)$ and tangential $u_x(t)$ displacement wave components are exported at a point corresponding to the defect location.

2. Displacement time data previously obtained on a relatively coarse grid suitable for solving time-consuming wave equation are interpolated on a finer grid for solving ordinary differential equations describing the CAN behavior at the next step.

3. The equation of motion in ordinary derivatives for a HM-CAN excited by wave displacements is numerically solved using the Adams-Bashforth algorithm in the purpose of obtaining the normal $N(t)$ and tangential $T(t)$ contact forces applied to the plate at the defect position. In the case of RS-CAN, these forces are calculated directly from the known contact displacements $a(t)$ and $b(t)$ without solving of equation of motion. In the both situations, the load-displacement relationships for frictional contact are obtained with the use of the Method of Memory Diagrams. The corresponding algorithms are implemented in Fortran.

4. Technical step consisting in preparation of force data for importing to COMSOL at the next stage.

5. Solving the problem for secondary waves emitted by a punctual force with the normal $N(t)$ and tangential $T(t)$ components applied at the defect position (programmed in COMSOL). Same geometry as at step 1 is considered.

Conclusions

The principal result of the modeling effort presented in this chapter is the creation of a modeling tool capable of describing the dynamic CAN response to acoustic excitation and the subsequent generation of the secondary waves to be used in SHM damage locating procedures. The contact response is modeled here with the use of modern semi-analytical approaches based on the Hertz-Mindlin contact theory which takes into account friction and friction-induced hysteresis. Thus, in some sense, the proposed model bridges the gap between acoustics and contact mechanics and provides a description for processes underlying NDT/SHM experiments in acoustically excited structures containing inner frictional contacts.

At the same time, the developed numerical tool should be seen as a prototype of a real working toolbox that has to accompany SHM experiments in the future. The reason for that is in a considerable number of geometric simplifications accepted in the analysis. In particular, instead of realistic damaged plate-like structures we have considered a 2D small fragment of a plate interacting with an artificial CAN (such as small sphere pressed against the plate similar to the one in real experiments in chapter 2). On the one hand, the presence of inertia associated with the sphere make the response dynamic which is not pertinent to crack-like defects having no mass. On the other hand, the plate fragment is assumed to have fixed edges to avoid the movement of the plate as a whole. These boundary conditions entail multiple reflections of the secondary wave incompatible with the use of the damage locating algorithms (chapter 2). However, despite these features following from experimental or modeling simplifications, physical nature of the considered processes is represented in an adequate manner.

In particular, we have arrived to the following specific conclusions.

1. There exist physical conditions under which the model CAN (sphere-plate contact or HM-CAN) behaves similarly to crack-like damage (RS-CAN) in terms of mechanical response to acoustic excitation. Namely, the dimensionless mass introduced in Eq. (5.23) must be much higher than 1. Higher dimensionless mass provides the similarity between the both responses at a longer time interval.

2. The developed numerical tool adequately describes physical nature of the CAN-wave interaction, but the considered test geometry significantly differs from the experimental one.

3. Modern FEM-based software provide generally higher but comparable efficiency with respect to the classical finite difference implementations.

This study can be substantially improved in the future ; the related perspectives include :

1. Account for geometries closer to real SHM experiments (higher geometric aspect ratios of the computation domain, realistic suspensions/fixing of the tested structure, excitation signals similar to the applied pump-probe scheme, etc). These improvements would require significantly higher computation resources.

2. Parameters of the used CAN models can be matched to behaviors of real defects.

3. Mutual compromises from both modeling and experimental sides can help reach a configuration which, on the one hand, assumes the application of the damage locating algorithms and visualizing damage, and, on the other hand, adequate modeling is possible. This effort would result in establishing a detailed theory and experiment agreement in NDT/SHM problems.

4. 3D-modeling can bring the model closer to the current experimental configuration and open the opportunity to numerically estimate the damage scattering cross-section, as well as to establish its dependence on CAN mechanical properties. Indeed, in 3D it is possible to do by analyzing secondary waves generated by a CAN. However, this change would require higher computer performance.

General conclusions and perspectives

As mentioned in introduction, the main goal of this thesis was to develop ambient noise based reference-free acoustic damage localization technique for structural health monitoring in thin plates capable of identifying contact acoustic nonlinearities modulated by low frequency vibrations. In this work, we particularly focused on the experimental tests with an artificial CAN in pump-probe configuration. We studied scattering characteristics of this artificial CAN and performed modeling for its nonlinear interaction with acoustic waves in a thin aluminum plate. Preliminary localization results have been obtained in experiments with white noise of kHz range along with low frequency harmonic vibrations. Image contrast increases with the growth of the defect scattering cross-section. Strain induced by pump wave is proportional to vertical displacement, i.e. it is mechanically linear regime. Strain caused by the probe wave appeared to be three orders of magnitude smaller than strain caused by pump wave.

In chapter 2, an active reference-free damage localization algorithm in thin plates based on a combination of repetitive probing with back-propagation of signals is described. This algorithm appeared to be capable of detecting an artificial CAN mimicked with a steel sphere pressed against an aluminum plate in pump-probe experiments. The algorithm's working range is at few Hertz for pump wave and at tens kHz for probe wave. Two variants of experiment have been done : when a pump wave is synchronized with a probe wave (synchronized mode) and when it is not (non-synchronized mode). For non-synchronized experiments, random sign compensation technique was proposed to improve contrast of localization images. Contrast was improved by up to 15 times comparing to incoherent imaging of the initial algorithm. Derivation of formula for a contrast established relationship with a CAN scattering cross-section. For synchronized experiments, coherent imaging based on classical synchronous detection was introduced. Contrast was improved by 3 to 5 times comparing to incoherent imaging of the initial algorithm. The proposed algorithm is robust for various emitter positions. The closer the emitter to the defect and to the center of the plate, the better localization image is obtained. The algorithm functions for different defect locations including situations when it is close to plate's boundaries. The parameters (probe and pump frequencies, emitter position) for high contrast images have been empirically optimized. Strain caused by probe wave $\sim 10^{-8}$, which is three orders lower than for pump wave. Strain induced by pump wave is proportional to displacement, i.e. our experiment remains in linear regime. Nonlinearity of experiment is not in stress-strain dependency but essentially in pump-probe interaction with a CAN.

Chapter 3 provides quantitative study of an artificial CAN scattering characteristics and image contrast in the experiment described in chapter 2. It is shown that the contrast depends monotonically on a defect scattering cross-section, and is directly proportional to it at small scattering cross-sections. This statement has been confirmed by experimental measurements, numerical simulation of scattering in infinite plate and theoretical derivation for active static experiments. Scattering cross-section of an artificial CAN is experimentally estimated under infinite plate approximation and isotropic scatterer assumption for the central excitation frequency. CAN with scattering cross-section from the order of hundredths of a millimeter to several millimeters can be resolved by the proposed localization algorithm. In pump-probe experiment, image contrast can be improved by increasing pump amplitude or changing the defect strength, i.e. angle between ruler and the plate. Number of receivers and sources also affect image contrast according to the obtained theoretical formula.

In the fourth chapter preliminary passive experiments are discussed which constitutes a proof of concept of passive SHM in environment subjected to low frequency vibrations. Algorithm developed in chapter 2 is applied for pump-probe experiment with white noise from 1 to 30 kHz as a probe wave. Relative noise level is estimated for the preliminary passive experiment with unsuccessful detection, the conclusion from that was to increase number of noise sources, which is done in the next chapter about passive dynamic experiments. Differential signals are replaced with differential correlations of short windows and are subjected to back-propagation procedure and coherent summation. Dependencies of image contrast on the window duration, number of receivers and noise sources, sources distribution are qualitatively studied.

Preliminary localization images are obtained. Interaction between an artificial CAN with white noise is weak compared to residual noise, therefore, the algorithm is sensitive to many parameters and in the current setup configuration is hard to be detected. Further developments are suggested to decrease relative noise level by optimizing noise sources and receivers distribution, modifying technique of summation over loading states, conducting tests on larger plate.

The principal result of chapter 5 is the development of a modeling tool capable of describing the dynamic CAN response to acoustic excitation and the subsequent generation of the secondary waves to be used in SHM damage locating procedures. Hertz-Mindlin contact response to acoustic wave is compared to a crack response. First, semi-analytical algorithm accounting for friction was used to obtain force-displacement relationship at the contact for both sphere pressed against the plate (Hertz-Mindlin contact) and crack (planar contact model) in a thin plate excited by Lamb A0 mode. Then these forces were applied as a point load on the plate top surface and resulting acoustic field was measured by solving wave equation with a finite element method. An artificial model CAN can be approximated by a crack under particular physical conditions, namely, prestress, Lamb waves amplitude and frequency, plate's thickness, and mass of the sphere. The developed numerical tool adequately describes physical nature of the CAN-wave interaction, but the considered test geometry significantly differs from the experimental one.

In perspective, geometries closer to real SHM experiments can be considered (higher geometric aspect ratios of the computation domain, realistic suspensions/fixing of the tested structure, excitation signals similar to the applied pump-probe scheme, etc). These improvements would require significantly higher computation resources. Parameters of the used CAN models can be matched to behaviors of real defects. Mutual compromises from both modeling and experimental sides can help reach a configuration which, on the one hand, assumes the application of the damage locating algorithms and visualizing damage, and, on the other hand, adequate modeling is possible. 3D-modeling can bring the model closer to the current experimental configuration and open the opportunity to numerically estimate the damage scattering cross-section, as well as to establish its dependence on CAN mechanical properties. However, this change would require higher computer performance. These efforts would result in establishing a detailed theory and experiment agreement in NDT/SHM problems.

We envisage to extend this method to a more realistic situation with using the secondary noise sources (see fig. 5.19) developed by G. Lacerra, F. Massi, E. Chatelet (our project partners in LaMCoS, Lyon) [133] to convert a part of low-frequency plate modal vibrations into high-frequency noise and then apply the proposed localization algorithm to this converted noise. Similar experiments for passive static experiments were already done by L. Chehami et al. [89]. Applying such conversion devices is of interest, because this is the way to improve spatial stationarity of the noise sources (here probe signal), and also because the noise common in nature, vehicles and structures in service mostly exists in low-frequency range.

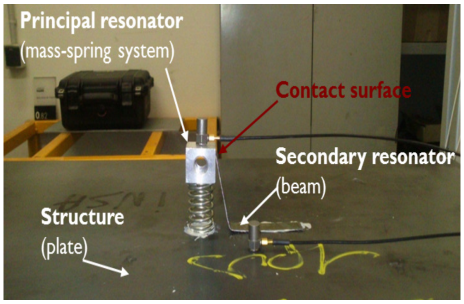

FIGURE 5.19 – Artificial secondary source : mass-spring resonator with a frictional beam.

Another perspective of this work is to modify the proposed localization algorithm for passive pump, i.e. instead of low frequency continuous harmonic modulation, expose the plate to the low frequency noise. In this thesis, we studied cases of active pump/active probe and active pump/passive probe. Using passive pump would be a real challenge, and constitutes another step towards completely passive structural health monitoring.

In this work, passive baseline-free localization algorithm is applied for model artificial contact acoustic nonlinearity. The next step is to try it on more realistic contact defects such as cracks, delaminations, notches, etc. Also it would be possible to quantify and optimize experimental parameters more, if the parameters of experiment were similar to parameters in our wave-CAN interaction modeling tool, since we would be able to predict the interaction regime.

The ultimate long term goal of this study is to apply the developed passive localization in the field tests to find locations of real flaws in plate-like structures in service such as a wing of an aircraft.

References

[1] J. F. Claerbout. Synthesis of a Layered Medium from its Acoustic Transmission Response. *Geophysics*, 33(2) :264–269, April 1968.

[2] O. I. Lobkis and R. L. Weaver. On the emergence of the Green's function in the correlations of a diffuse field. *The Journal of the Acoustical Society of America*, 110(6) :3011–3017, December 2001.

[3] S. Mukherjee, M. A. Morjaria, and F. C. Moon. Eddy Current Flows Around Cracks in Thin Plates for Nondestructive Testing. *Journal of Applied Mechanics*, 49(2) :389–395, June 1982.

[4] J. M. Grochowalski and T. Chady. Pulsed Multifrequency Excitation and Spectrogram Eddy Current Testing (PMFES-ECT) for Nondestructive Evaluation of Conducting Materials. *Materials*, 14(18) :5311, September 2021.

[5] P. M. V. Subbarao, P. Munshi, and K. Muralidhar. Performance Evaluation of Iterative Tomographic Algorithms applied to Reconstruction of a Three-Dimensional Temperature Field. *Numerical Heat Transfer, Part B : Fundamentals*, 31(3) :347–372, April 1997.

[6] A. Rosencwaig. Thermal-Wave Imaging. *Science*, 218(4569) :223–228, October 1982.

[7] T. Bowen, R. L. Nasoni, and A. E. Pifer. Thermoacoustic Imaging Induced by Deeply Penetrating Radiation. In M. Kaveh, R. K. Mueller, and J. F. Greenleaf, editors, *Acoustical Imaging*, volume 13, pages 409–427. Springer US, Boston, MA, 1984. Series Title : Acoustical Imaging.

[8] X. Guo. Ultrasonic Infrared Thermography of Aluminium Thin Plates for Crack Inspection in Friction Stir Welded Joints. *IEEE Sensors Journal*, 20(12) :6524–6531, June 2020.

[9] R. Clark, W. D. Dover, and L. J. Bond. The effect of crack closure on the reliability of NDT predictions of crack size. *NDT International*, 20(5) :269–275, October 1987.

[10] S. N Dwivedi and A. Sharan. Development of knowledge-based engineering module for diagnosis of defects in casting and interpretation of defects by nondestructive testing. *Journal of Materials Processing Technology*, 141(2) :155–162, October 2003.

[11] M. Mitra and S. Gopalakrishnan. Guided wave based structural health monitoring : A review. *Smart Materials and Structures*, 25(5) :053001, May 2016.

[12] L. Yu, L. Cheng, and Z. Su. Correlative Sensor Array for Damage Identification. *Structural Control and Health Monitoring*, 19(8) :650–671, December 2012.

[13] P. Wilcox, M. Lowe, and P. Cawley. The effect of dispersion on long-range inspection using ultrasonic guided waves. *NDT & E International*, 34(1) :1–9, January 2001.

[14] P. D. Wilcox. A rapid signal processing technique to remove the effect of dispersion from guided wave signals. *IEEE Transactions on Ultrasonics, Ferroelectrics and Frequency Control*, 50(4) :419–427, April 2003.

[15] X. Liu, C. Zhou, and Z. Jiang. Damage localization in plate-like structure using built-in PZT sensor network. *Smart Structures and Systems*, 9(1) :21–33, January 2012.

[16] T. Ghosh, T. Kundu, and P. Karpur. Efficient use of Lamb modes for detecting defects in large plates. *Ultrasonics*, 36(7) :791–801, May 1998.

[17] E. Le Clézio, M. Castaings, and B. Hosten. The interaction of the S0 Lamb mode with vertical cracks in an aluminium plate. *Ultrasonics*, 40(1-8) :187–192, May 2002.

[18] F. L. Degertekin and B. T. Khuri-Yakub. Single mode Lamb wave excitation in thin plates by Hertzian contacts. *Applied Physics Letters*, 69(2) :146–148, July 1996.

[19] I. A. Viktorov. *Rayleigh and Lamb waves : physical theory and applications.* Springer Science + Business Media, New York, 2013.

[20] A. E. H. Love. XVI. The small free vibrations and deformation of a thin elastic shell. *Philosophical Transactions of the Royal Society of London. (A.)*, 179 :491–546, December 1888.

[21] R. Gorgin, Y. Luo, and Z. Wu. Environmental and operational conditions effects on Lamb wave based structural health monitoring systems : A review. *Ultrasonics*, 105 :106114, July 2020.

[22] X. Lu, C. K. Soh, and P. V. Avvari. Lamb wave propagation in vibrating structures for effective health monitoring. In T. Kundu, editor, *Proc. SPIE Health Monitoring of Structural and Biological Systems 2015*, volume 9438, page 94381Z, San Diego, California, United States, March 2015.

[23] Y.âH. Pao and U. Gamer. Acoustoelastic waves in orthotropic media. *The Journal of the Acoustical Society of America*, 77(3) :806–812, March 1985.

[24] Y. Lu and J. E. Michaels. A methodology for structural health monitoring with diffuse ultrasonic waves in the presence of temperature variations. *Ultrasonics*, 43(9) :717–731, October 2005.

[25] G. Konstantinidis, B. W. Drinkwater, and P. D. Wilcox. The temperature stability of guided wave structural health monitoring systems. *Smart Materials and Structures*, 15(4) :967–976, August 2006.

[26] A. J. Croxford, J. Moll, P. D. Wilcox, and J. E. Michaels. Efficient temperature compensation strategies for guided wave structural health monitoring. *Ultrasonics*, 50(4-5) :517–528, April 2010.

[27] N. Stubbs and J.-T. Kim. Damage localization in structures without baseline modal parameters. *AIAA Journal*, 34(8) :1644–1649, August 1996.

[28] S. R. Anton, D. J. Inman, and G. Park. Reference-Free Damage Detection Using Instantaneous Baseline Measurements. *AIAA Journal*, 47(8) :1952–1964, August 2009.

[29] X. Wu, J. Ghaboussi, and J. H. Garrett. Use of neural networks in detection of structural damage. *Computers & Structures*, 42(4) :649–659, February 1992.

[30] K. S. Alguri, J. E. Michaels, and J. B. Harley. Robust baseline subtraction for ultrasonic full wavefield analysis. In *AIP Conference Proceedings*, volume 1806, page 020005, Atlanta, Georgia, USA, 2017.

[31] J. J. Lee, J. W. Lee, J. H. Yi, C. B. Yun, and H. Y. Jung. Neural networks-based damage detection for bridges considering errors in baseline finite element models. *Journal of Sound and Vibration*, 280(3-5) :555–578, February 2005.

[32] S. Mariani, Q. Rendu, M. Urbani, and C. Sbarufatti. Causal dilated convolutional neural networks for automatic inspection of ultrasonic signals in non-destructive evaluation and structural health monitoring. *Mechanical Systems and Signal Processing*, 157 :107748, August 2021.

[33] T. Planès and E. Larose. A review of ultrasonic Coda Wave Interferometry in concrete. *Cement and Concrete Research*, 53 :248–255, November 2013.

[34] E. Niederleithinger, X. Wang, M. Herbrand, and M. Müller. Processing Ultrasonic Data by Coda Wave Interferometry to Monitor Load Tests of Concrete Beams. *Sensors*, 18(6) :1971, June 2018.

[35] Y. Zhang, O. Abraham, V. Tournat, A. Le Duff, B. Lascoup, A. Loukili, F. Grondin, and O. Durand. Validation of a thermal bias control technique for Coda Wave Interferometry (CWI). *Ultrasonics*, 53(3) :658–664, March 2013.

[36] Y. Zhang, V. Tournat, O. Abraham, O. Durand, S. Letourneur, A. Le Duff, and B. Lascoup. Nonlinear mixing of ultrasonic coda waves with lower frequency-swept pump waves for a global detection of defects in multiple scattering media. *Journal of Applied Physics*, 113(6) :064905, February 2013.

[37] T. R. Hay, R. L. Royer, H. Gao, X. Zhao, and J. L. Rose. A comparison of

embedded sensor Lamb wave ultrasonic tomography approaches for material loss detection. *Smart Materials and Structures*, 15(4) :946–951, August 2006.

[38] D. Wang, L. Ye, Y. Lu, and Z. Su. Probability of the presence of damage estimated from an active sensor network in a composite panel of multiple stiffeners. *Composites Science and Technology*, 69(13) :2054–2063, October 2009.

[39] J. Zhang, K. Liu, C. Gao, Z. Wu, Y. Zheng, and D. Gao. Multi-Mode Guided Waves Based Reference-Free Damage Diagnostic Imaging in Plates. *Structural Durability & Health Monitoring*, 13(1) :41–59, 2019.

[40] X. Zhao, H. Gao, G. Zhang, B. Ayhan, F. Yan, C. Kwan, and J. L. Rose. Active health monitoring of an aircraft wing with embedded piezoelectric sensor/actuator network : I. Defect detection, localization and growth monitoring. *Smart Materials and Structures*, 16(4) :1208–1217, August 2007.

[41] G. Azuara, E. Barrera, M. Ruiz, and D. Bekas. Damage Detection and Characterization in Composites Using a Geometric Modification of the RAPID Algorithm. *IEEE Sensors Journal*, 20(4) :2084–2093, February 2020.

[42] C. Pacheco and R. Snieder. Time-lapse travel time change of multiply scattered acoustic waves. *The Journal of the Acoustical Society of America*, 118(3) :1300–1310, September 2005.

[43] V. Rossetto, L. Margerin, T. Planès, and É. Larose. Locating a weak change using diffuse waves : Theoretical approach and inversion procedure. *Journal of Applied Physics*, 109(3) :034903, February 2011.

[44] M. Fink, D. Cassereau, A. Derode, C. Prada, P. Roux, M. Tanter, J.-L. Thomas, and F. Wu. Time-reversed acoustics. *Reports on Progress in Physics*, 63(12) :1933–1995, December 2000.

[45] H. W. Park, H. Sohn, K. H. Law, and C. R. Farrar. Time reversal active sensing for health monitoring of a composite plate. *Journal of Sound and Vibration*, 302(1-2) :50–66, April 2007.

[46] H. Sohn and H. W. Park. Can damage be detected without any baseline

data ? In *Proc. SPIE Health Monitoring and Smart Nondestructive Evaluation of Structural and Biological Systems IV*, volume 5768, pages 418–429, San Diego, CA, May 2005.

[47] R. K. Ing and M. Fink. Self-focusing and time recompression of Lamb waves using a time reversal mirror. *Ultrasonics*, 36(1-5) :179–186, February 1998.

[48] R. K. Ing and M. Fink. Time-reversed Lamb waves. *IEEE Transactions on Ultrasonics, Ferroelectrics and Frequency Control*, 45(4) :1032–1043, July 1998.

[49] C. H. Wang, J. T. Rose, and F.-K. Chang. A synthetic time-reversal imaging method for structural health monitoring. *Smart Materials and Structures*, 13(2) :415–423, April 2004.

[50] P. Blanloeuil, L. R. F. Rose, J. A. Guinto, M. Veidt, and C. H. Wang. Closed crack imaging using time reversal method based on fundamental and second harmonic scattering. *Wave Motion*, 66 :156–176, November 2016.

[51] P. Blanloeuil, L. R. F. Rose, M. Veidt, and C. H. Wang. Time reversal invariance for a nonlinear scatterer exhibiting contact acoustic nonlinearity. *Journal of Sound and Vibration*, 417 :413–431, March 2018.

[52] H. W. Park, S. B. Kim, and H. Sohn. Understanding a time reversal process in Lamb wave propagation. *Wave Motion*, 46(7) :451–467, November 2009.

[53] N. Smagin, A. Trifonov, O. Bou Matar, and V.V. Aleshin. Local damage detection by nonlinear coda wave interferometry combined with time reversal. *Ultrasonics*, 108 :106226, December 2020.

[54] L. Huang, L. Zeng, and J. Lin. Baseline-free damage detection in composite plates based on the reciprocity principle. *Smart Materials and Structures*, 27(1) :015026, January 2018.

[55] H. Sohn, H. W. Park, K. H. Law, and C. R. Farrar. Combination of a Time Reversal Process and a Consecutiv Outlier Analysis for Baseline-free Damage Diagnosis. *Journal of Intelligent Material Systems and Structures*, 18(4) :335–346, April 2007.

[56] B. Park, H. Sohn, C.-M. Yeum, and T. C. Truong. Laser ultrasonic imaging and damage detection for a rotating structure. *Structural Health Monitoring : An International Journal*, 12(5-6) :494–506, September 2013.

[57] S. B. Kim and H. Sohn. Instantaneous reference-free crack detection based on polarization characteristics of piezoelectric materials. *Smart Materials and Structures*, 16(6) :2375–2387, December 2007.

[58] W. Qu, L. Xiao, Y. Zhou, and D. J. Inman. Lamb wave damage detection using time reversal DORT method. *Smart Materials and Structures*, 22(4) :045014, April 2013.

[59] M. Kannusamy, S. Kapuria, and S. Sasmal. Accurate baseline-free damage localization in plates using refined Lamb wave time-reversal method. *Smart Materials and Structures*, 29(5) :055044, May 2020.

[60] D. A. Hutchins, D. P. Jansen, and C. Edwards. Lamb-wave tomography using non-contact transduction. *Ultrasonics*, 31(2) :97–103, January 1993.

[61] S. M. Rytov. *Principles of statistical radiophysics 3 : elements of random fields.* Springer, Berlin and Heidelberg, 2012.

[62] C. R. Farrar and G.H. James III. System Identification from Ambient Vibration Measurements on a Bridge. *Journal of Sound and Vibration*, 205(1) :1–18, August 1997.

[63] E. Larose, P. Roux, and M. Campillo. Reconstruction of RayleighâLamb dispersion spectrum based on noise obtained from an air-jet forcing. *The Journal of the Acoustical Society of America*, 122(6) :3437–3444, December 2007.

[64] K. G. Sabra, A. Duroux, A. Srivastava, F. Lanza di Scalea, and I. Bartoli. Passive-only wave-based structural health monitoring from ambient noise. In *Proceedings of SPIE - The International Society for Optical Engineering*, volume 6935, page 693508, San Diego, California, March 2008.

[65] R. Snieder. Extracting the Greenâs function from the correlation of coda waves : A derivation based on stationary phase. *Physical Review E*,

69(4) :046610, April 2004.

[66] S.G. Mallat and Z. Zhang. Matching pursuits with time-frequency dictionaries. *IEEE Transactions on Signal Processing*, 41(12) :3397–3415, December 1993.

[67] E. Lubeigt, S. Rakotonarivo, S. Mensah, J.-F. Chaix, F. Baqué, and W. A. Kuperman. Passive structural monitoring based on data-driven matched field processing. *The Journal of the Acoustical Society of America*, 145(4) :EL317–EL322, April 2019.

[68] L. Chehami, E. Moulin, J. de Rosny, C. Prada, O. Bou Matar, F. Benmeddour, and J. Assaad. Detection and localization of a defect in a reverberant plate using acoustic field correlation. *Journal of Applied Physics*, 115(10) :104901, March 2014.

[69] J. E. Michaels and T. E. Michaels. Guided wave signal processing and image fusion for in situ damage localization in plates. *Wave Motion*, 44(6) :482–492, June 2007.

[70] L. Chehami, E. Moulin, J. de Rosny, C. Prada, J. Assaad, and F. Benmeddour. Experimental Study of Passive Defect Detection and Localization in Thin Plates from Noise Correlation. *Physics Procedia*, 70 :322–325, 2015.

[71] B. W. Drinkwater and P. D. Wilcox. Ultrasonic arrays for non-destructive evaluation : A review. *NDT & E International*, 39(7) :525–541, October 2006.

[72] K.E. Thomenius. Evolution of ultrasound beamformers. In *1996 IEEE Ultrasonics Symposium. Proceedings*, volume 2, pages 1615–1622, San Antonio, TX, USA, 1996. IEEE.

[73] C. Holmes, B. W. Drinkwater, and P. D. Wilcox. Post-processing of the full matrix of ultrasonic transmit-receive array data for non-destructive evaluation. *NDT & E International*, 38(8) :701–711, December 2005.

[74] W. A. K. Deutsch, A. Cheng, and J. D. Achenbach. Self-Focusing of Rayleigh Waves and Lamb Waves with a Linear Phased Array. *Research in Nondestructive Evaluation*, 9(2) :81–95, January 1997.

[75] P. Wilcox. Lamb and SH wave transducer arrays for the inspection of large areas of thick plates. In *AIP Conference Proceedings*, volume 509, pages 1049–1056, Montreal (Canada), 2000. AIP.

[76] T. Fromenteze, C. Decroze, and D. Carsenat. UWB passive beamforming for large antenna arrays. In *2014 IEEE International Conference on Ultra-WideBand (ICUWB)*, pages 47–50, Paris, France, September 2014. IEEE.

[77] J. C. P. McKeon and M. K. Hinders. Parallel projection and crosshole Lamb wave contact scanning tomography. *The Journal of the Acoustical Society of America*, 106(5) :2568–2577, November 1999.

[78] J. E. Michaels, J. S. Hall, and T. E. Michaels. Adaptive imaging of damage from changes in guided wave signals recorded from spatially distributed arrays. In T. Kundu, editor, *Proc. SPIE 7295, Health Monitoring of Structural and Biological Systems 2009*, page 729515, San Diego, California, USA, March 2009.

[79] P.D. Wilcox. Omni-directional guided wave transducer arrays for the rapid inspection of large areas of plate structures. *IEEE Transactions on Ultrasonics, Ferroelectrics and Frequency Control*, 50(6) :699–709, June 2003.

[80] F. Yan, R. L. Royer, and J. L. Rose. Ultrasonic Guided Wave Imaging Techniques in Structural Health Monitoring. *Journal of Intelligent Material Systems and Structures*, 21(3) :377–384, February 2010.

[81] R. Griesmaier, N. Hyvönen, and O. Seiskari. A note on analyticity properties of far field patterns. *Inverse Problems & Imaging*, 7(2) :491–498, 2013.

[82] P. A. Martin. Multiple scattering and scattering cross sections. *The Journal of the Acoustical Society of America*, 143(2) :995–1002, February 2018.

[83] A.N. Norris and C. Vemula. Scattering of flexural waves on thin plates. *Journal of Sound and Vibration*, 181(1) :115–125, March 1995.

[84] M. Born and E. Wolf. *Principles of optics*. Cambridge University Press, Cambridge, United Kingdom, seventh anniversary edition, 60th anniversary of first edition, 20th anniversary of seventh edition edition, 2019.

[85] A. Ishimaru. *Wave propagation and scattering in random media.* Academic Press, New York, 1978.

[86] C. Vemula and A.N. Norris. Flexural wave propagation and scattering on thin plates using Mindlin theory. *Wave Motion*, 26(1) :1–12, August 1997.

[87] H. Achdjian, E. Moulin, F. Benmeddour, J. Assaad, L. Dupont, and L. Chehami. Reverberation of flexural waves scattered by a local heterogeneity in a plate. *The Journal of the Acoustical Society of America*, 140(1) :157–164, July 2016.

[88] E. Moulin, H. Achdjian, F. Benmeddour, L. Dupont, L. Chehami, and J. Assaad. Caractérisation d'un défaut dans une plaque á partir de la réverbération des ondes de flexion. In *13e Congrès Français d'Acoustique*, pages 1701–1708, Le Mans, France, 2016.

[89] L. Chehami, E. Moulin, J. de Rosny, C. Prada, E. Chatelet, G. Lacerra, K. Gryllias, and F. Massi. Nonlinear secondary noise sources for passive defect detection using ultrasound sensors. *Journal of Sound and Vibration*, 386 :283–294, January 2017.

[90] D. V. Sivuhin. *General course of physics. volume 1. mechanics.* Book on Demand Ltd., Moscow, 2014.

[91] L. D. Landau, L. P. Pitaevskii, A. M. Kosevich, and E. M. Lifshitz. *Theory of Elasticity : Volume 7.* Butterworth-Heinemann, 3rd edition, 1986.

[92] K. L. Johnson. *Contact mechanics.* Cambridge University Press, Cambridge, UK, 2003.

[93] J. Rivière, G. Renaud, R. A. Guyer, and P. A. Johnson. Pump and probe waves in dynamic acousto-elasticity : Comprehensive description and comparison with nonlinear elastic theories. *Journal of Applied Physics*, 114(5) :054905, August 2013.

[94] M. Lott, C. Payan, V. Garnier, P. Y. Le Bas, T. J. Ulrich, and M. C. Remillieux. Three-dimensional modeling and numerical predictions of multimodal

nonlinear behavior in damaged concrete blocks. *The Journal of the Acoustical Society of America*, 144(3) :1154–1159, September 2018.

[95] J. N. Eiras, C. Payan, S. Rakotonarivo, and V. Garnier. Damage detection and localization from linear and nonlinear global vibration features in concrete slabs subjected to localized thermal damage. *Structural Health Monitoring*, 20(2) :567–579, March 2021.

[96] E. P. Tomasini and P. Castellini, editors. *Laser doppler vibrometry : a multimedia guide to its features and usage.* Springer, Berlin [Heidelberg], 2020.

[97] A. W. Leissa. *Vibration of plates.* American Institute of Physics, Woodbury, NY, reprint. ed edition, 1993.

[98] M. Terzi, L. Chehami, M. Farin, E. Moulin, V. Aleshin, N. Smagin, J. de Rosny, and F. Benmeddour. Pump-probe localization technique of varying solid contacts. *The Journal of the Acoustical Society of America*, 149(5) :2943–2949, May 2021.

[99] M. Bruneau. *Manuel d'acoustique fondamentale.* Études en méchanique des matériaux et des structures. Hermés, Paris, 1998.

[100] M. Farin, C. Palerm, C. Prada, and J. de Rosny. Localization of unbounded contacts on vibrating elastic plates. *The Journal of the Acoustical Society of America*, 148(6) :3455–3466, December 2020.

[101] Dirk P. Kroese, Tim Brereton, Thomas Taimre, and Zdravko I. Botev. Why the Monte Carlo method is so important today. *WIREs Computational Statistics*, 6(6) :386–392, November 2014.

[102] G. D. Bensen, M. H. Ritzwoller, M. P. Barmin, A. L. Levshin, F. Lin, M. P. Moschetti, N. M. Shapiro, and Y. Yang. Processing seismic ambient noise data to obtain reliable broad-band surface wave dispersion measurements. *Geophysical Journal International*, 169(3) :1239–1260, June 2007.

[103] L. Chehami, E. Moulin, J. de Rosny, and C. Prada. Accuracy of Green's function estimation from correlation of diffuse elastic waves on thin plates.

The Journal of the Acoustical Society of America, 146(5) :3505–3511, November 2019.

[104] V. Cotoni, R.S. Langley, and M.R.F. Kidner. Numerical and experimental validation of variance prediction in the statistical energy analysis of built-up systems. *Journal of Sound and Vibration*, 288(3) :701–728, December 2005.

[105] L. A. Galin. *Contact Problems*, volume 155 of *Solid Mechanics and Its Applications*. Springer Netherlands, Dordrecht, 2008.

[106] V. L. Popov and M. Heß. *Method of Dimensionality Reduction in Contact Mechanics and Friction*. Springer, Berlin [Heidelberg], 2015.

[107] F. P. Bowden and D. Tabor. The area of contact between stationary and moving surfaces. *Proceedings of the Royal Society of London. Series A. Mathematical and Physical Sciences*, 169(938) :391–413, February 1939.

[108] G. Carbone and F. Bottiglione. Asperity contact theories : Do they predict linearity between contact area and load ? *Journal of the Mechanics and Physics of Solids*, 56(8) :2555–2572, August 2008.

[109] S. Hyun and M. O. Robbins. Elastic contact between rough surfaces : Effect of roughness at large and small wavelengths. *Tribology International*, 40(10-12) :1413–1422, October 2007.

[110] B. N. J. Persson, F. Bucher, and B. Chiaia. Elastic contact between randomly rough surfaces : Comparison of theory with numerical results. *Physical Review B*, 65(18) :184106, April 2002.

[111] M. Paggi and M. Ciavarella. The coefficient of proportionality κ between real contact area and load, with new asperity models. *Wear*, 268(7-8) :1020–1029, March 2010.

[112] M. Paggi, R. Pohrt, and V. L. Popov. Partial-slip frictional response of rough surfaces. *Scientific Reports*, 4(1) :5178, May 2015.

[113] S. Biwa, S. Nakajima, and N. Ohno. On the Acoustic Nonlinearity of Solid-

Solid Contact With Pressure-Dependent Interface Stiffness. *Journal of Applied Mechanics*, 71(4) :508–515, July 2004.

[114] M. Yuan, J. Zhang, S.-J. Song, and H.-J. Kim. Numerical simulation of Rayleigh wave interaction with surface closed cracks under external pressure. *Wave Motion*, 57 :143–153, September 2015.

[115] R. Pohrt and V. L. Popov. Normal Contact Stiffness of Elastic Solids with Fractal Rough Surfaces. *Physical Review Letters*, 108(10) :104301, March 2012.

[116] R. Pohrt and V. L. Popov. Contact stiffness of randomly rough surfaces. *Scientific Reports*, 3(1) :3293, December 2013.

[117] V. Aleshin, O. Bou Matar, and K. Van Den Abeele. Method of memory diagrams for mechanical frictional contacts subject to arbitrary 2D loading. *International Journal of Solids and Structures*, 60-61 :84–95, May 2015.

[118] R. D. Mindlin and H. Deresiewicz. Elastic Spheres in Contact Under Varying Oblique Forces. *Journal of Applied Mechanics*, 20(3) :327–344, September 1953.

[119] M. Ciavarella. The generalized Cattaneo partial slip plane contact problem. I–Theory. *International Journal of Solids and Structures*, 35(18) :2349–2362, June 1998.

[120] M. Ciavarella. Tangential Loading of General Three-Dimensional Contacts. *Journal of Applied Mechanics*, 65(4) :998–1003, December 1998.

[121] J. Jäger. Axi-symmetric bodies of equal material in contact under torsion or shift. *Archive of Applied Mechanics*, 65(7) :478–487, September 1995.

[122] J. Jäger. A New Principle in Contact Mechanics. *Journal of Tribology*, 120(4) :677–684, October 1998.

[123] R. L. Munisamy, D. A. Hills, and D. Nowell. Static Axisymmetric Hertzian Contacts Subject to Shearing Forces. *Journal of Applied Mechanics*, 61(2) :278–283, June 1994.

[124] R. L. Munisamy, D. A. Hills, and D. Nowell. Contact of similar and dissimilar

elastic spheres under tangential loading. In *Contact mechanics : proceedings of the international symposium*, Lausanne, 1992. Presses polytechniques et universitaires romandes.

[125] V. V. Aleshin, S. Delrue, K. Van Den Abeele, and O. Bou Matar. Nonlinear and hysteretic constitutive models for wave propagation in solid media with cracks and contacts. In T. Kundu, editor, *Nonlinear Ultrasonic and Vibro-Acoustical Techniques for Nondestructive Evaluation (Chapter 5)*, pages 175–224. Springer, Cham, 2019.

[126] V. Aleshin, S. Delrue, A. Trifonov, O. Bou Matar, and K. Van Den Abeele. Two dimensional modeling of elastic wave propagation in solids containing cracks with rough surfaces and friction - Part I : Theoretical background. *Ultrasonics*, 82 :11–18, January 2018.

[127] J. A. Greenwood and J. B. P. Williamson. Contact of nominally flat surfaces. *Proceedings of the Royal Society of London. Series A. Mathematical and Physical Sciences*, 295(1442) :300–319, December 1966.

[128] V. V. Aleshin and O. Bou Matar. Solution to the frictional contact problem via the method of memory diagrams for general 3D loading histories. *Physical Mesomechanics*, 19(2) :130–135, April 2016.

[129] E. Hairer, S. P. Nørsett, and G. Wanner. *Solving ordinary differential equations I : nonstiff problems*. Number 8 in Springer series in computational mathematics. Springer, Heidelberg ; London, 2nd rev. edition, 2009.

[130] J. Virieux. *P-SV* wave propagation in heterogeneous media : Velocity-stress finite-difference method. *Geophysics*, 51(4) :889–901, April 1986.

[131] R. Courant, K. Friedrichs, and H. Lewy. Über die partiellenber die partiellen Differenzengleichungen der mathematischen Physik. *Mathematische Annalen*, 100(1) :32–74, December 1928.

[132] B. Finkelstein and R. Kastner. Finite difference time domain dispersion reduction schemes. *Journal of Computational Physics*, 221(1) :422–438, January 2007.

[133] G. Lacerra, E. Chatelet, F. Massi, and K. Gryllias. Design of a Mechanical System for Energy Transfer between Acoustic Fields by Frictional Contact Nonlinearity. In *DINAME 2015 : XVII International Symposium on Dynamic Problems of Mechanics*, Natal, Brazil, February 2015. ABCM.

Abstract

In structural health monitoring, acoustic methods without use of a reference intact sample are nowadays of great interest due to variability of environmental and operational conditions. This thesis presents an acoustic reference-free method for detecting and localizing defects in thin plates. The proposed approach is based on pump-probe measurements and a differential signal processing algorithm. The pump-probe scheme here means the simultaneous excitation of low-frequency vibrations and high-frequency acoustic pulses generated by a piezoelectric transducer and recorded by an array of transducers of the same kind. The role of pumping vibrations is in imposing changes to loading conditions for a defect (here a model Hertzian contact i.e. a small ball pressed against the tested plate) while the ultrasonic Lamb wave pulses probe the defect in various loading states. Then a differential signal processing algorithm based on backpropagation of A0 Lamb mode is used to detect and locate the defect. Two detection modes have been studied: the mode requiring the synchronization between the pump and probe signals, and the non-synchronous mode. In the latter case, a correction with the use of ad hoc weight coefficients improves the detection. Further, a parametric study was performed by computing the image contrast as a function of the defect scattering cross-section that allowed us to determine a minimum detection threshold. The application of the method to passive imaging (i.e. using white noise instead of probe pulses) produced encouraging results for the price of increasing the number of receivers. Finally, numerical modeling for the interaction of an ultrasonic wave with a Hertz-Mindlin frictional contact was performed in 2D to compare the model defect (ball pressed against the plate) with a more realistic one (crack).

Key words: structural health monitoring, Lamb waves, Green’s function, noise correlation, passive imaging, baseline-free localization, beamforming, pump-probe experiment, Hertz-Mindlin contact, method of memory diagrams.

Résumé

Le contrôle-qualité de matériaux par méthodes acoustiques sans référence suscite aujourd’hui un grand intérêt en contrôle santé intégré (CSI) au vu de la variabilité des conditions environnementales et opérationnelles. Dans ce manuscrit, nous proposons une méthode de détection synchrone/non synchrone de défaut soumis à des sollicitations basses fréquences, permettant une localisation sans état hypothétique "sans défaut". Une série de tests "pompe-sonde" a été menée sur une plaque d'aluminium. Un pot vibrant est fixé sur cette dernière afin de la mettre en vibration à une fréquence de quelques Hz. Une bille solidaire d'une lame en acier est pressée contre la plaque (contact Hertzien) et joue le rôle d'un défaut (reproduisant ainsi un contact tel qu'on peut le rencontrer par exemple entre deux fronts d'une fissure). Un réseau de transducteurs piézoélectriques est utilisé pour faire l'imagerie ultrasonore. Le principe de la détection repose sur la modulation du contact entre la plaque et la bille par la vibration pompe basse fréquence. Des mesures ultrasonores répétées (onde sonde) permettent ainsi d'interroger le défaut dans plusieurs états de sollicitation. Un algorithme d'imagerie différentielle permet alors de mettre en évidence et localiser le défaut. Deux modes de détection ont été testés : 1) mode synchrone entre la pompe et les signaux ultrasonores et 2) mode non synchrone. Dans ce dernier cas, une correction par des coefficients de pondération ad-hoc permet d’améliorer la détection. Une étude paramétrique a été également réalisée en reliant le contraste des images en fonction de la section de diffusion de défaut. Ceci a permis de définir un seuil minimal de détection d’un défaut de type contact variable. L'application de cette méthode à l'imagerie passive par corrélation de bruit a donné des résultats encourageants, à condition d'augmenter la densité du réseau de capteurs ultrasonores. Enfin, des simulations numériques en 2D, modélisant l'interaction d'une onde ultrasonore avec un contact de frottement type "Hertz-Mindlin" ont été réalisées afin de comparer le défaut actuel (bille pressée sur la plaque) avec un défaut réaliste (une fissure).

Mots clés : contrôle santé intégré, ondes de Lamb, fonction de Green, corrélation du bruit, imagerie passive, localisation sans référence, beamforming, expérience pompe-sonde, contact de Hertz-Mindlin, méthode des diagrammes de mémoire.